VERIFICATION AND VALIDATION STUDY OF CFD SIMULATIONS OF SEMI-SUBMERSIBLE PLATFORM FOR FLOATING OFFSHORE WIND TURBINES

A Dissertation

by

YU WANG

Submitted to the Graduate and Professional School of
Texas A&M University
in partial fulfillment of the requirements for the degree of

DOCTOR OF PHILOSOPHY

Chair of Committee,	Hamn-Ching Chen
Committee Members,	Moo-Hyun Kim
	Richard S. Mercier
	John Michael Niedzwecki
Head of Department,	Sharath Girimaji

May 2022

Major Subject: Ocean Engineering

ABSTRACT

In the proposed study, Computational Fluid Dynamic (CFD) code ReFRESCO is utilized to analyze the hydrodynamic behaviour of a Floating Offshore Wind Turbine with a semi-submersible platform. An in-house nonlinear Finite Element Method (FEM) mooring analysis module MOORING3D is coupled with ReFRESCO to count in the hydrodynamic effect brought by the mooring system. Four load conditions are simulated using the coupled CFD-FEM code. They are respectively pitch free decay, regular waves, bichromatic waves and irregular waves. In the simulations of pitch free decay condition, Reynolds Average Navier Stokes (RANS) equations are used as governing equations closed by KSKL turbulence model. While k-ω SST-IDDES turbulence model is used in irregular wave simulation. In the remaining simulations, laminar flow assumption is adopted. Volume of Fluid (VOF) method is utilized to model the free surfaces. A six degree-of-freedoms (DOFs) motion solver is used to interact with both flow solver and mooring solver.

A systematic verification and validation study is applied to selected metrics obtained in the first three load conditions. Numerical uncertainties embedded in the signal processing, iterative method, grid and time step combinations are quantified. The respective uncertainties are namely statistical uncertainty, iterative uncertainty and discretization uncertainty. The statistical uncertainty is quantified for periodic simulations with waves using Transient Scanning Technique (TST). The iterative uncertainty is quantified using least square method towards iterative errors obtained from repeated simulations with different convergence tolerance. The discretization uncertainty is quantified by applying the similar method towards solutions obtained by repeated simulations with different combination of grid sizes and time step sizes. Validation uncertainties are computed by summing the numerical, input and experimental uncertainties. The simulation results are validated against the experimental measurements with the uncertainty range. A standard procedure of verification and validation study is generalized from this study for applications of hydrodynamic analysis of FOWT using CFD simulations.

DEDICATION

To my parents.

For their continuous love and support.

To my wife Yi Wei.

For her support, patience and faith.

ACKNOWLEDGMENTS

I would like to thank the committee chair, Dr. Hamn-Ching Chen, for his thorough instruction and support during my PhD study. I am deeply grateful for the opportunity provided by him to participate in the collaboration with MARIN which forms my dissertation study.

I would like to extend my gratitude to my committee members, Dr. Richard Mercier, Dr. Moo-Hyun Kim, and Dr. John Niedzwecki, for their valuable time, suggestions, and personal encouragement.

Thank Dr. Guilherme Vaz in BlueOASIS, Dr. Arjen Koop in MARIN and Dr. Simon Mewes in University of Duisburg-Essen for their support and collaboration.

The IT support and computing time granted by the High Performance Research Computing (HPRC) Center of Texas A&M University is gratefully acknowledged.

Thanks to the friends, department faculty and staff for making a great experience in Texas A&M University.

CONTRIBUTORS AND FUNDING SOURCES

Contributors

This work was supported by a dissertation committee consisting of Professor Hamn-Ching Chen, John Niedzwecki and Moo-Hyun Kim of the Department of Ocean Engineering and Professor Richard Mercier of the Department of Civil and Environmental Engineering. The computational resource is granted by Texas A&M University High Performance Research Computing center. All work for the dissertation was completed by the student, under the advisement of Professor Hamn-Ching Chen of the Department of Ocean Engineering.

Funding Sources

There are no outside funding contributions to acknowledge related to the research and compilation of this document.

TABLE OF CONTENTS

Page

ABSTRACT ii

DEDICATION iii

ACKNOWLEDGMENTS iv

CONTRIBUTORS AND FUNDING SOURCES v

TABLE OF CONTENTS vi

LIST OF FIGURES ix

LIST OF TABLES xiii

1. INTRODUCTION 1

    1.1 Background and significance 1
    1.2 Literature Review 1
    1.3 Dissertation Objective 3
    1.4 Dissertation Organization 4

2. METHODOLOGY 6

    2.1 Flow solver 6
        2.1.1 Navier-Stokes equations 6
        2.1.2 Free surface model 7
        2.1.3 Turbulence model 7
        2.1.4 Wave modelling 9
    2.2 Numerical schemes 13
        2.2.1 Preconditioners 13
        2.2.2 Solver methods 14
        2.2.3 Convective schemes 15
    2.3 Hydrodynamic responses 18
        2.3.1 PQ analysis 18
        2.3.2 Response amplitude operator 20
        2.3.3 Slow drift load QTF 21
        2.3.4 Power spectral density sum 22
    2.4 Verification and Validation 22
        2.4.1 Verification 23
        2.4.2 Validation 27

3. TEST CASE DESCRIPTION 30

3.1 FOWT model 30
3.2 Load conditions 32

4. COUPLING OF MOORING3D AND ReFRESCO 35

4.1 Methodology 35
4.2 Sensitivity study on mooring line coefficients 37
4.3 Discretization uncertainty in MOORING3D 41

5. V&V STUDY OF FOWT SEMI-SUBMERSIBLE PLATFORM UNDER PITCH FREE DECAY 45

5.1 Numerical settings 45
5.2 Verification study 49
5.3 Validation study 54

6. V&V STUDY OF FOWT SEMI-SUBMERSIBLE PLATFORM UNDER REGULAR WAVES 59

6.1 Numerical settings 59
6.2 Verification study 63
6.2.1 Statistical uncertainty 64
6.2.2 Iterative uncertainty 65
6.2.3 Discretization uncertainty 69
6.2.4 Total numerical uncertainty 76
6.3 Validation study 78

7. V&V STUDY OF FOWT SEMI-SUBMERSIBLE PLATFORM UNDER IRREGULAR WAVES 81

7.1 Benchmark case: focused waves 81
7.1.1 Case description and numerical settings 81
7.1.2 Results and discussions 84
7.2 Bichromatic waves 87
7.2.1 Numerical settings 87
7.2.2 Verification study 88
7.3 JONSWAPS spectrum random waves 100
7.3.1 Numerical settings 100
7.3.2 Wave-only simulation 100
7.3.3 Validation study with the semi-submersible platform 101

8. CONCLUSIONS 107

8.1 Generalized procedure of V&V study 107
8.2 Conclusions 108

REFERENCES 111

LIST OF FIGURES

FIGURE Page

2.1 Comparison between simulations with and without a turbulence model. 10

2.2 1D illustration for convective flux discretization schemes. 16

2.3 Time history of free decay motion for a weakly damped system. 18

2.4 Illustration of PQ analysis. 21

2.5 Illustration of Transient Scanning Technique (TST). 28

3.1 DeepCWind semi-submersible floater for the 1/50th scale model tests, reprinted from [1]. 30

3.2 Top view and side view sketch of the 1/50th scaled floater. Mooring arrangement is depicted in top view sketch. 31

3.3 The amplitude spectrum of LC4 - JONSWAP random waves analyzed from experimental data. 33

4.1 The simulation workflow of the coupled code of ReFRESCO and MOORING3D. ... 36

4.2 Cross verification using pitch free decay test data of MOORING3D and OrcaFlex with the baseline coefficient setup, i.e. $C_{Dn} = 2.4$, $C_{Dt} = 0.8$, $C_{Mn} = 3.1$, $C_{Mt} = 1.7$. The experimental measurements is also added for comparison. 39

4.3 Sensitivity test of drag and added mass coefficients for mooring lines using pitch free decay test data. Except for the coefficients labeled in legends, all tests are simulated with the baseline coefficients setup $C_{Dn} = 1.5$, $C_{Dt} = 0.8$, $C_{Mn} = 3.1$, $C_{Mt} = 1.7$. 40

4.4 Sensitivity test of drag and added mass coefficients for mooring lines. Comparison errors of PSDs of the mooring tensions in all three mooring lines against experimental results are depicted with different set of coefficients. Except for the varied coefficient captioned under each plot, the remaining coefficients are set as $C_{Dn} = 1.5$, $C_{Dt} = 0.8$, $C_{Mn} = 3.1$, $C_{Mt} = 1.7$. 41

4.5 The mooring tensions at fairlead of each mooring line in pitch decay test computed by MOORING3D with five different grids. 43

4.6 The mooring tensions at fairlead of each mooring line in pitch decay test computed by MOORING3D with three different time step sizes. 44

5.1 Computational domain setup in all simulations. With refinement sectors defined in Table 5.1. 47

5.2 Grid refinement at semi-submersible platform and free surface. 48

5.3 Pitch free decay motions of the floater using 20 different sets of grid sizes and time step sizes. 50

5.4 3D fit of pitch natural periods gathered from 20 cases. Green bar indicates the uncertainty range of natural period for G3T4. 51

5.5 Discretization uncertainty analysis of pitch motion over 4 oscillation periods. Gray area is the range of motion based on the quantified uncertainty level. 52

5.6 3D fit of pitch peaks with green bar representing uncertainty estimation for G3T4. Uncertainties for first two peaks were evaluated from all 20 cases while others from 8 cases with sufficient simulation time. 53

5.7 Surge, heave and pitch motion histories comparison between CFD simulations with linear mooring model, dynamic mooring model and experiment. Blue and gray bands represent the uncertainty ranges estimated by averaged and maximum value, respectively. 55

5.8 PQ analysis to the pitch motion for numerical solutions with LM (linear mooring model), DM (dynamic mooring model) and experimental results. 56

6.1 Computational domain and the boundary conditions settings in all simulations. 59

6.2 Refinement zones division in the computational domain. See detail refinement settings in Table 6.1. 60

6.3 Grid refinement at semi-submersible platform and free surface for regular wave load conditions. 61

6.4 The amplitude spectrum of 3-DOF motion and wave elevation. 63

6.5 Transient scanning results of surge motion of the semi-submersible platform under the regular waves. 65

6.6 Mean L_2 norm residuals of the z momentum equation at the end of every time step within $[20, 100]$ s versus the numbers of outer iterations. 67

6.7 Residuals in L_2 norm for 4 simulations with different numbers of outer iterations. 68

6.8 Wave heights and motion histories in surge, heave and pitch DOF for 11 simulations conducted for discretization uncertainty analysis. 70

6.9 Phase spectrum of 3-DOF motion compared with the waves. 71

6.10 Surge, heave and pitch RAOs at wave frequency calculated from the 11 simulations for discretization uncertainty analysis. 72

6.11 Surge, heave and pitch RAOs at double wave frequency calculated from the 11 simulations for discretization uncertainty analysis. 73

6.12 Mean surge offset and zero frequency surge QTF calculated from the 11 simulations for discretization uncertainty analysis. 73

6.13 3D fit of all metrics in regular wave case with green bar representing discretization uncertainty bounds for simulation G2T2 (denoted as red dot). 74

6.14 Validation of RAOs, MSO and $SQTF_0$ between numerical results and experimental measurements. The red uncertainty bands represent the total numerical uncertainty and the black ones represent the validation uncertainty. The RAOs at double wave frequency are scaled up by a factor of 10 and the MSO is scaled up by a factor of 500. 79

7.1 Illustration of the wave tank and the locations of the wave probes. 82

7.2 The wave amplitude spectrum of the focused waves. 83

7.3 The computational domain used in the benchmark focused wave simulation. 84

7.4 Wave elevation time series at WP1-4 from the focused wave simulation in comparison with experimental data. 86

7.5 The amplitude spectrum of 3-DOF motion and wave elevation in bichromatic wave condition. 88

7.6 The time history of surge motion of semi-submersible under bichromatic waves with the transient phase marked as orange. Below is the time length T vs. the statistical uncertainty to judge if the signal is stationary. 90

7.7 Residuals in L_2 norm for 5 simulations with different combination of grid and time step sizes. 91

7.8 Wave elevation and motion time histories in surge, heave and pitch DOF for 5 simulations conducted for discretization uncertainty analysis in bichromatic wave cases. 93

7.9 3-DOF RAOs at wave frequency 1 and wave frequency 2 calculated from the 5 simulations for discretization uncertainty analysis in bichromatic wave case. 94

7.10 3-DOF RAOs at wave sum-frequency and diff-frequency calculated from the 5 simulations for discretization uncertainty analysis in bichromatic wave case. 95

7.11 Mean surge offset and zero frequency surge QTF calculated from the 5 simulations for discretization uncertainty analysis in bichromatic wave case. 95

7.12 3D fit of all metrics in bichromatic wave case with green bar representing discretization uncertainty bounds for simulation G2T2 (denoted as red dot). 97

7.12 (Continued) 3D fit of all metrics in bichromatic wave case with green bar representing discretization uncertainty bounds for simulation G2T2 (denoted as red dot). 98

7.13 Comparison of JONSWAP spectrum random wave elevation histories from numerical simulations and experiment. 101

7.14 Power spectral density of surge responses of the semi-submersible platform under random waves. The blue shade denotes low frequency range (0.0354, 0.3536) Hz and orange shade denotes wave frequency range (0.3536, 0.9900) Hz. 102

7.15 Power spectral density of heave responses of the semi-submersible platform under random waves. The blue shade denotes low frequency range (0.0354, 0.3536) Hz and orange shade denotes wave frequency range (0.3536, 0.9900) Hz. 103

7.16 Power spectral density of pitch responses of the semi-submersible platform under random waves. The blue shade denotes low frequency range (0.0354, 0.3536) Hz and orange shade denotes wave frequency range (0.3536, 0.9900) Hz. 104

7.17 Validation of the PSD sums in low frequency range and wave frequency range of the semi-submersible platform under random waves. The red uncertainty bands represent the numerical uncertainty and the black ones represent the validation uncertainty. The heave PSD sum of low frequency is scaled up by a factor of 100. .. 105

LIST OF TABLES

TABLE Page

3.1 Main properties of the floating wind turbine system at model scale. 31

3.2 Stiffness properties of the linear mooring system; values are given with respect to the center of gravity. 32

3.3 Load conditions in the proposed dissertation study. Parameters are given at model scale. 33

3.4 Selected metrics for numerical uncertainty quantification in LC1-3. 34

3.5 Frequency ranges for PSD sums of responses in LC4. 34

4.1 Properties of the mooring lines attached to the OC5 floater. Subscript m denotes the mooring lines. 42

5.1 Refinement zones settings with grid sizes measured with baseline grid. The unit is meter for all values. 46

5.2 Relative grid size, number of cells and maximum skewness of all grids for the verification study. Refinement factors are computed by Eq. (2.52). (* The coarsest grid cannot converge with the finest time step size T5 because of the poor resolution at outer boundary. Hence a grid with refinement at outer boundary is generated specially for case G1T5.) 46

5.3 Numerical settings to solve the governing equations and the convergence tolerance or maximum iterations in pitch free decay case. 48

5.4 Time step size and relative time step for the verification study. 49

5.5 Grid and time step size combinations of 20 simulations for the discretization uncertainty analysis for pitch free decay case. The wall times in unit of hour are actual computing times using 240 cores on TAMU Terra cluster. 49

5.6 Numerical uncertainty analysis of the pitch natural period with G3T4 evaluated from 20 cases. 51

5.7 Uncertainty analysis of six pitch peaks with G3T4. 53

5.8 Pitch natural periods from numerical solutions and experiment. 57

5.9 Pitch damping coefficients generated from PQ analysis for numerical solutions in comparison with experiment. Critical damping is denoted as b_C. $\bar{U}_\phi$ is the mean value of numerical uncertainty. The damping coefficients for uncertainty bounds are computed using the marked extremes in the pitch decay motion (Figure 5.7). 57

5.10 Validation study for linear and quadratic damping coefficients obtained from the solutions with DM. The subscript ub and lb denote upper bound and lower bound of the uncertainty range. The validation uncertainty obtained by applying the mean uncertainty towards the solutions (DM$\pm\bar{U}_\phi$) is denoted with subscript $mean$ and DM$\pm \max(U_\phi)$ is denoted with subscript max. 57

6.1 Refinement zones for the computational domain. 61

6.2 Number of cells and refinement factors of grids for the verification study for regular waves. 61

6.3 Numerical settings to solve the governing equations and the convergence tolerance or maximum iterations in regular wave case. 62

6.4 Time step size and refinement factor of time step for the verification study for regular waves. 62

6.5 Selected metrics for numerical uncertainty quantification in regular wave case. 64

6.6 The statistical uncertainties of all metrics in selected time window $[20, 100]$ s. 66

6.7 Iterative uncertainties of all metrics obtained from 4 simulations with different number of outer iterations. 69

6.8 Grid and time step size combinations of 11 simulations for the discretization uncertainty analysis and the corresponding Courant number. 69

6.9 Discretization uncertainties of all the metrics obtained from 11 simulations with different grids and/or time step sizes. The error constants and order of convergence in space and time as described in Equation 2.51 are attached. 75

6.10 The total numerical uncertainties of all metrics for G2T2 simulation with 60 outer iterations per time step. 76

6.11 The component uncertainties, validation uncertainty and comparison error of investigated metrics for the semi-submersible platform under regular wave condition. Judgement of validation is determined by direct comparion of E and U_V. 77

7.1 Positions of the wave probes to be investigated with the x measured from wave paddle and y measured from side wall. 82

7.2 Wave characteristics of the benchmark focused wave case. 82

7.3 Number of cells and refinement factors of grids for the verification study for bichromatic waves. 87

7.4 Time step size and refinement factor of time step for the verification study for bichromatic waves. 87

7.5 Selected metrics for numerical uncertainty quantification in bichromatic wave case. 89

7.6 Grid and time step size combinations of 5 simulations for the discretization uncertainty analysis and the corresponding Courant number in bichromatic wave case. 92

7.7 Discretization uncertainties of all metrics in bichromatic wave case. The error constants and order of convergence in space and time as described in Equation 2.51 are attached. 99

7.8 The numerical uncertainties, total experiment uncertainty, and validation uncertainty of PDS sums in 3 DOFs for the semi-submersible platform under random wave condition. Judgement of validation is determined by direct comparion of E and U_V. 106

1. INTRODUCTION

1.1 Background and significance

The objective of this dissertation is to establish a robust and reliable verification and validation study for numerical analysis of FOWT using CFD simulations. Numerical tools have been commonly utilized to predict the responses of the FOWT in winds and waves due to their acceptable accuracy and lower cost-effectiveness compared to wave tank or in-situ experiments. A wide range of numerical tools like FAST, OrcaFlex etc. were most used in the simulations of FOWT. These numerical tools are based on potential flow, lumped mass, and Blade Element Momentum Theory (BEMT). The International Energy Agency (IEA) initiated an OC serial projects under the Wind Task 30 framework to test the performance of these numerical tools. Within the Offshore Code Comparison, Collaboration, Continued, with Correlation (OC5) project, it was found that the potential theory based numerical tools significantly under-predicted the responses of semi-submersible FOWTs under low-frequency nonlinear wave excitation [2]. The extended OC6 (OC5 with unCertainty) project commits to evaluate the applicability of CFD codes in simulations of FOWT [3].

High fidelity CFD simulations which accurately capture all non-linearities, and viscous damping effects were gradually picked up by researchers. In the OC6 project, cross verification and validation using CFD tools was focused to help tune and improve the potential theory based tools [4]. However, the uncertainty of the CFD simulations remained unveiled in most studies. In this dissertation, a procedure of systematic verification and validation study is introduced to robustly quantify the uncertainties embedded in the CFD simulations of the FOWT.

1.2 Literature Review

The compatibility of accurate prediction in hydrodynamics of floating offshore wind turbine with CFD codes has been reported in literature since OC3 project. The Hywind floater, which is a spar type floater adopted as primary model in OC3, was evaluated using CFD by Beyer et

al. [5] and Quallen et al. [6]. The CFD results aligned with simulation results obtained from mature numerical tools. The DeepCwind semi-submersible floater adopted by OC4, OC5 and OC6 was simulated by Tran et al. [7] under free decay motions and several regular wave conditions. Liu et al. [8] performed simulations of the DeepCwind floater under rough sea conditions. Liu et al. [9] established a fully coupled CFD analysis for the floater and turbine system with the hydrodynamic analysis of the floater included. Comparisons with experimental data were made in the above studies and fair agreement was reached in most metrics. Burmester et al. [10] conducted CFD simulations of surge decay motions of the DeepCwind floater, providing validated damping coefficients of the floater to engineering level tools. Wang et al. [11, 12, 13] extended the study toward pitch decay and regular waves conditions. In most of these studies, instead of systematic verification study, merely grid and time step convergence study was conducted which provides approximate discretization uncertainty.

It is well-known that the application of CFD relies heavily on both verification and validation [14]. Verification and Validation studies are common procedures to quantify the errors and uncertainties and assess the quality of a numerical model. Verification deals with numerical errors/uncertainties whereas validation deals with modeling errors/uncertainties. The term "error" refers to difference between numerical solution and exact solution, while "uncertainty" defines an interval that should contain the exact solution with a certain degree of confidence.

Verification is a purely mathematical exercise composed of code verification and solution verification. Code verification evaluates the errors by comparing numerical solutions to the exact solutions and verifies that a given numerical model correctly solves the equations. While solution verification estimates the numerical errors/uncertainties of a simulation for which the exact solution is generally unknown. The numerical uncertainty consists of statistical, iterative, spatial and temporal discretization uncertainties.

Validation is an engineering activity to estimate modeling errors/uncertainties. With validation we compare the numerical results to model test results to identify whether the mathematical model chosen is valid for the application at hand. In order to conduct a thorough validation, both

computational and experimental data should be accompanied by errors and uncertainties.

A procedure proposed by Eça et al. [15] is capable of quantifying the numerical uncertainty for CFD simulations. In the surge decay study from Burmester et al. [10], verification was performed using this method. The uncertainties for natural period and first negative surge peak were assessed in that work. In a posteriori work [16], the uncertainties were obtained using procedures from Oberhagemann et al. [17] and from Xing et al. [18] as well, proving that uncertainties estimated using Eça and Hoekstra method are more robust but more expensive as they require more simulation results. The method was adopted in a following work [13], where the numerical uncertainties of pitch natural period, pitch peaks and pitch damping coefficients for FOWT under pitch free decay motion were quantified. In that work, the numerical results were also validated against experiments and all metrics had achieved validation except for the quadratic pitch damping coefficient. Wang et al.[19] conducted a thorough uncertainty analysis on CFD solutions of nonlinear difference frequency wave loads on the fixed simplified DeepCwind platform. No attempt has yet been undertaken to thoroughly quantify the numerical uncertainties in the CFD simulations of free-floating moored semi-submersible platform of FOWT under multiple load conditions.

1.3 Dissertation Objective

The objective of this work is to develop a general method of systematic verification and validation study for CFD simulation of FOWT by investigation of a semi-submersible platform for FOWT, which includes:

- application of a dynamic mooring model coupled with CFD codes and compare with the linear mooring model;
- quantification of numerical uncertainties embedded in the CFD simulations of the semi-submersible platform under several load conditions;
- validation of the numerical results with the experiment measurements;
- generalization of the procedures to be applied in the CFD simulations of hydrodynamics of the support platform of FOWT.

1.4 Dissertation Organization

Chapter 1 introduces the current status of CFD simulations in studying the hydrodynamics of FOWT and the significance of verification and validation study in CFD simulations. Several methods to quantify the numerical uncertainties of the CFD simulations are also introduced.

Chapter 2 introduces the methods used in the CFD solver, the methods to obtain hydrodynamic responses and the procedures to perform the verification and validation study. The first part includes the governing equations, free surface model, turbulence model and wave generation models. The second part includes the definition of linear and quadratic damping coefficients, the Response Amplitude Operators (RAO), the Quadratic Transfer Functions (QTF) and the Power Spectral Density (PSD). The last part includes methods to quantify the iterative, discretization and statistical uncertainty. The last part also introduces a modern way to perform validation study.

Chapter 3 describes the test case of this work including the geometry of the semi-submersible platform, the properties of the model, the load conditions and the corresponding metrics in each condition to be investigated.

Chapter 4 describes the coupling between CFD codes and an in-house developed dynamic mooring module. The mooring properties of the semi-submersible platform and selection of the mooring coefficients are also presented in this chapter.

Chapter 5 presents the verification and validation study performed towards the semi-submersible platform under pitch free decay condition. The discretization uncertainty is quantified and validation is made against experiments.

Chapter 6 presents the results of verification and validation study of the semi-submersible platform under regular waves. The statistical, iterative and discretization uncertainties of the numerical results are quantified. Validation is made with given experimental uncertainty.

Chapter 7 presents the uncertainty quantification for semi-submersible platform under bichromatic waves and the validation of the hydrodynamic responses in random waves. A benchmark case to calibrate the CFD simulation of irregular waves is also made in this chapter.

Chapter 8 describes the generalized method to perform verification and validation study for

CFD simulations of hydrodynamics of FOWT. The previous verification and validation practices are also summarized and concludes in this chapter.

2.1 Flow solver

The numerical simulations are performed with community based open-source CFD code ReFRESCO [20] (`https://www.refresco.org`). The CFD code solves multi-phase unsteady incompressible viscous flows using the Navier-Stokes equations.

2.1.1 Navier-Stokes equations

For simulations with laminar flow, the flow is governed by the continuity and Navier-Stokes Equations:

$$\frac{\partial \rho}{\partial t} + \nabla \cdot (\rho \mathbf{u}) = 0, \tag{2.1}$$

$$\frac{\partial (\rho \mathbf{u})}{\partial t} + \nabla \cdot (\rho \mathbf{u}\mathbf{u}) = \nabla \cdot [\mu(\nabla \mathbf{u} + \nabla \mathbf{u}^T)] - \nabla p + \rho \mathbf{g}, \tag{2.2}$$

where $\mathbf{u}$ is the velocity vector, $\mathbf{g}$ the gravity vector, p denotes pressure, ρ and μ represent the density and viscosity of mixture of water and air to be determined in the following discussed free surface model.

For simulations with turbulence flow, the Reynolds Averaged form of the Navier-Stokes equations (RANS) is used:

$$\frac{\partial \rho}{\partial t} + \nabla \cdot (\rho \mathbf{u}) = 0, \tag{2.3}$$

$$\frac{\partial (\rho \mathbf{u})}{\partial t} + \nabla \cdot (\rho \mathbf{u}\mathbf{u}) = \nabla \cdot [(\mu + \mu_t)(\nabla \mathbf{u} + \nabla \mathbf{u}^T)] - \nabla \left(p + \frac{2}{3}\rho k \right) + \rho \mathbf{g}, \tag{2.4}$$

where velocity and pressure are ensemble averaged quantities plus fluctuation quantities, k denoting the turbulence kinetic energy and μ_t the eddy viscosity. Additional turbulence models are used to close the RANS equations which will be introduced in the following part.

The transport equations are discretized using a finite-volume approach with cell-centered collocated variables, in strong-conservation form, and a pressure correction equation based on the SIMPLE algorithm [21] is used to ensure mass conservation. Time integration is performed im-

plicitly with a second-order backward scheme.

2.1.2 Free surface model

The Volume Of Fluid (VOF) method is used to model the free surface between air and water [22]. The multi-phase flow is modeled by adopting a continuum fluid with time and space varying density and viscosity defined as:

$$\begin{aligned} \rho &= \alpha\rho_w + (1-\alpha)\rho_a, \\ \mu &= \alpha\mu_w + (1-\alpha)\mu_a. \end{aligned} \tag{2.5}$$

The subscript w and a stand for the material properties of water and air respectively, α denotes the air volume fraction in the cell with $\alpha = 0$ representing the cell is entirely filled by air. Air volume fraction α is governed by an additional transport equation of the form:

$$\frac{\partial \alpha}{\partial t} + \nabla \cdot (\alpha \mathbf{V}) = 0. \tag{2.6}$$

The convection term of the volume fraction transport equation is discretized with the interface capturing scheme ReFRICS [22].

2.1.3 Turbulence model

To solve for the additional two variables k and μ_t in the RANS equations Eq. 2.4 & 2.3, turbulence models are used to close the equations. The KSKL ($k - \sqrt{k}L$) turbulence model [23] is implemented in simulations of free decay test. Such model has advantages in convergence for CFD simulations with free surface and less unrealistic eddy-viscosity compared to the $k-\omega$ SST-2003 turbulence model [24]. However, for simulations of propagating waves, an over-production of turbulence level can be found beneath the surface waves [25] due to the finite strain rate. Therefore, the $k-\omega$ SST-IDDES turbulence model [26] is used in the wave cases.

KSKL turbulence model

Assigning $\Phi = \sqrt{k}L$ where L is the integral length scale of turbulence, the KSKL two-equation model is:

$$\frac{\partial \rho k}{\partial t} + \nabla \cdot (\rho \mathbf{u} k) = P_k - c_\mu^{3/4} \rho \frac{k^2}{\Phi} + \nabla \cdot \left(\frac{\mu_t}{\sigma_k} \nabla k \right), \tag{2.7}$$

$$\frac{\partial \rho \Phi}{\partial t} + \nabla \cdot (\rho \mathbf{u} \Phi) = P_\Phi - c_\mu^{3/4} (2 - c_{\epsilon 2}) \rho k + \nabla \cdot \left(\frac{\mu_t}{\sigma_\Phi} \nabla \Phi \right), \tag{2.8}$$

$$\mu_t = c_\mu^{1/4} \rho \Phi. \tag{2.9}$$

In the above two equation model, P_k and P_Φ are respectively the production terms of k and Φ; c_μ, $c_{\epsilon 2}$, σ_k and σ_Φ are constants. Details of these coefficients and production terms can be found in [27].

$k - \omega$ SST-IDDES turbulence model

The SST-IDDES is a hybrid zonal RANS-LES model which allows the more robust but higher costly Large Eddy Simulation (LES) be activated in part of the computational domain. The governing equations of the SST-IDDES model read as:

$$\frac{\partial \rho k}{\partial t} + \nabla \cdot (\rho \mathbf{u} k) = P_k - \rho \frac{k^{3/2}}{l_{IDDES}} + \nabla \cdot \left[(\mu + \sigma_k \mu_t) \nabla k \right], \tag{2.10}$$

$$\frac{\partial \rho \omega}{\partial t} + \nabla \cdot (\rho \mathbf{u} \omega) = P_\omega - \beta \rho \omega^2 + 2(1 - F_1) \sigma_{\omega 2} \rho \frac{\nabla k \cdot \nabla \omega}{\omega} + \nabla \cdot \left[(\mu + \sigma_\omega \mu_t) \nabla \omega \right], \tag{2.11}$$

$$\mu_t = \rho \frac{a_1 k}{\max(a_1 \omega, S F_2)}. \tag{2.12}$$

In the above equations, F_1 and F_2 denote the SST blending functions, P_k is the turbulence kinetic energy production term, σ_k, σ_ω, $\sigma_{\omega 2}$, β and a_1 are model constants. The IDDES length scale in Eq. 2.10 is defined as:

$$l_{IDDES} = \tilde{f}_d l_{RANS} + (1 - \tilde{f}_d) l_{LES}, \tag{2.13}$$

where $\tilde{f}_f$ is an empiric blending function, l_{RANS} and l_{LES} denote RANS length scale and LES length scale respectively. Details of the SST-IDDES model can be found at [26].

Comparative study with laminar flow

In the simulations of semi-submersible platform under waves, the solutions of wave loads are pressure dominated where the viscous effect should be negligible [28]. A laminar assumption can be made in such simulations and thereby reduces the computing costs. To study the difference brought by the application of turbulence model, a comparative study is made with two simulations under regular waves - one with the turbulence model and one without. The wave elevation, surge, heave and pitch motion time histories of both simulations are plotted at Figure 2.1. Nearly identical time histories are observed in wave elevation and 3-DOF motions. The root-mean-square-errors between four time histories are smaller than 0.1 % of the amplitude of each metric. The differences for surge, heave and pitch RAOs are within 1 %. Therefore, no turbulence model is applied in the simulations for the verification study of semi-submersible under waves.

2.1.4 Wave modelling

Regular waves

To account for the nonlinearity of the realistic regular waves, the elevation η of free surface and velocities u and w are defined using the Stokes 5$^{\text{th}}$ order wave theory at the inflow boundary.

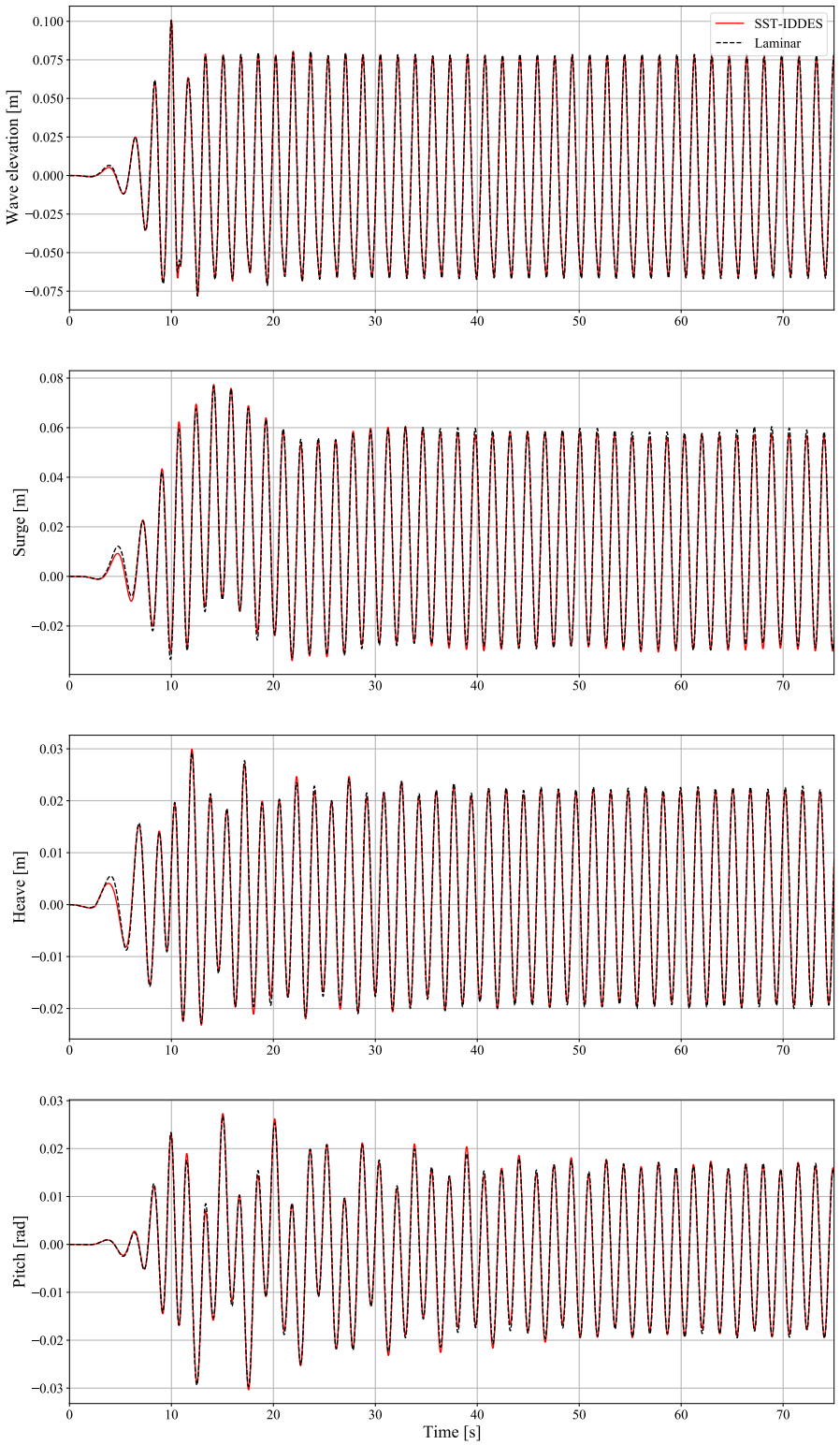

Figure 2.1: Comparison between simulations with and without a turbulence model.

$$
\begin{aligned}
\eta &= \sum_{n=1}^{5} \eta_n \cos[n(kx - \omega t)], \\
u &= \sum_{n=1}^{5} c_n \cosh[nk(z+d)] \cos[n(kx - \omega t)], \\
w &= \sum_{n=1}^{5} c_n \sinh[nk(z+d)] \cos[n(kx - \omega t)].
\end{aligned}
\tag{2.14}
$$

In the above equations, $k = 1/\lambda$ is the wave number which is inverse of wavelength λ, $\omega = 2\pi/T$ is the wave frequency derived from wave period T and d refers to the water depth. Together with the non-linear wave height H, the dispersion relation between these parameters is:

$$
\begin{aligned}
H &= \frac{2}{k}(ka + \kappa_1 (ka)^3 + \kappa_2 (ka)^5), \\
\omega^2 &= C_0 gk \tanh(kd),
\end{aligned}
\tag{2.15}
$$

where ka is the wave steepness coefficient with a as the first order wave amplitude. The details of the coefficients η_n, c_n, κ_1, κ_2 and C_0 can be found in [29].

Bichromatic waves

Bichromatic waves are generated using two superimposed linear sinusoidal waves which can be formulated as:

$$
\eta = \eta_1 \cos(k_1 x - \omega_1 t) + \eta_2 \cos(k_2 x - \omega_2 t), \tag{2.16}
$$

where η_1, η_2, k_1, k_2, ω_1 and ω_2 are respectively the wave amplitude, wave number and wave frequency of the two wave components. The wave number and wave frequency have to satisfy the dispersion relation:

$$
\omega^2 = gk \tanh(kd), \tag{2.17}
$$

with d as the water depth.

JONSWAP spectrum irregular waves

Irregular wave condition was investigated in the model test with a random wave whose energy spectrum follows a JONSWAP wave spectrum [30]. The wave spectrum is formulated as:

$$S(\omega) = \frac{\alpha g^2}{\omega^5} \exp\left[-\frac{5}{4}\left(\frac{\omega_p}{\omega}\right)^4\right] \gamma^r, \tag{2.18}$$

where

$$\begin{aligned} r &= \exp\left[-\frac{(\omega-\omega_p)^2}{2\sigma^2\omega_p^2}\right], \\ \sigma &= \begin{cases} \sigma_1 & \text{for } \omega \leq \omega_p, \\ \sigma_2 & \text{for } \omega > \omega_p. \end{cases} \end{aligned} \tag{2.19}$$

In the above equations $\omega_p = 2\pi/T_p$ denotes the peak wave frequency and the remaining constants α, γ, σ_1 and σ_2 are determined by the peak wave period T_p and the significant wave height H_s.

Wave absorption

To avoid reflected waves which would disturb the wave field in the regions of interest, wave absorption zones are defined in the computational domain adjacent to the inflow and outflow boundary. In the absorption zones, body force terms are added in the momentum equations to gradually modify the solution towards undisturbed waves. The body forces are proportional to the difference between the expected undisturbed wave orbital velocities $\hat{\mathbf{u}}$ and the actual velocities $\mathbf{u}$ as:

$$\rho f(\hat{\mathbf{u}} - \mathbf{u}). \tag{2.20}$$

The absorption zones are applied between an inner radius and an outer radius where the radius defined as the distance to the center of the structure. The function f controls the magnitude of

body force which increases from the inner edge to the outer edge to ensure smooth wave damping. A cosine function is adopted to describe f as:

$$f(x) = \frac{1}{2T_{ref}} f_{\max}(1 - \cos \pi x), \tag{2.21}$$

where T_{ref} is the reference wave period of the undisturbed waves and $f_{\max}$ is the dimensionless maximum body force value. Details of the wave absorption scheme can be found in Rapuc et al. [31].

2.2 Numerical schemes

The numerical methods utilized to solve the aforementioned governing equations including momentum, pressure, free surface and turbulence equations are introduced in this section.

2.2.1 Preconditioners

Preconditioners are transformation applied in solving a linear problem $\mathbf{Ax} = \mathbf{b}$ with iterative method to reduce the condition number of $\mathbf{A}$. The preconditioner $\mathbf{T} = \mathbf{P}^{-1}$ is applied to matrix $\mathbf{A}$ transforming the linear problem as solving for $\mathbf{AP}^{-1}\mathbf{y} = \mathbf{b}$ and $\mathbf{Px} = \mathbf{y}$. The application of precondition increases the rate of convergence in iterative methods and hence improve the performance of the iterative linear solvers.

JACOBI

The JACOBI preconditioner is one of the simplest preconditioners where

$$\mathbf{P} = \mathrm{diag}(\mathbf{A}). \tag{2.22}$$

It is efficient for diagonally dominant matrices. When solving momentum equation where velocities are minor, JACOBI preconditioner is the most efficient choice.

BJACOBI

The BJACOBI preconditioner is the block version of JACOBI preconditioner, i.e., considering JACOBI as using a 1×1 block in diagonals, BJACOBI uses larger blocks. The BJACOBI preconditioner reads:

$$\mathbf{P} = \sum_{i=1}^{p} \mathbf{R}_i^T (\mathbf{R}_i \mathbf{A} \mathbf{R}_i^T)^{-1} \mathbf{R}_i, \tag{2.23}$$

where $\mathbf{R}_i$ is the restriction matrix from the global numbering of unknowns to the local numbering of process i. An illustration of a BJACOBI preconditioner is presented as below:

$$\mathbf{A} = \begin{pmatrix} 2 & -1 & 0 & 0 & 0 & 0 \\ -1 & 3 & 0 & 0 & 0 & 0 \\ 0 & -1 & 4 & -1 & 0 & 0 \\ 0 & 0 & -1 & 5 & -1 & 0 \\ 0 & 0 & 0 & -1 & 6 & -1 \\ 0 & 0 & 0 & 0 & -1 & 7 \end{pmatrix} \quad \mathbf{P} = \begin{pmatrix} \begin{pmatrix} 2 & -1 \\ -1 & 3 \end{pmatrix}^{-1} & & \\ & \begin{pmatrix} 4 & -1 \\ -1 & 5 \end{pmatrix}^{-1} & \\ & & \begin{pmatrix} 6 & -1 \\ -1 & 7 \end{pmatrix}^{-1} \end{pmatrix}. \tag{2.24}$$

The BJACOBI preconditioner is suitable for problems with multiple physical variables where blocks can be formed to group the equations for one node. In solving all the transport equations in the flow solver, the BJOCABI preconditioner is applicable.

2.2.2 Solver methods

After the treatment of preconditioner, the linear system is solved by several choices of methods introduced in this subsection.

GMRES

The generalized minimal residual (GMRES) method [32] is an iterative method for the numerical solution of an indefinite non-symmetric system of linear equations. To solve for $\mathbf{Ax} = \mathbf{b}$, GMRES approximates the exact solution by the vector $\mathbf{x}_n$ that minimizes the Euclidean norm of the residual $\mathbf{r}_n = \mathbf{b} - \mathbf{A}\mathbf{x}_n$. The residual can be transformed to $\mathbf{r}_n = \mathbf{H}_n \mathbf{y}_n - |\mathbf{r}_0|$ by performing Arnoldi method [33] to get $\mathbf{H}_n$. Such treatment convert the problem to a linear least square problem to find $\mathbf{y}_n$.

The GMRES method is widely used in solving for transport equations with convection and diffusion terms where non-symmetric systems could present.

CG

The conjugate gradient (CG) method [34] is an iterative method to solve sparse positive definite system of linear equations. By solving $\mathbf{x}_n$ for $\mathbf{Ax} = \mathbf{b}$ in an iterative sense, the $\mathbf{x}_n$ is iterated as $\mathbf{x}_{n+1} = \mathbf{x}_n + \alpha_n \mathbf{p}_n$ with α_n and $\mathbf{p}_n$ calculated from the residual $\mathbf{r}_n = \mathbf{b} - \mathbf{A}\mathbf{x}_n$.

The CG method requires less storage and often faster convergence rate. Hence it is preferable to apply the CG method for linear system of equations with a symmetric matrix. In practice, the pressure Poisson equation is often solved using the CG method.

BCGS

The biconjugate gradient stabilized (BCGS) method [35] is an iterative method for the numerical solution of non-symmetric linear systems. It is a variant of biconjugate gradient method where the matrix $\mathbf{A}$ is multiplied with its conjugate transpose $\mathbf{A}^*$ and then solved in iterative sense using the CG method.

The BCGS method is applicable for non-symmetric systems and also requires less storage than the GMRES method does. It is chosen as a storage preserving substitute of the GMRES method where the CG method could not be applied.

2.2.3 Convective schemes

In solving for the partial differential equations, besides the variables in the cell center, values at the cell faces are also needed for calculation of convection terms. In order to obtain the cell face values, special discretization schemes are utilized to gather the information at the face center. An illustration of the discretization scheme in one dimension is shown in Figure 2.2. The flow direction is prescribed to east direction for illustration purpose.

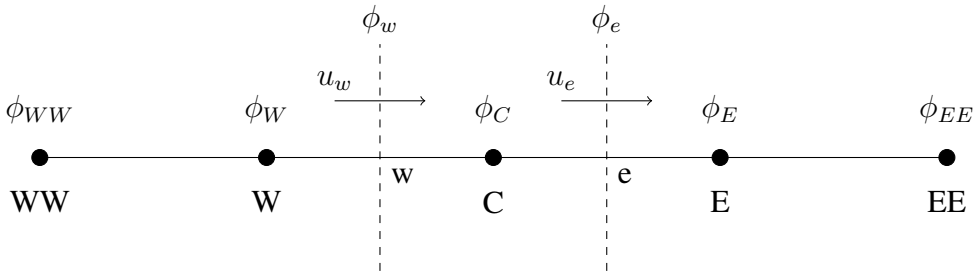

Figure 2.2: 1D illustration for convective flux discretization schemes.

1st order upwind

In the first order upwind scheme, the convected value ϕ at the cell face is adopted from the upstream node:

$$\phi_w = \phi_W, \quad \phi_e = \phi_C. \tag{2.25}$$

This scheme is specifically developed for strong convective flows with suppressed diffusion effects. It is simple to implement but only first order accurate.

QUICK

The quadratic interpolation for convective kinetics (QUICK) scheme [36] uses 3 points in the upstream with weights for quadratic interpolation for the cell face value. The scheme reads:

$$\begin{aligned} \phi_w &= \frac{6}{8}\phi_W + \frac{3}{8}\phi_C - \frac{1}{8}\phi_{WW}, \\ \phi_e &= \frac{6}{8}\phi_C + \frac{3}{8}\phi_E - \frac{1}{8}\phi_W. \end{aligned} \tag{2.26}$$

The QUICK scheme is third order accurate and is most appropriate for steady flow or quasi-steady highly convective flow.

HARMONIC

The harmonic scheme [37] is one of the total variation diminishing (TVD) scheme. Take ϕ_e as the interested cell face value, the scheme reads:

$$\begin{aligned} \phi_e &= \phi_C + \frac{1}{2}\psi(r)(\phi_C - \phi_W), \\ r &= \frac{\phi_E - \phi_C}{\phi_C - \phi_W}, \end{aligned} \tag{2.27}$$

where the limiter function $\psi(r)$ for the harmonic scheme is:

$$\psi(r) = \frac{r + |r|}{1 + |r|}. \tag{2.28}$$

The harmonic scheme is second order accurate and is able to resolve discontinuities without spurious oscillations.

ReFRICS

In order to maintain the step function of the volume fraction as it moves with the fluid, an interface capturing scheme ReFRICS [22] is implemented. Such scheme utilizes a blending function between a compressive scheme and a high-resolution scheme to determine the cell face value. The high-resolution scheme implemented in ReFRICS is the Harmonic scheme where the compressive scheme is chosen as the bounded downwind scheme with the limiter function as:

$$\psi(r) = \max\left\{0, \min\left\{2r, 2\right\}\right\}. \tag{2.29}$$

The value at the cell face is obtained with the blending function β:

$$\begin{aligned} \phi_e &= \beta\phi_{\text{compressive}} + (1 - \beta)\phi_{\text{highres}}, \\ \beta &= \frac{\cos(2\theta) + 1}{2}, \end{aligned} \tag{2.30}$$

where θ is the angle between the normal of air-water interface at the face center and the vector

from cell center of C to E.

2.3 Hydrodynamic responses

2.3.1 PQ analysis

Free decay data from a simulation or a model test can be used to derive the natural period and damping coefficients. Take surge DOF ($\mathbf{r} = x$) as example. Adopting a damping model with both linear and quadratic damping terms considered, the hydrodynamic damping force $F_{H,D}$ becomes

$$F_{H,D} = b_L \dot{x}(t) + b_Q |\dot{x}(t)| \dot{x}(t), \tag{2.31}$$

where b_L and b_Q denote the linear and quadratic damping coefficients, $\dot{x}(t)$ stands for the velocity of motion. Then, these two damping coefficients can be derived from the free decay motion data using a so-called PQ analysis [38]. The procedure is introduced below.

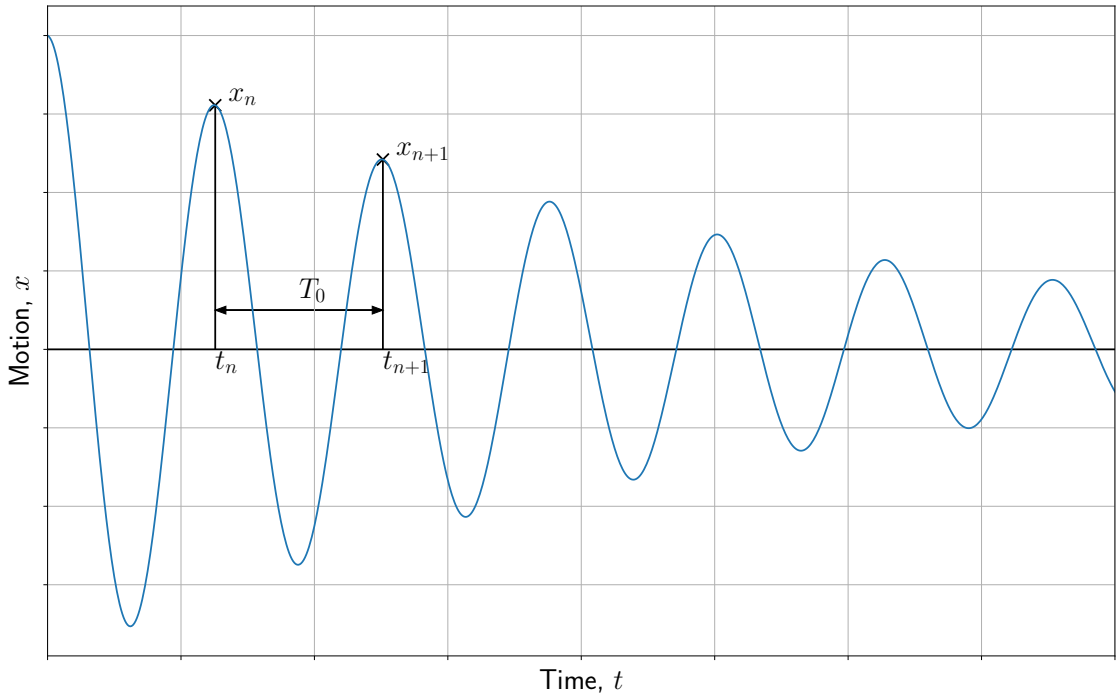

Figure 2.3: Time history of free decay motion for a weakly damped system.

A typical time history of free decay motion for a weakly damped system is illustrated in Figure 2.3. Consider the time instances t_n and t_{n+1} where two positive peaks x_n and x_{n+1} are reached, the loss of energy is given by

$$\begin{aligned}\Delta E &= \Delta E_k + \Delta E_p \\ &= \frac{1}{2}m\dot{x}_n^2 - \frac{1}{2}m\dot{x}_{n+1}^2 + \frac{1}{2}cx_n^2 - \frac{1}{2}cx_{n+1}^2.\end{aligned} \tag{2.32}$$

Here m is the total inertia of the system and c is the stiffness. For that the velocities $\dot{x}_n$ and $\dot{x}_{n+1}$ are zero, the energy loss is simplified as:

$$\Delta E = \frac{1}{2}c(x_n^2 - x_{n+1}^2). \tag{2.33}$$

By the assumption for weakly damped system, the stiffness can be approximated as $c \approx m\omega^2$. Furthermore, denoting $\bar{x}_n = \frac{1}{2}(x_n + x_{n+1})$ and $\Delta x_n = x_n - x_{n+1}$, Eq. (2.33) can be rewritten as:

$$\Delta E = m\omega^2 \bar{x}_n \Delta x_n. \tag{2.34}$$

On the other hand, the work done by the hydrodynamic damping force $F_{H,D}$ during time frame $[t_n, t_{n+1}]$ is:

$$W_D = \int_{t_n}^{t_{n+1}} \left[b_L \dot{x}^2(t) + b_Q |\dot{x}(t)| \dot{x}^2(t)\right] \mathrm{d}t. \tag{2.35}$$

Again for a weakly damped system, we can approximate the displacement $x(t)$ and the velocity $\dot{x}(t)$ in the time frame $[t_n, t_{n+1}]$ by:

$$\begin{aligned}x(t) &= \bar{x}_n \cos \omega t, \\ \dot{x}(t) &= -\omega \bar{x}_n \sin \omega t.\end{aligned} \tag{2.36}$$

Substituting the expressions into Eq. (2.35) yields:

$$W_D = b_L \pi \omega \bar{x}_n^2 + \frac{8}{3} b_Q \omega^2 \bar{x}_n^3. \tag{2.37}$$

For a free decay motion, the loss of energy is due to the work done by the damping force which gives

$$\frac{\Delta x_n}{\bar{x}_n} = \frac{\pi}{m\omega} b_L + \frac{8}{3m} b_Q \bar{x}_n. \tag{2.38}$$

Finally by assigning p and q as

$$\begin{aligned} & p = \frac{\pi}{m\omega} b_L, \quad q = \frac{8}{3m} b_Q, \\ \Leftrightarrow \quad & b_L = \frac{m\omega}{\pi} p, \quad b_Q = \frac{3m}{8} q, \\ \Leftrightarrow \quad & B_L = \frac{p}{2\pi} \times 100\% b_C, \quad B_Q = \frac{3T_n}{32\pi} q \times 100\% b_C, \end{aligned} \tag{2.39}$$

where $b_C = 2m\omega$ is the critical damping. the formula used in PQ analysis can be written as:

$$\frac{\Delta x_n}{\bar{x}_n} = p + q\bar{x}_n. \tag{2.40}$$

In order to obtain the values of p and q, the decrease of successive motion amplitudes normalized by the mean motion amplitude $\Delta x_n/\bar{x}_n$ is plotted as a function of the mean motion amplitude $\bar{x}_n$. By fitting the scattered points with a line representing the Eq. (2.40), the values of p and q can be obtained as the intercept with the y axis and the slope of the fitting line. Finally the linear and quadratic damping can be derived using Eq. (2.39). The above procedure is illustrated in Figure 2.4.

2.3.2 Response amplitude operator

The Response Amplitude Operators (RAOs) is computed by following equation:

$$RAO = H(\omega) = \frac{S_{\xi x}(\omega)}{S_{\xi\xi}(\omega)}, \tag{2.41}$$

where $H(\omega)$ is the Frequency Response Function (FRF), $S_{\xi x}(\omega)$ and $S_{\xi\xi}(\omega)$ are the cross spectral and power spectral densities of the wave height time series $\xi(t)$ and the response motion time series $x(t)$.

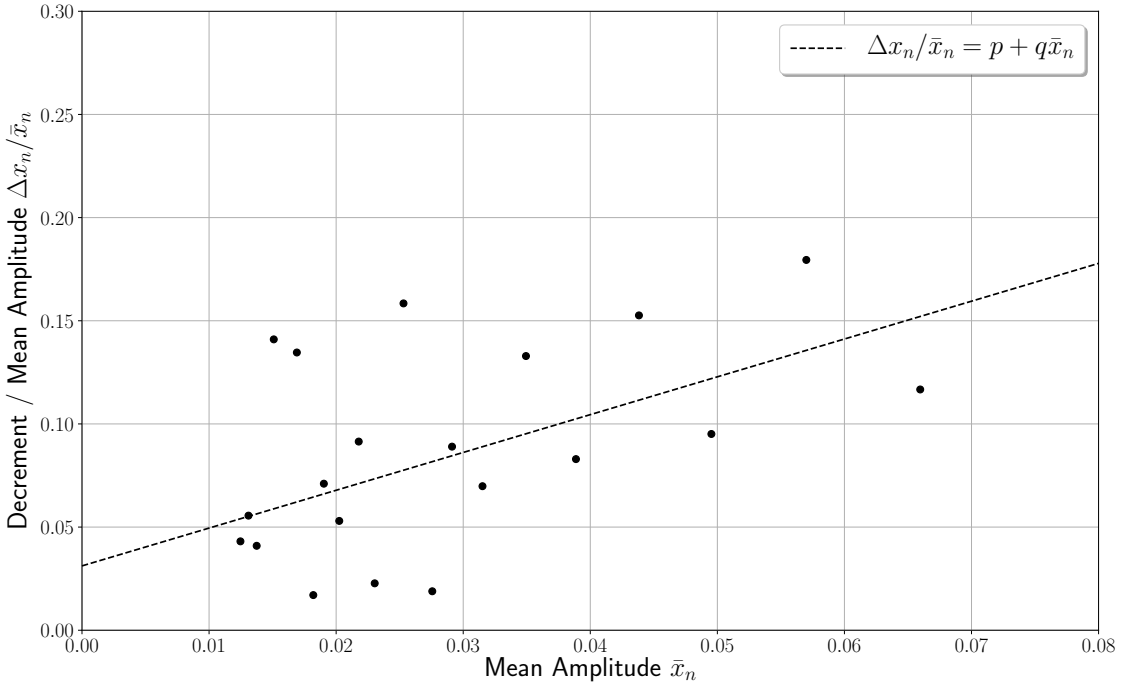

Figure 2.4: Illustration of PQ analysis.

2.3.3 Slow drift load QTF

The slow drift excitation load $F_d^{(2)}$ is defined as below [39]:

$$F_d^{(2)} = \sum_{j=1}^{N}\sum_{k=1}^{N} A_j A_k [T_{jk}^c \cos\{(\omega_k - \omega_j)t + (\epsilon_k - \epsilon_j)\} + T_{jk}^s \sin\{(\omega_k - \omega_j)t + (\epsilon_k - \epsilon_j)\}], \tag{2.42}$$

where A_j, A_k are wave amplitudes of the waves with frequencies ω_j, ω_k and phase ϵ_j, ϵ_k, T_{jk}^c and T_{jk}^s are the diff-frequency Quadratic Transfer Functions (QTF). For the regular wave with wave amplitude A, the diff-frequency QTF at zero frequency is obtained as

$$T_0 = \frac{\bar{F}}{A^2}, \tag{2.43}$$

where $\bar{F}$ is the mean of the load F.

For the bichromatic waves with wave amplitudes A_1 and A_2, the zero frequency QTF is:

$$T_0 = \frac{\bar{F}}{A_1^2 + A_2^2}. \tag{2.44}$$

2.3.4 Power spectral density sum

For irregular wave case, the spectrum of the motions of the semi-submersible is concerned. The sum in a certain frequency range of the discrete Power Spectral Density (PSD) function $S(f_i)$ of the response is investigated in this work. The PSD sum is computed as:

$$S_{sum} = \sum_{i=f_1}^{f_2} S(f_i)\Delta f, \tag{2.45}$$

where f_1, f_2 are the lower and higher limits of the frequency range, Δf is the frequency increment for the discrete PSD function $S(f_i)$.

2.4 Verification and Validation

Verification and Validation studies are common procedure to quantify the errors and uncertainties and assess the quality of a numerical model. Verification deals with numerical errors/uncertainties whereas validation deals with modeling errors/uncertainties. The term "error" refers to difference between numerical solution and exact solution, while "uncertainty" defines an interval that should contain the exact solution with a certain degree of confidence [14].

Verification is a purely mathematical exercise composed of code verification and solution verification. Code verification evaluates the errors by comparing numerical solutions to the exact solutions and verifies that a given numerical model solves the correct equations. While solution verification estimates the errors/uncertainties of a simulation for which the exact solution is generally unknown.

Validation is an engineering activity to estimate modeling errors/uncertainties. It requires experimental data to compare with. In order to conduct a thorough validation, both computational and experimental data should be accompanied by errors and uncertainties.

2.4.1 Verification

For present work, an analytic solution is not available for the pitch decay motion of the semi-submersible floater. Thus a solution verification is performed to estimate the numerical uncertainty. The goal is to find an interval that contains the exact solution with a 95% confidence:

$$\phi_{ij} - U_N \leq \phi_{exact} \leq \phi_{ij} + U_N, \tag{2.46}$$

where ϕ_{ij} is any integral or other functional derived from the numerical solution of grid i and time step setting j, ϕ_{exact} is the estimated solution and U_N is the estimated numerical uncertainty composed of round-off U_{ro}, iterative U_{it}, discretization U_d and statistical uncertainties U_{st} [14].

$$U_N = U_{ro} + U_{it} + U_d + U_{st}. \tag{2.47}$$

The round-off uncertainty is a consequence of the finite precision of the computers. The iterative uncertainty is unavoidable due to the non-linearity of the mathematical equations. The discretization uncertainty is a consequence of the approximations made to transform the partial differential equations of the continuum formulation into a system of algebraic equations. The statistical uncertainty is caused by using any finite time-averaged measurement for analysis, assuming that random physical processes have become stationary after a start-up time.

Iterative uncertainty

In practice, the round-off uncertainty is made suitably negligible thank to double-precision arithmetic. When the iterative uncertainty is controlled within a level of two order of magnitude below the discretization uncertainty, it is considered as negligible [40]. However, in complex problem this is not always feasible and therefore an investigation into the residual level is required to estimate iterative uncertainty. An extrapolation procedure [41] to estimate iterative uncertainty U_{it} from iterative error ϵ_{it} can be done by using the convergence tolerance at each time step δ_{it} as

independent variable in the following expression

$$\epsilon_{it} = \phi_{it} - \phi_{0it} = \alpha_{it} e^{H(\delta_{it})\beta_{it}}, \tag{2.48}$$

where ϕ_{it} and ϕ_{0it} are the solution associated with δ_{it} and the estimated value of it. The function $H(\delta_{it})$ takes two alternatives: $H(\delta_{it}) = \ln(\delta_{it})$ or $H(\delta_{it}) = -1/\delta_{it}^{p_{it}}$, leaving three unknowns $(\alpha_{it}, \beta_{it}, \phi_{0it})$ or four unknowns (with additional p_{it}) to be determined. And these constants can be solved in the least-squares sense by minimizing the standard deviation

$$\sigma_{it} = \sqrt{\frac{\sum_{i=1}^{n_{it}} \left[\phi_{it} - (\phi_{0it} + \alpha_{it} e^{H(\delta_{it})\beta_{it}})\right]^2}{n_{it} - k}}, \tag{2.49}$$

where n_{it} is the number of simulations and k is the number of unknowns. Finally the iterative uncertainty is given by:

$$U_{it} = F_S |\epsilon_{it}| + \sigma_{it}, \tag{2.50}$$

where $F_S = 1.25$ is the safety factor.

Discretization uncertainty

A procedure proposed by Eça and Hoekstra [15] to estimate discretization uncertainty was used in present work. For unsteady calculations, basic equation to estimate the discretization error is:

$$\epsilon_d \simeq \delta_d = \phi_{ij} - \phi_0 = \alpha_x h_i^{p_x} + \alpha_t t_j^{p_t}. \tag{2.51}$$

In above equation, ϕ_0 is the estimate of the exact solution which is an extrapolated value on the fit, α is a constant to be determined, p is the observed order of grid convergence, the subscripts x and t stand for space and time dependent variables, h_i and t_j are the relative grid size and time step to be estimated with:

$$h_i = \left(\frac{N_{cell_1}}{N_{cell_i}}\right)^{1/n_d}, \; t_j = \frac{\Delta t_j}{\Delta t_1}, \tag{2.52}$$

where N_{cell_i} is the number of cells of grid i, $n_d = 3$ for current three dimensional cases, Δt_j is the

time step size of setting j, subscript 1 refers to the finest grid and time step. Thus, the finest grid and time step are represented with $h_1 = 1$ and $t_1 = 1$.

There are five unknowns in Eq. 2.51 which require solutions from at least five sets of grid and time step to solve. Eça and Hoekstra recommended to use at least one set more than unknowns in order to estimate the errors in a least-square sense. That is, ϕ_0, α_x, p_x, α_t and p_t are determined from the minimum of the function

$$S(\phi_0, \alpha_x, p_x, \alpha_t, p_t) = \sqrt{\sum_{i=1}^{n_g} \sum_{j=1}^{n_t} w_{ij} \left[\phi_{ij} - (\phi_0 + \alpha_x h_i^{p_x} + \alpha_t t_j^{p_t})\right]^2}, \tag{2.53}$$

in which n_g and n_t are the number of grids and time step settings, w_{ij} is a weight to give more emphasis to certain grid and time step combination as e.g. for the finer grid and time step. By solving Eq. 2.53 a fit of the solutions with respect to grid size and time step size can be obtained. The corresponding standard deviations may be written as:

$$\sigma_d = \sqrt{\frac{\sum_{i=1}^{n_g} \sum_{j=1}^{n_t} n_g n_t w_{ij} \left[\phi_{ij} - (\phi_0 + \alpha_x h_i^{p_x} + \alpha_t t_j^{p_t})\right]^2}{n_g n_t - 5}}. \tag{2.54}$$

In addition, a data range parameter is determined as

$$\Delta_\phi = \frac{(\phi_{ij})_{\max} - (\phi_{ij})_{\min}}{n_g n_t - 1}, \tag{2.55}$$

where $(\phi_{ij})_{\max}$ and $(\phi_{ij})_{\min}$ are the maximum and minimum value of ϕ_{ij} among all simulations. When $\sigma_d < \Delta_\phi$, the error estimation is judged as "good" and a safety factor $F_S = 1.25$ is used. Otherwise, a safety factor of $F_S = 3$ is used for "bad" error estimation. Finally, the discretization uncertainty can be obtained from:

For $\sigma_d < \Delta_\phi$,

$$U_d(\phi_{ij}) = F_S \epsilon_d(\phi_{ij}) + \sigma_d + |\phi_{ij} - \phi_{fit}|. \tag{2.56}$$

For $\sigma_d \geq \Delta_\phi$,

$$U_d(\phi_{ij}) = F_S \frac{\sigma_d}{\Delta_\phi} \left[\epsilon_d(\phi_{ij}) + \sigma_d + |\phi_{ij} - \phi_{fit}|\right]. \tag{2.57}$$

In above equations, ϕ_{fit} is value on the fit plane with the same grid spacing and time step as ϕ_{ij}.

Statistical uncertainty

The motion time series of the floater responses to the regular waves can be crop into a piece of stationary signals after applying a Transient Scanning Technique (TST) [42]. Towards the stationary finite length (T) of motion histories $\phi(t)$, an auto-covariance method can be utilized to obtain the statistical uncertainty of the mean motion. The auto-correlation function $C_{xx}(\tau)$ can be calculated from Wiener-Khinchine relation as

$$C_{xx}(\tau) = \int_0^\infty S_{xx}(f) \cos(2\pi f \tau) \mathrm{d}f, \tag{2.58}$$

where the auto spectral density function $S_{xx}(f)$ is computed from the Fourier transform $\Phi(f)$ of the motion histories $\phi(t)$:

$$\begin{aligned} S_{xx}(f) &= \frac{2}{T}|\Phi(f)|^2, \\ \Phi(f) &= \int_0^T \left[\phi(t) - \bar{\phi}\right] e^{-i2\pi f t} \mathrm{d}t. \end{aligned} \tag{2.59}$$

In the above equation, $\bar{\phi}$ is the mean value of the motion histories $\phi(t)$. The estimator for statistical uncertainty ϵ_{st} is

$$\epsilon_{st} = \sqrt{\frac{1}{T} \int_0^T \left(1 - \frac{\tau}{T}\right)^2 C_{xx}(\tau) \mathrm{d}\tau}. \tag{2.60}$$

The final statistical uncertainty is obtained by applying the safety factor $F_S = 2$ to the estimator:

$$U_{st} = F_S \epsilon_{st}. \tag{2.61}$$

To identify the transient phase in the early stage of the signal, the statistical uncertainty is calculated from the end of the signal by selecting $[t_{end} - T, t_{end}]$ for each finite length of time T. By plotting U_{st} versus T with logarithmic scale, the range where the data shows $1/T$-behaviour is judged as stationary. The time length T where the minimum statistical uncertainty is obtained is chosen as the optimal section for derivation of metrics. The process of TST is illustrated in Figure 2.5.

Total numerical uncertainty

The total numerical uncertainty is obtained by combination of the iterative, discretization and statistical uncertainty. The statistical uncertainty contributes to the numerical uncertainty independently, while the iterative and discretization uncertainty do not [41]. Therefore, a conservative total numerical uncertainty is obtained by:

$$U_N^2 = (U_{it} + U_d)^2 + U_{st}^2. \tag{2.62}$$

2.4.2 Validation

The approach to CFD solution validation developed by [43] is utilized. By defining the predicted solution from the simulation as ϕ_{ij} and the experimentally measured value as ϕ_{exp}, the comparison error E is derived as

$$E = \frac{\phi_{exp} - \phi_{ij}}{\phi_{exp}}. \tag{2.63}$$

The absolute value of the comparison error E should be bounded by the uncertainty U_E with 95% confidence. The uncertainty U_E can be expressed as

$$U_E^2 = U_{exp}^2 + U_S^2, \tag{2.64}$$

where U_{exp} is the experimental uncertainty, and U_S the uncertainty in the simulation. The simula-

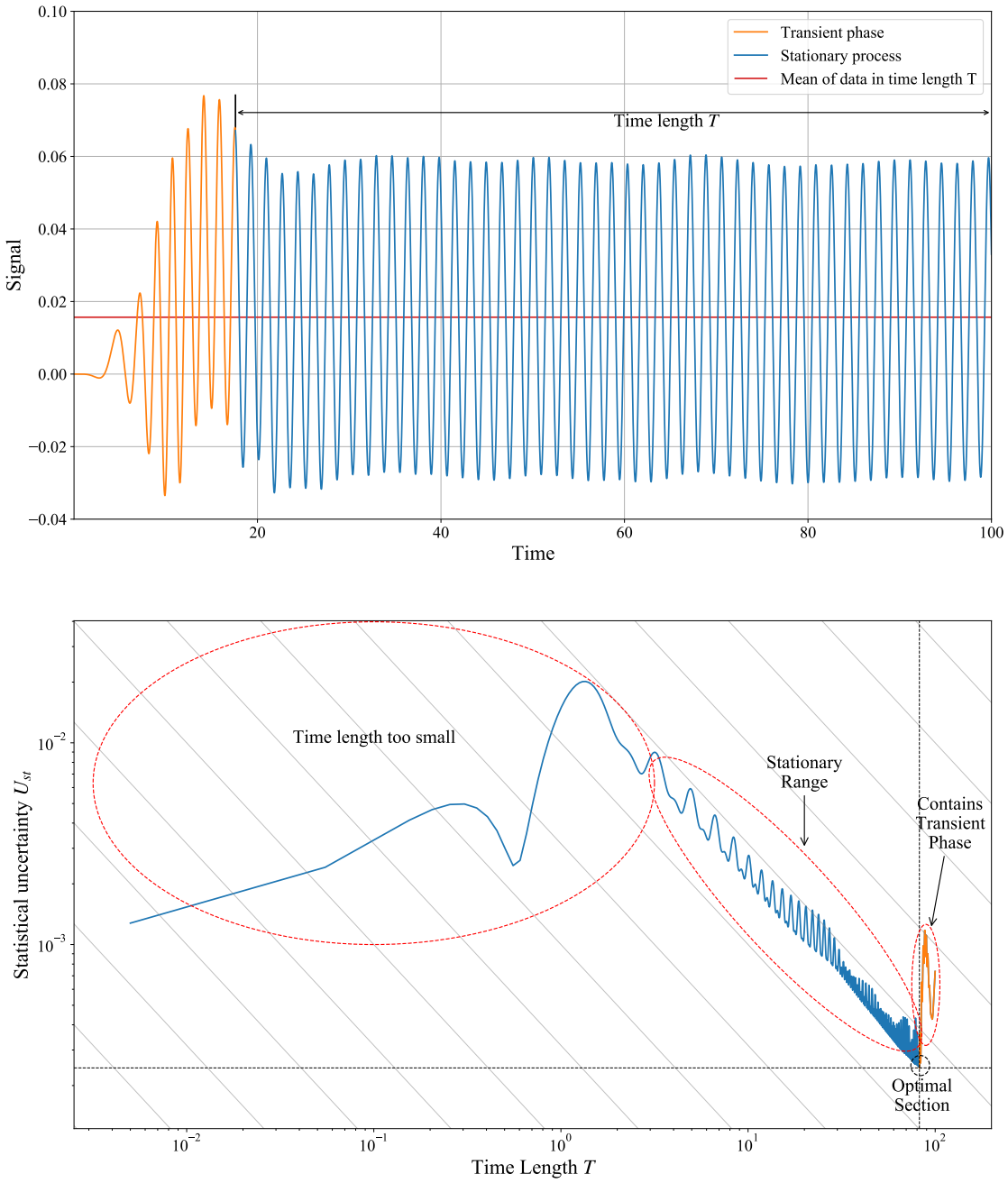

Figure 2.5: Illustration of Transient Scanning Technique (TST).

tion uncertainty U_S can be further expanded as

$$U_S^2 = U_N^2 + U_I^2 + U_{SMA}^2, \tag{2.65}$$

where U_N is the numerical uncertainty obtained from Equation 2.62, U_I is the input parameter uncertainty, and U_{SMA} is the simulation modeling uncertainty arising from modeling assumptions. Since estimation of U_{SMA} is impossible, the combination of all remaining uncertainties is defined as the validation uncertainty U_V

$$U_V^2 = U_{exp}^2 + U_N^2 + U_I^2. \tag{2.66}$$

Besides the numerical uncertainty U_N which can be estimated from verification study, the experimental uncertainty U_{exp} is typically provided with the experimental data. The input parameter uncertainty U_I may be estimated with a local sensitivity method as

$$U_I^2 = \sum_{i=1}^{n_v} \left(\frac{\partial S_\phi}{\partial X_i} U_{X_i} \right)^2, \tag{2.67}$$

where n_v is the number of input variables X_i that have a standard uncertainty U_{X_i}. Or a statistical Uncertainty Quantification (UQ) analysis as in [44].

If $|E|$ is less than the validation uncertainty U_V then validation is achieved at the U_V level.

3. TEST CASE DESCRIPTION

3.1 FOWT model

The semi-submersible FOWT originally developed by DeepCWind consortium is used in the proposed study. A model test campaign was conducted in MARIN's offshore basin with 1/50th Froude scale applied to the tower and platform [2]. The performance matched wind turbine MSWT [45] was mounted on the floater in the model test. Repeated test campaign was reinforced to quantify the experimental uncertainty [46], but only for wave tests. To be consistent with experimental setup in the further validation study, simulations in this study are performed at model scale. Since the rotor did not rotate during the respective model tests, only the floater is modeled and used throughout this study. The geometry of the floater at model scale is shown in Fig. 3.2. However, the mass and moment of inertia properties for the whole FOWT system including tower, RNA and linear mooring system are used. Detailed properties are summarized in Table 3.1. Further details of the FOWT system can be found in Robertson et al. [1].

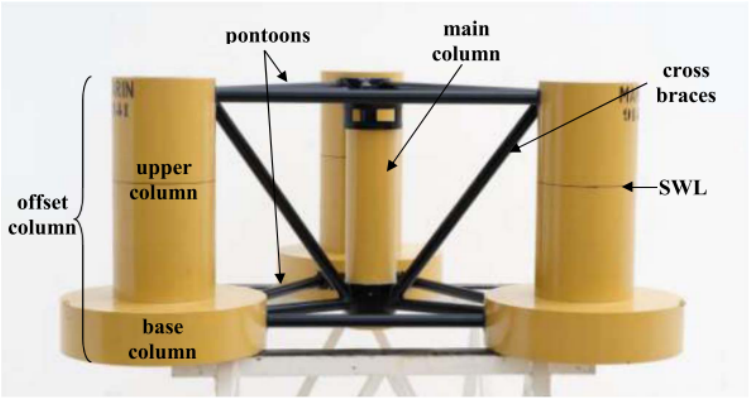

Figure 3.1: DeepCWind semi-submersible floater for the 1/50th scale model tests, reprinted from [1].

The coordinate system implemented follows the right-handed criteria with the origin coinciding with the center of gravity (COG) of the FOWT system, the x-coordinate pointed in positive surge,

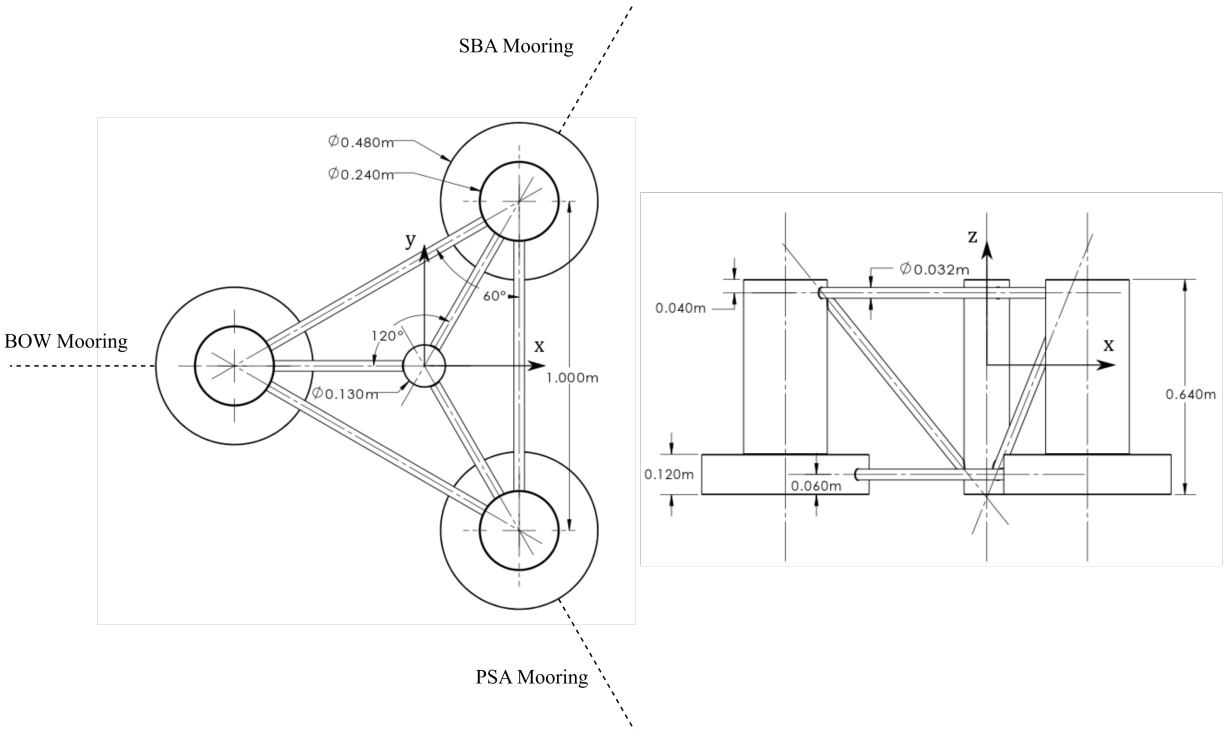

Figure 3.2: Top view and side view sketch of the 1/50th scaled floater. Mooring arrangement is depicted in top view sketch.

Table 3.1: Main properties of the floating wind turbine system at model scale.

Designation	**Symbol**	**Value**	**Unit**
Total draft	D	0.4	m
Total mass	M	111.664	kg
Center of gravity below SWL	COG	0.1614	m
Roll radius of gyration	r_ϕ	0.6526	m
Pitch radius of gyration	r_θ	0.6676	m
Yaw radius of gyration	r_ψ	0.6264	m

y in positive sway and z in positive heave directions. The floater consisted of one center column for tower mounting and three vertical offset columns distributed with 120° around the center column. Columns were connected by pontoons and braces.

In the model test, the platform was moored with three catenary lines spread 120° apart from

each other similar to the offset columns. Mooring lines were attached to the top of the base columns which was at a depth of 0.28 m below the SWL and at a radius of 0.8174 m from the platform centerline. The anchors were located at the seabed and at a radius of 16.752 m from the centerline. Two mooring models are implemented in the free decay and regular wave load cases for comparison. The first one is linear mooring model which utilize the stiffness matrix as listed in Table 3.2 to simulate the linear restoring forces provided by mooring lines. The second mooring model is a dynamic mooring model utilizing a coupled mooring module MOORING3D. Detailed properties of the dynamic mooring model will be discussed at the following section with the coefficients calibrated .

Table 3.2: Stiffness properties of the linear mooring system; values are given with respect to the center of gravity.

Designation	**Symbol**	**Value**	**Unit**
Surge	K_{xx}	33.84	N/m
Sway	K_{yy}	29.40	N/m
Heave	K_{zz}	7.76	N/m
Roll	$K_{\phi\phi}$	12.209	Nm/rad
Pitch	$K_{\theta\theta}$	17.013	Nm/rad
Yaw	$K_{\psi\psi}$	19.175	Nm/rad

3.2 Load conditions

Four load conditions are simulated using the coupled CFD-Mooring code as listed in Table 3.3. The waves are uni-directional and propagate in positive x direction which is the surge direction of the platform. Additionally, the JONSWAPS random waves generated in LC4 is a superposition of linear wave components taken from spectral analysis of experimentally measured wave elevations. The amplitude spectrum of the wave elevation measured in the experiment is shown at Figure 3.3. The sampling frequency is $\Delta f = 6.71 \times 10^{-4}$ Hz. Experimental data of motion, load time series and wave elevation history for LC1, 2 & 4 are available for validation study, while there is

no experimental data for LC3. Since direct numerical uncertainty quantification for LC4 is super costly, numerical uncertainty quantifies for LC3 is supplemented as a standard uncertainty bounds for LC4.

Table 3.3: Load conditions in the proposed dissertation study. Parameters are given at model scale.

LC Number	**Description**	**Parameters**
LC1	Pitch free decay	Initial pitch angle 4°
LC2	Regular waves	$T = 1.711$ s, $H = 0.142$ m
LC3	Bichromatic waves	$T_1 = 1.711$ s, $H_1 = 0.142$ m and $T_2 = 1.273$ s, $H_2 = 0.080$ m
LC4	Random waves	JONSWAP spectrum $T_p = 1.711$ s, $H_s = 0.142$ m

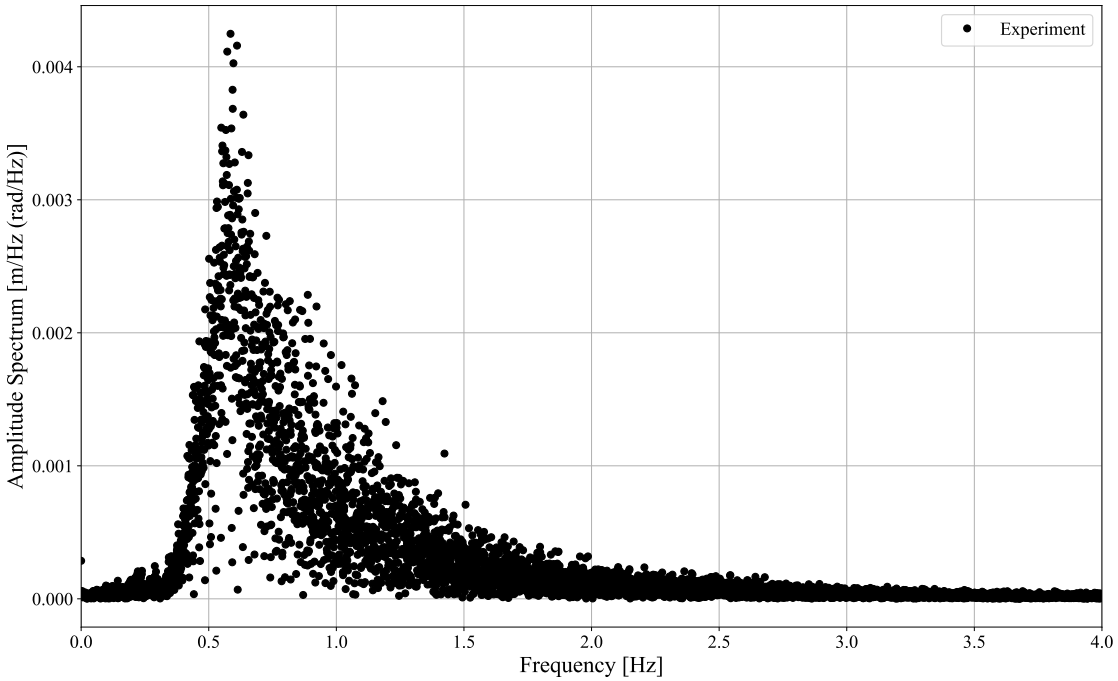

Figure 3.3: The amplitude spectrum of LC4 - JONSWAP random waves analyzed from experimental data.

For the first three load conditions where numerical uncertainty are quantified, the metrics that are used for uncertainty quantification are listed in Table 3.4. For LC4 with JONSWAP spectrum random waves, PSD sums of surge, heave and pitch motion are used in the validation against the experiment measurement. The frequency ranges for PSD sums are listed in Table 3.5. Experimental uncertainties are only given for wave tests. Therefore, validation study of LC1 is conducted with an assumed experimental uncertainty.

Table 3.4: Selected metrics for numerical uncertainty quantification in LC1-3.

LC Number	**Metrics**	**Symbol**
LC1	Pitch natural period	T_{nP}
LC1	Pitch motion peaks	$P_1, P_2, \ldots$
LC1	Pitch damping coefficients	p, q
LC2	Mean surge offset	MSO
LC2	Zero frequency surge QTF	SQTF_0
LC2	RAOs at wave frequency	$\mathrm{SRAO}, \mathrm{HRAO}, \mathrm{PRAO}$
LC2	RAOs at double wave frequency	$\mathrm{SRAO}_2, \mathrm{HRAO}_2, \mathrm{PRAO}_2$
LC3	Mean surge offset	MSO
LC3	Zero frequency surge QTF	SQTF_0
LC3	RAOs at ω_1	$\mathrm{SRAO}_1, \mathrm{HRAO}_1, \mathrm{PRAO}_1$
LC3	RAOs at ω_2	$\mathrm{SRAO}_2, \mathrm{HRAO}_2, \mathrm{PRAO}_2$
LC3	RAOs at $\omega_1 + \omega_2$	$\mathrm{SRAO}_+, \mathrm{HRAO}_+, \mathrm{PRAO}_+$
LC3	RAOs at $\omega_2 - \omega_1$	$\mathrm{SRAO}_-, \mathrm{HRAO}_-, \mathrm{PRAO}_-$

Table 3.5: Frequency ranges for PSD sums of responses in LC4.

LC Number	Low frequency window	Wave frequency window
LC4	0.0354 Hz - 0.3536 Hz	0.3536 Hz - 0.9900 Hz

4.1 Methodology

The fluid equations are coupled with the structural equations of motion in the CFD simulations. With the hydrodynamic force $\mathbf{F}_H$, the mooring force $\mathbf{F}_{moor}$ and other external mechanical forces $\mathbf{F}_{ext}$, the six degrees-of-freedom equations-of-motion may be written as:

$$\mathbf{M}\ddot{\mathbf{r}} = \mathbf{F}_H - \mathbf{F}_{moor} - \mathbf{F}_{ext}. \tag{4.1}$$

Here, $\mathbf{M}$ denotes the mass and $\ddot{\mathbf{r}}$ represents the second order time derivative of the state vector $\mathbf{r} = (x, y, z, \phi, \theta, \psi)$. To solve the nonlinear equations-of-motion caused by the nonlinear relation between $\mathbf{F}_H$ and $\mathbf{r}$, Backward-Difference 2$^{\text{nd}}$ order time-implicit predictor-corrector scheme (BDF2) is used. The communication between flow solution and rigid body system is done at the time loop level (predictor) and at the outer loop level iterative (corrector) step, at each 10$^{\text{th}}$ iteration. Convergence is claimed when residuals in state vector $\mathbf{r}$ fell under a tolerance of 1×10^{-5} in one corrector step or 1×10^{-6} between consequent corrector steps within one time step.

By coupling with MOORING3D, the mooring forces are derived from the displacement and velocity vectors of the floater computed in the motion solver. The coupling procedure is illustrated in Figure 4.1. MOORING3D communicated with motion solver to update the mooring forces at every time step. The flow field in mooring force calculation is derived within MOORING3D instead of passing from the flow solver, allowing the mooring forces to be accurately calculated in flow fields caused by waves or currents.

MOORING3D utilizes FEM to solve the partial differential equations that govern the configuration of mooring chains. the mooring chains are governed by the following dynamic equation and stretching constraint equation

$$\mathbf{M}\frac{\partial^2 \mathbf{l}}{\partial t^2} - \frac{\partial}{\partial s}\left(\tilde{\lambda}\frac{\partial \mathbf{l}}{\partial s}\right) = \mathbf{q}, \tag{4.2}$$

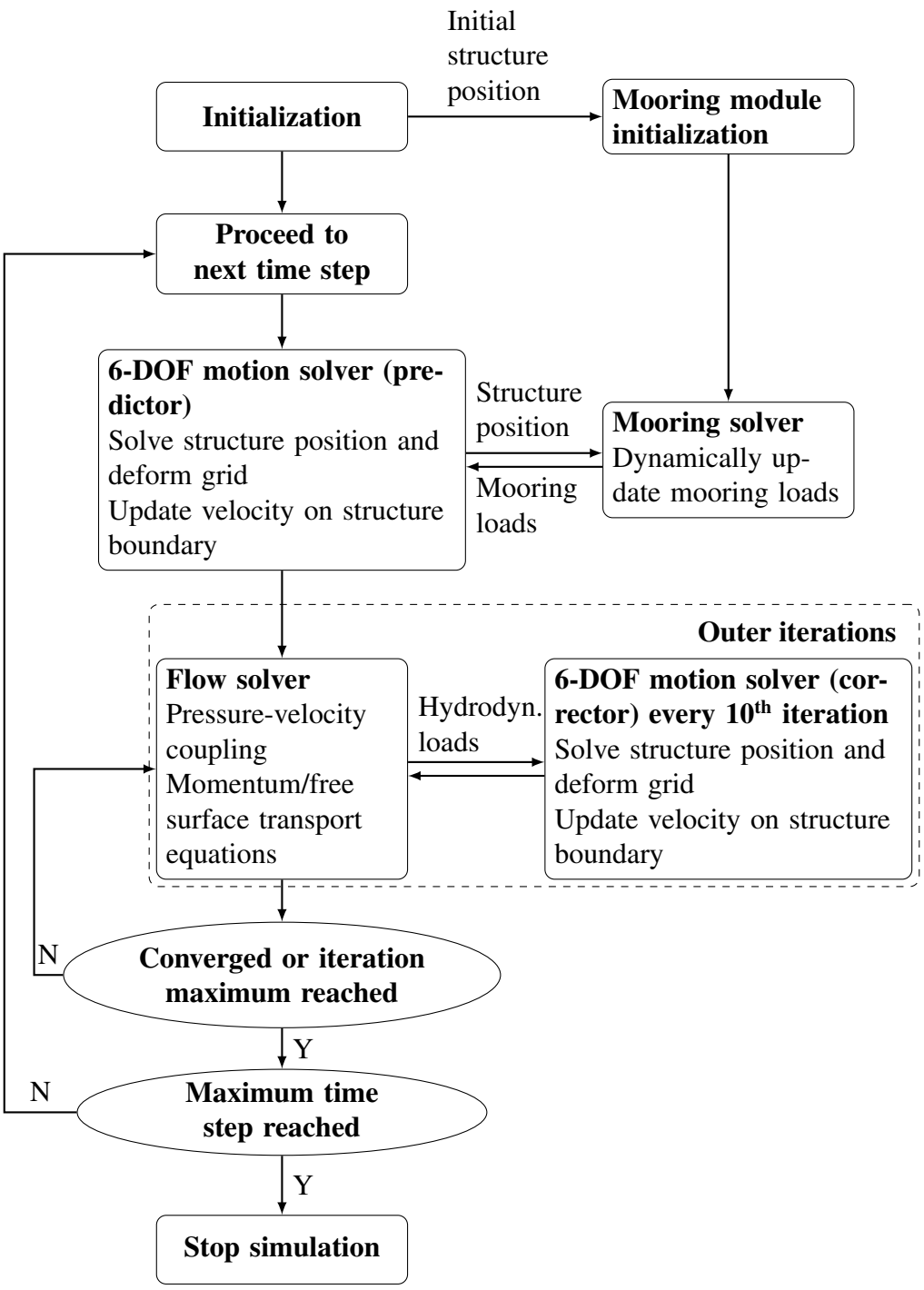

Figure 4.1: The simulation workflow of the coupled code of ReFRESCO and MOORING3D.

$$\left(\frac{\partial \mathbf{l}}{\partial s} \cdot \frac{\partial \mathbf{l}}{\partial s}\right)\left(1-\frac{\tilde{\lambda}}{EA}\right)^2 = 1. \tag{4.3}$$

In the above equation, $\mathbf{M}$ is the virtual mass matrix of the mooring chains including added mass; $\mathbf{l} = \mathbf{l}(s,t)$ is the instantaneous configuration of a rod as a function of s, the deformed arc length along the rod and time t; $\tilde{\lambda} = T/(1+\varepsilon)$ is the effective tension where T represents the tension and $\varepsilon = T/(EA)$ the strain; $\mathbf{q}$ is the external force on the mooring chains per unit length consist of hydrostatic, hydrodynamic and gravitational forces. The hydrodynamic forces are composed by added mass, drag and Froude-Krylov force where the first two terms are predicted with Morrison equation.

$$\begin{aligned}
\mathbf{q}^I =& \rho A C_{Mn}\mathbf{N}\left(\mathbf{a}-\frac{\partial^2 \mathbf{l}}{\partial t^2}\right) + \rho A C_{Mt}\mathbf{T}\left(\mathbf{a}-\frac{\partial^2 \mathbf{l}}{\partial t^2}\right), \\
\mathbf{q}^D =& \frac{1}{2}\rho D C_{Dn}\mathbf{N}\left(\mathbf{v}-\frac{\partial \mathbf{l}}{\partial t}\right)\left|\mathbf{N}\left(\mathbf{v}-\frac{\partial \mathbf{l}}{\partial t}\right)\right| \\
&+ \frac{1}{2}\rho D C_{Dt}\mathbf{T}\left(\mathbf{v}-\frac{\partial \mathbf{l}}{\partial t}\right)\left|\mathbf{T}\left(\mathbf{v}-\frac{\partial \mathbf{l}}{\partial t}\right)\right|.
\end{aligned} \tag{4.4}$$

In the above equations, A is the cross section area of the mooring chains, D is the diameter; ρ, $\mathbf{a}$ and $\mathbf{v}$ denote the density, acceleration and velocity of the water at each point of the rod respectively; $\mathbf{N}$ and $\mathbf{T}$ are transfer matrices to the normal and tangential directions of the mooring chain coordinate system; C_{Mn}, C_{Mt}, C_{Dn} and C_{Dt} are normal added mass coefficient, tangential added mass coefficient, normal drag coefficient and tangential drag coefficient respectively.

The partial differential equations (4.2) and (4.3) were then discretized using Galerkin's method [47] in space and a Newmark beta method [48] was employed for time integration. A convergence tolerance was set at 1×10^{-6} for the computation.

4.2 Sensitivity study on mooring line coefficients

The coupled ReFRESCO-MOORING3D is used throughout all the simulations of FOWT. However, before the application to the FOWT simulation, a sensitivity study is conducted to calibrate the coefficients of the mooring system properties.

In the model test, the platform was moored with three catenary lines spread 120° apart from each other similar to the offset columns (see Figure 3.2). Mooring lines were attached to the top of the base columns which was at a depth of 0.28 m below the SWL and at a radius of 0.8174 m from the platform centerline. The anchors were located at the seabed and at a radius of 16.752 m from the centerline. The properties of the mooring lines are summarized in Table 4.1.

Most properties of the mooring lines in the table are taken from the experimental report except for the coefficients. The drag and added mass coefficients for the mooring lines are undetermined in the experiment and thus need to be calibrated. Previous investigation from Gueydon et al. [49] aiming for reproducing the surge restoring forces provided a set of coefficients as $C_{Dn} = 2.4$, $C_{Dt} = 0.8$, $C_{Mn} = 3.1$, $C_{Mt} = 1.7$. Burmester et al. [50] found that using $C_{Dn} = 1.5$ instead of 2.4 improves the prediction of surge motion in surge decay simulations. In order to determine the coefficients of the mooring lines for the following pitch decay and waves tests, a sensitivity study is performed.

The MOORING3D module is running at stand-alone mode with a baseline mooring setup with coefficients $C_{Dn} = 1.5$, $C_{Dt} = 0.8$, $C_{Mn} = 3.1$, $C_{Mt} = 1.7$. The experimental measurement of 6 DOF motion histories of the floater under pitch free decay and regular waves are given to the code for determination of fairlead positions for three mooring lines. Thereafter the tensions at the fairlead of each mooring line are computed.

The baseline setup is first cross-verified with OrcaFlex and compared with the experiment measurements for pitch decay test. The results are shown in Figure 4.2. It should be noted that the mooring tension in SBA and PSA mooring lines are not anti-symmetric. This is due to the asymmetric floater motion in the sway direction existed in the experiment. Furthermore, the high frequency fluctuated patterns are presented in the figure, which is caused by the high frequency fluctuation in the input motion history. The mooring simulation results from MOORING3D and OrcaFlex are almost identical and their agreements with experimental results are generally good in SBA and PSA mooring lines. They are poorly matched with the experimental results in BOW mooring line, especially in the first few pitch troughs. The deviations are most possibly caused by

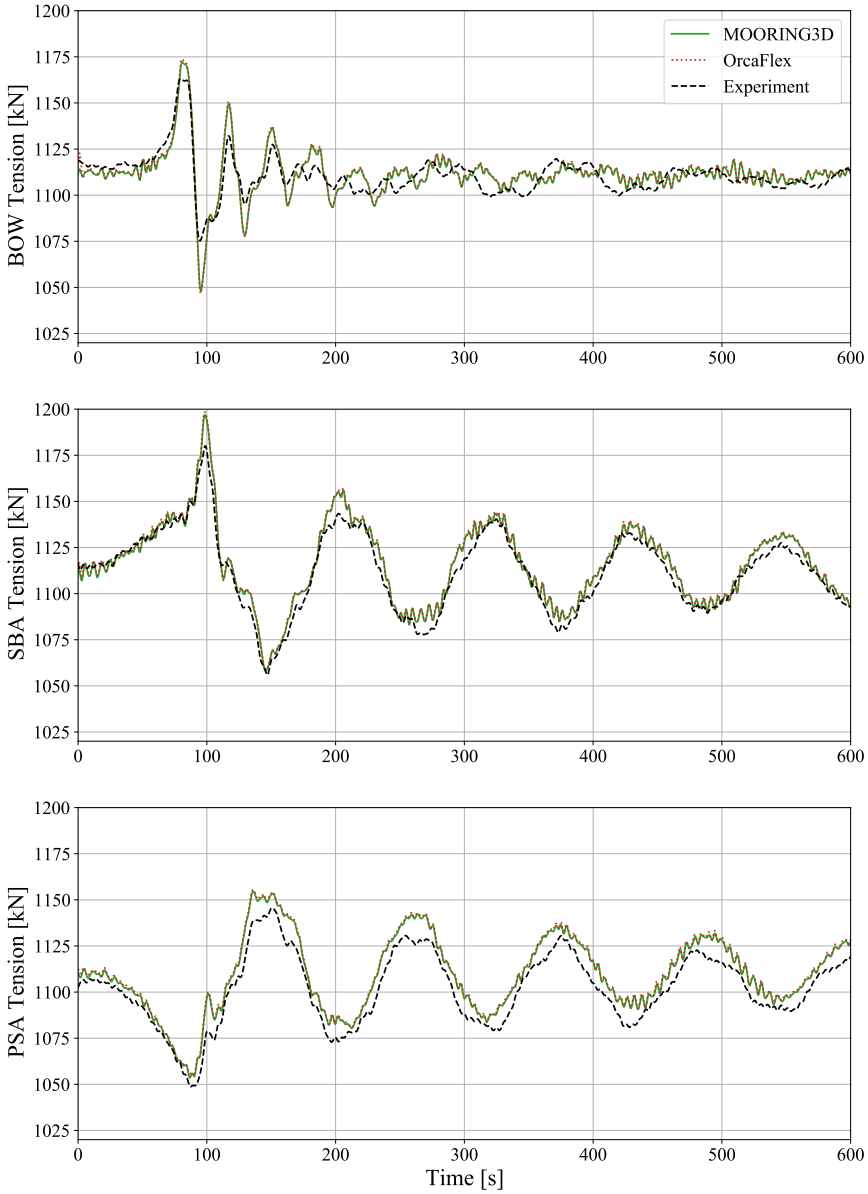

Figure 4.2: Cross verification using pitch free decay test data of MOORING3D and OrcaFlex with the baseline coefficient setup, i.e. $C_{Dn} = 2.4$, $C_{Dt} = 0.8$, $C_{Mn} = 3.1$, $C_{Mt} = 1.7$. The experimental measurements is also added for comparison.

the wake induced forces from the wake of floater motion. Both numerical tools lack the instantaneous flow field information passed by the flow solver to capture wake induced forces. However, the largest difference of BOW tension at the first pitch trough is as small as 3%, and the contribution of mooring forces to the motion solver is less than 10% of the hydrodynamic forces in the

coupled simulation. Therefore, the ignorance of wake induced forces is not critical in the present work.

After the cross-verification, the simulation was repeated with varied drag or added mass coefficients, changing only one value each time. The comparison of the BOW mooring tension between numerical and experimental results are depicted in Figure 4.3. The mooring tension is only sensitive to the normal drag coefficient C_{Dn}. With a value of $C_{Dn} = 1.5$, the solutions from MOORING3D has a closest match with the experiment, especially at the first oscillation of pitch decay at around 80 - 150 s.

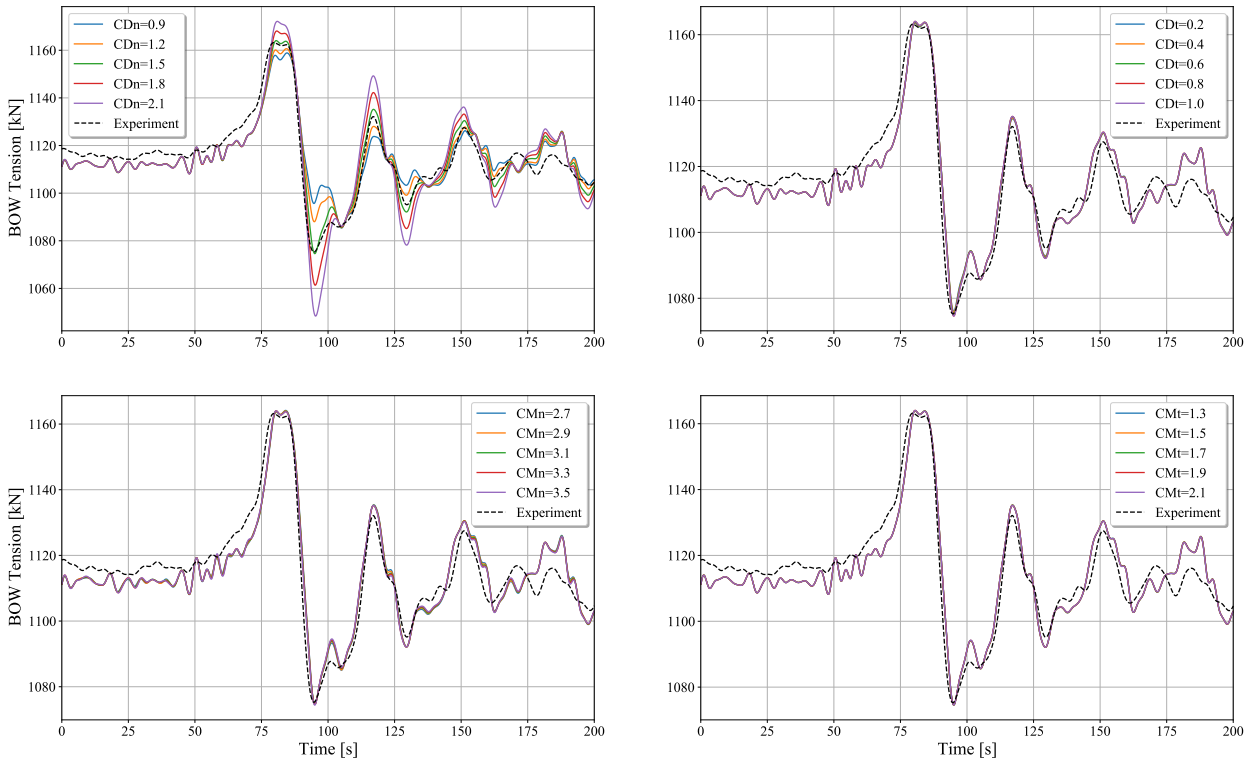

Figure 4.3: Sensitivity test of drag and added mass coefficients for mooring lines using pitch free decay test data. Except for the coefficients labeled in legends, all tests are simulated with the baseline coefficients setup $C_{Dn} = 1.5$, $C_{Dt} = 0.8$, $C_{Mn} = 3.1$, $C_{Mt} = 1.7$.

As for wave cases, sensitivity study is also conducted by the same means. The power spectral density of tensions of three mooring lines are computed from numerical results. The comparison

error of them against experiment are presented in Figure 4.4. The normal drag coefficient C_{Dn} is again the most significant impact factor and the value of $C_{Dn} = 1.5$ best fits with the experimental data.

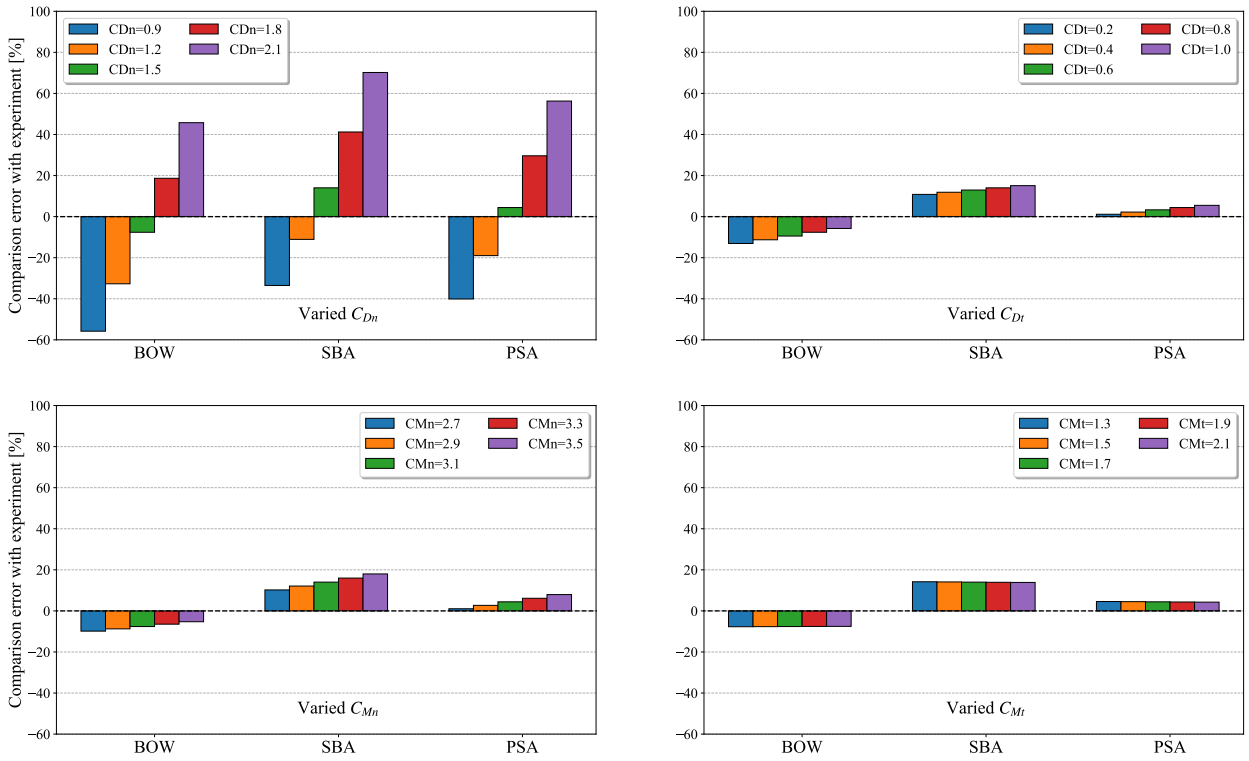

Figure 4.4: Sensitivity test of drag and added mass coefficients for mooring lines. Comparison errors of PSDs of the mooring tensions in all three mooring lines against experimental results are depicted with different set of coefficients. Except for the varied coefficient captioned under each plot, the remaining coefficients are set as $C_{Dn} = 1.5$, $C_{Dt} = 0.8$, $C_{Mn} = 3.1$, $C_{Mt} = 1.7$.

Therefore, the selection of coefficients is settled at $C_{Dn} = 1.5$, $C_{Dt} = 0.8$, $C_{Mn} = 3.1$, $C_{Mt} = 1.7$. A concluded property of the mooring system is summarized in Table 4.1.

4.3 Discretization uncertainty in MOORING3D

Numerical uncertainties raised in MOORING3D need to be quantified and add into numerical uncertainty for coupled simulations. The iterative uncertainty of MOORING3D is neglected due to the low convergence tolerance of 10^{-6} and the fact that all solutions have converged below the

Table 4.1: Properties of the mooring lines attached to the OC5 floater. Subscript m denotes the mooring lines.

Designation	**Symbol**	**Value**	**Unit**
Mass per unit length	M_m	0.05024	kg/m
Diameter	D_m	0.00277372	m
Unstretched length	L_m	16.71	m
Submerged weight per unit length	W_m	0.43192	N/m
Buoyancy per unit length	B_m	0.06076	N/m
Stiffness	EA	5989.0666	N
Normal drag coefficient	C_{Dn}	1.5	-
Tangential drag coefficient	C_{Dt}	0.8	-
Normal added mass coefficient	C_{Mn}	3.1	-
Tangential added mass coefficient	C_{Mt}	1.7	-

tolerance. The statistical uncertainty is also omitted in MOORING3D for that no statistical method is used in deriving the mooring forces. Therefore, the discretization uncertainty is the only one to be quantified for MOORING3D computations.

Both spatial and temporal verification study are made to estimate the discretization uncertainties brought by MOORING3D. The simulations are performed with similar setup to the coefficient sensitivity study using pitch free decay test data in the previous section. For spatial discretization uncertainty analysis, five different grids with 10, 30, 50, 100 and 200 elements per mooring line are investigated. For temporal discretization uncertainty analysis, three different time step sizes with $\Delta t = 0.07070$ s, $\Delta t = 0.03535$ s and $\Delta t = 0.02357$ s are used. The baseline setup for all settings is grid with 100 elements per line and time step size of $\Delta t = 0.07070$ s. The mooring tensions for three mooring lines are plotted at Figure 4.5 for spatial discretization uncertainty analysis and Figure 4.6 for temporal one. Among three mooring lines, the mooring tensions computed from five grids are nearly identical with a maximum difference at 0.009%. The discrepancies in mooring tensions between different time step sizes are even smaller. The total discretization uncertainty is $U_{d,Moor} = 0.01\%$ for the baseline grid. The total numerical uncertainty add-up by MOORING3D is only $U_{N,Moor} = 0.01\%$ and hence is neglected in the total numerical uncertainty of coupled

simulations.

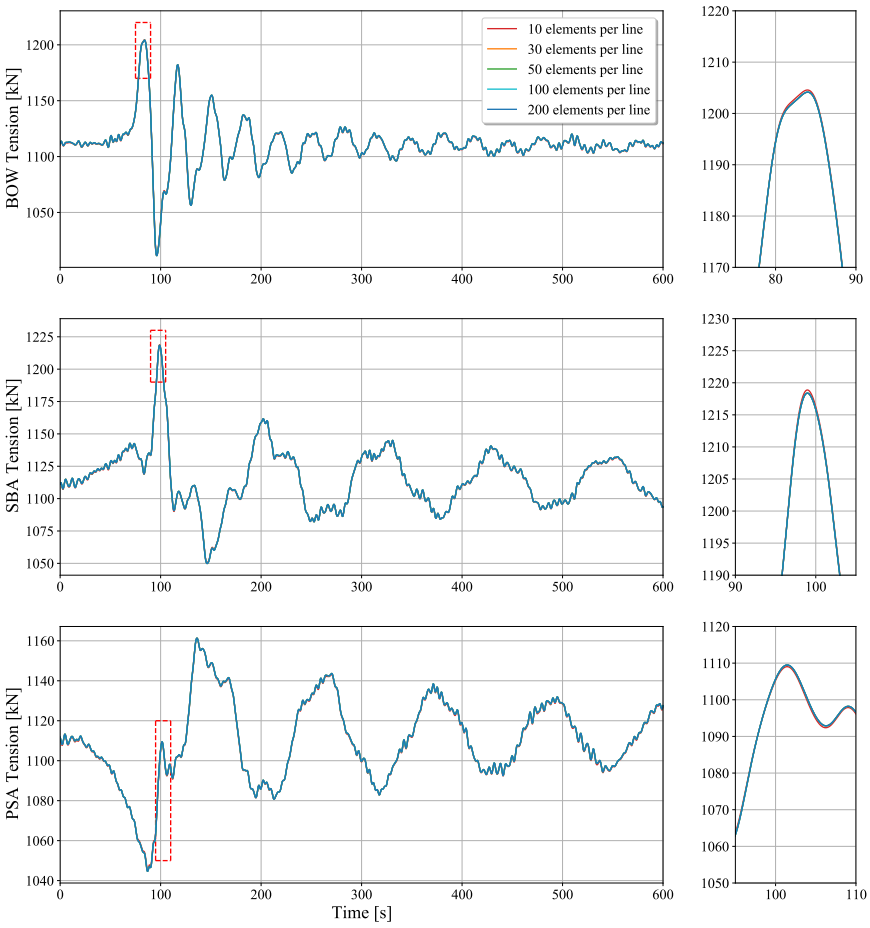

Figure 4.5: The mooring tensions at fairlead of each mooring line in pitch decay test computed by MOORING3D with five different grids.

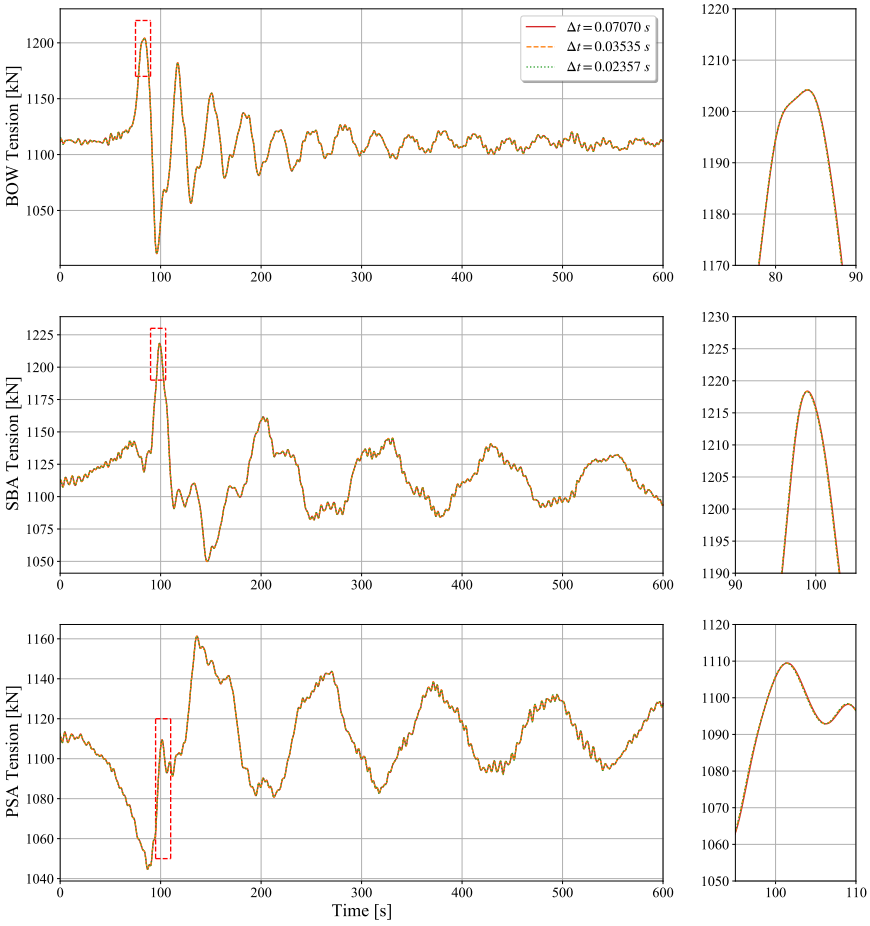

Figure 4.6: The mooring tensions at fairlead of each mooring line in pitch decay test computed by MOORING3D with three different time step sizes.

5. V&V STUDY OF FOWT SEMI-SUBMERSIBLE PLATFORM UNDER PITCH FREE DECAY*

5.1 Numerical settings

For a simulation of pitch free decay motion of a semi-submersible floater, the motions in sway, yaw and roll DOFs are negligible. Furthermore, the floater is symmetric with respect to xOz plane. Therefore, solely half of the geometry is modeled with xOz plane as the cutting plane. The computational domain is constructed with a semi-cylinder wrapping the half floater geometry. Noted that the sharp corners of the columns were skirted to match the real physical model. It is advocated to perform this treatment to better capture the local flow pattern in numerical simulations, especially in the cases where rotational motions are dominant [51]. The origin of the domain is coincided with the center of gravity (COG) of the floater. The radius of the cylindrical domain is set as $r = 4.9$ m which is 6 times of the characteristic radius of the floater $r_c = 0.82$ m. The total height is set as $h = 8.0$ m consisting of the water domain with depth of $d = 4.0$ m and the air domain with height of $h_a = 4.0$ m. The computational domain is illustrated in Figure 5.1.

Pure hexahedral unstructured grids are generated in the computational domain. The grids are refined at three sectors illustrated in Figure 5.1. The specifications of the refinement zones are listed in Table 5.1. Additionally the grid is refined towards the free surface plane $z = 0.1614$ m with a refinement ratio same as Sector 2. Refinement ratio is higher at the connections between columns, pontoons and braces to ensure that the geometry is correctly captured. Viscous layers are inserted at the near wall regions of the floater with the non-dimensional wall distance value $y^+ < 1.5$. A detail view of the grid is illustrated in Figure 5.2. Four grids with different grid sizes are generated for the purpose of verification study. The corresponding relative grid size (with the finest grid denoted as 1), number of cells and maximum equiangular skewness angle of each grid are summarized in Table 5.2. Amongst which G3 is selected as the baseline grid. The cell aspect

*Reprinted with permission from "Verification and validation of CFD simulations for semi-submersible floating offshore wind turbine under pitch free-decay motion" by Y. Wang, H.-C. Chen, A. Koop, and G. Vaz, 2021. Ocean Engineering, vol. 242, p. 109993, Copyright 2021 by Elsevier.

ratios of all grids are maintained below 2 for all cells except for boundary layers. The orthogonality of all cells outside boundary layers is larger than 60 deg with 85% of cells larger than 80 deg. The maximum skewness in all grids are obtained around the corners of the base columns and does not exceed 0.9. The grid quality for all grids could be judged as good.

Table 5.1: Refinement zones settings with grid sizes measured with baseline grid. The unit is meter for all values.

Zone	**Origin**	**Height**	**Radius**	$\Delta z(=\Delta x=\Delta y)$
Sector 1	(0,0,-2.5)	3.5	4.9	0.07
Sector 2	(0,0,-0.1886)	0.7	1.0	0.02
Sector 3	(0,0,0.1264)	0.07	1.6	0.01

Table 5.2: Relative grid size, number of cells and maximum skewness of all grids for the verification study. Refinement factors are computed by Eq. (2.52). (* The coarsest grid cannot converge with the finest time step size T5 because of the poor resolution at outer boundary. Hence a grid with refinement at outer boundary is generated specially for case G1T5.)

Acronyms	**Relative grid size** h_i	**Number of cells** N_{cell_i} [million]	**Max skewness**
G1	1.740	1.564	0.860
G1*	1.527	2.313	0.834
G2	1.384	3.105	0.842
G3	1.211	4.636	0.899
G4	1.000	8.237	0.794

A no-slip condition is assigned to the boundaries of the semi-submersible. A static pressure boundary condition is prescribed at the top and bottom of the domain. On the xOz planar surface, symmetry boundary condition is applied. The curved surface of the semi-cylinder is modeled as

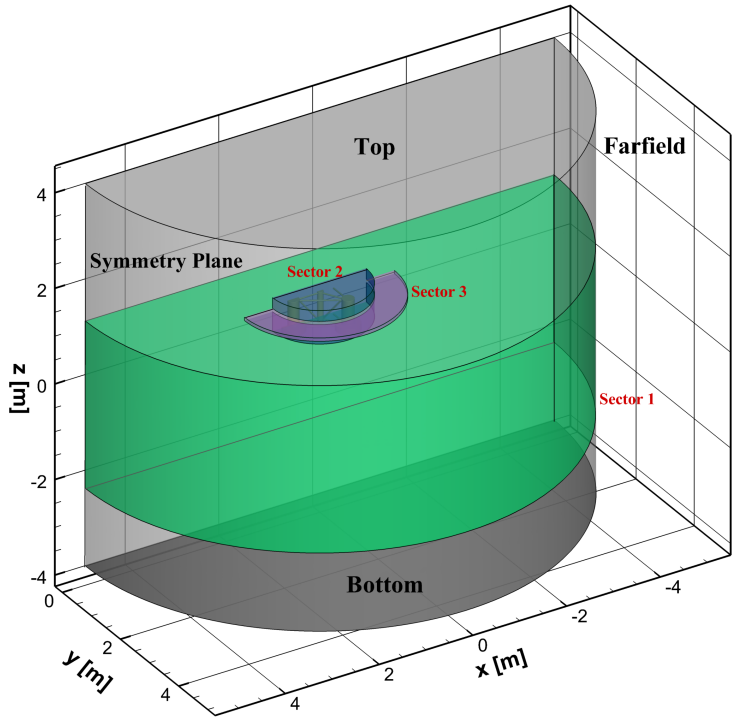

Figure 5.1: Computational domain setup in all simulations. With refinement sectors defined in Table 5.1.

non-reflecting boundary condition of first-order Sommerfeld type [52]. This condition approximately achieves no wave reflection from the boundary surface through Equation 5.1 applied at the boundary:

$$\frac{\partial \hat{\phi}}{\partial t} + c\left(\cos\alpha \frac{\partial \hat{\phi}}{\partial x} + \sin\alpha \frac{\partial \hat{\phi}}{\partial y}\right) = 0, \tag{5.1}$$

where the velocity potential of outgoing waves is denoted as $\hat{\phi}$, the incident angle is denoted as α, and the phase velocity is denoted as c. The phase velocity in the boundary condition is set larger than the mean normal flow velocity to ensure the non-reflection condition.

A deforming-grid method is used to enable simulations of the pitch motion of the platform in the fixed computational domain. Such method is implemented with radial basis function interpolation to derive the displacements of the internal mesh nodes for a specified displacement of the

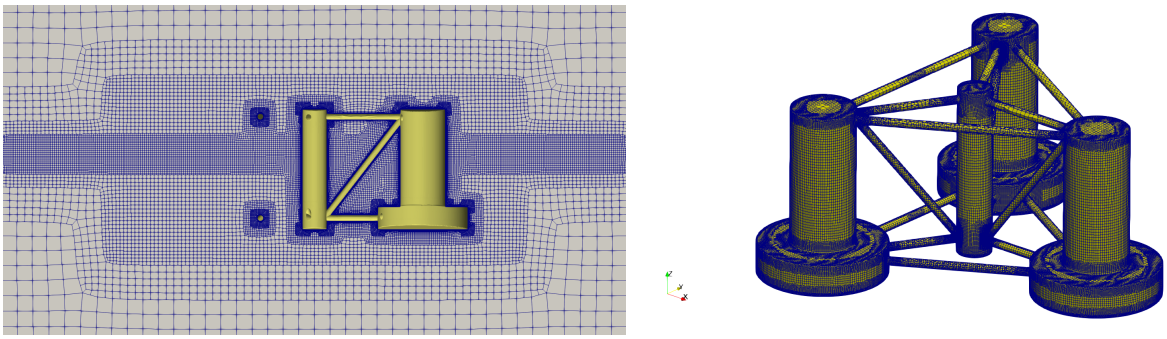

Figure 5.2: Grid refinement at semi-submersible platform and free surface.

platform [53]. Support radius in radial basis function setup is chosen as 1.6 m which is twice of the platform outer radius. Solver settings and choices of discretization schemes for each transport equation are listed in Table 5.3. Implicit three time level scheme is utilized for time discretization. Linear equation solvers from PETSc library are used in simulations [54].

Table 5.3: Numerical settings to solve the governing equations and the convergence tolerance or maximum iterations in pitch free decay case.

Equation	**Preconditioner**	**Solver**	**Convec. Scheme**	**Converg. tol. (Max iter.)**
Momentum	JACOBI	GMRES	QUICK	1×10^{-2} (200)
Pressure	BJACOBI	CG	-	5×10^{-2} (500)
Free Surface	BJACOBI	GMRES	ReFRICS	5×10^{-2} (300)
Turbulence	BJACOBI	GMRES	1st Order UPWIND	1×10^{-2} (300)

Five sets of time step sizes are applied to each grid such that 20 simulations are done for the verification study. The time step sizes range from $\Delta t = 3 \times 10^{-4}$ s to $\Delta t = 2.4 \times 10^{-3}$ s which are approximately $T_{nP}/16000$ to $T_{nP}/2000$ where T_{nP} is the natural pitch period measured from experiment. Detailed time step settings and refinement factors are listed in Table 5.4. The baseline simulation is accompanied with G3 grid and T4 time step size (G3T4).

Table 5.4: Time step size and relative time step for the verification study.

Acronyms	**Relative time step**, t_j	Δt_j **(s)**	**Ratio of** T_{nP}
T1	8.00	0.0024	$T_{nP}/2000$
T2	4.00	0.0012	$T_{nP}/4000$
T3	2.67	0.0008	$T_{nP}/6000$
T4	2.00	0.0006	$T_{nP}/8000$
T5	1.00	0.0003	$T_{nP}/16000$

5.2 Verification study

An investigation into the iterative convergence of the baseline simulation shows that the residuals are below 10^{-4} level. According to the judgement that iterative uncertainty is negligible when controlled within two order of magnitude below the discretization uncertainty, and knowing that the discretization uncertainty is at a level of 10^{-2} to 10^{-1}, the iterative uncertainty is neglected in the quantification of numerical uncertainty of pitch free decay simulations. Moreover, the quantification of the statistical uncertainty is unable to perform for the pitch free decay cases. Therefore, the numerical uncertainty is purely contributed by discretization uncertainty.

20 combinations of grid and time step size are applied to the pitch free decay simulations for quantification of discretization uncertainty. The simulations are run on Terra cluster within Texas A&M University using 240 Intel Xeon E5-2680 2.4 GHz cores. The wall time for the simulations are summarized in Table 5.5.

Table 5.5: Grid and time step size combinations of 20 simulations for the discretization uncertainty analysis for pitch free decay case. The wall times in unit of hour are actual computing times using 240 cores on TAMU Terra cluster.

	T1	**T2**	**T3**	**T4**	**T5**
G1	18.6	28.4	35.7	45.5	60.4
G2	28.9	75.6	108.3	126.4	151.0
G3	52.7	116.0	157.1	181.9	226.8
G4	89.7	148.2	224.2	286.1	321.2

Pitch free decay motion histories obtained from 20 simulations are plotted in Figure 5.3. Markers are added to the peaks of each pitch oscillation cycle. From Figure 5.3 it can be observed that the pitch motions for all 20 simulations are close to each other. An enlarged view of the pitch motions at the first negative peak is shown on the right of Figure 5.3. In view of the first negative peaks, the time when peaks are reached from all simulations were nearly identical at around 2.24 s. The peak amplitudes vary among the simulations and showed an increasing trend when the grid size decreases. The largest difference (between G1T3 and G4T5) is around 0.06 degree which is 1.6% of the mean pitch amplitude at the first negative peak.

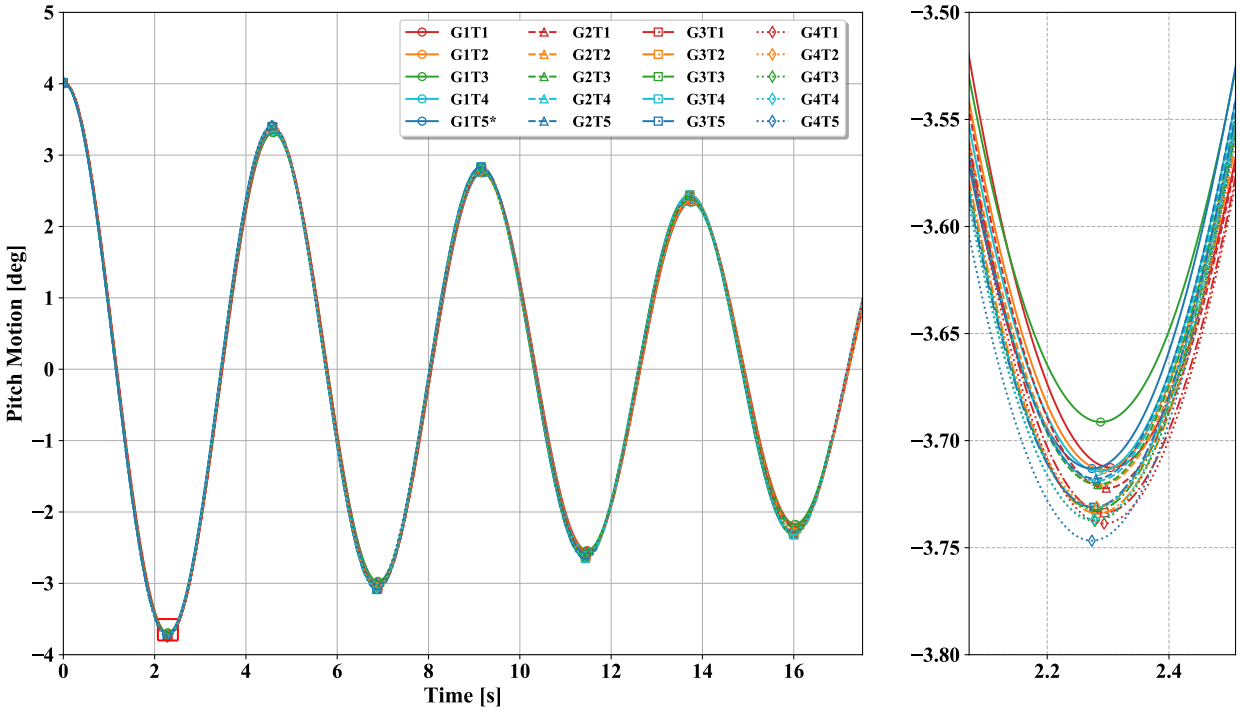

Figure 5.3: Pitch free decay motions of the floater using 20 different sets of grid sizes and time step sizes.

It was advocated by [16] to use quantities that needs the least amount of post-processing for discretization error estimation to avoid uncertainties brought in from post-processing. In the present work, the pitch motions at certain time instances distributed over 4 oscillation cycles are selected

Table 5.6: Numerical uncertainty analysis of the pitch natural period with G3T4 evaluated from 20 cases.

	Extrapolated value ϕ_0	**G3T4 solution** ϕ_1	**Discretization uncertainty** U_d	**Numerical uncertainty** U_N
T_{nP}	4.473	4.480	0.050 (1.1%)	1.1%

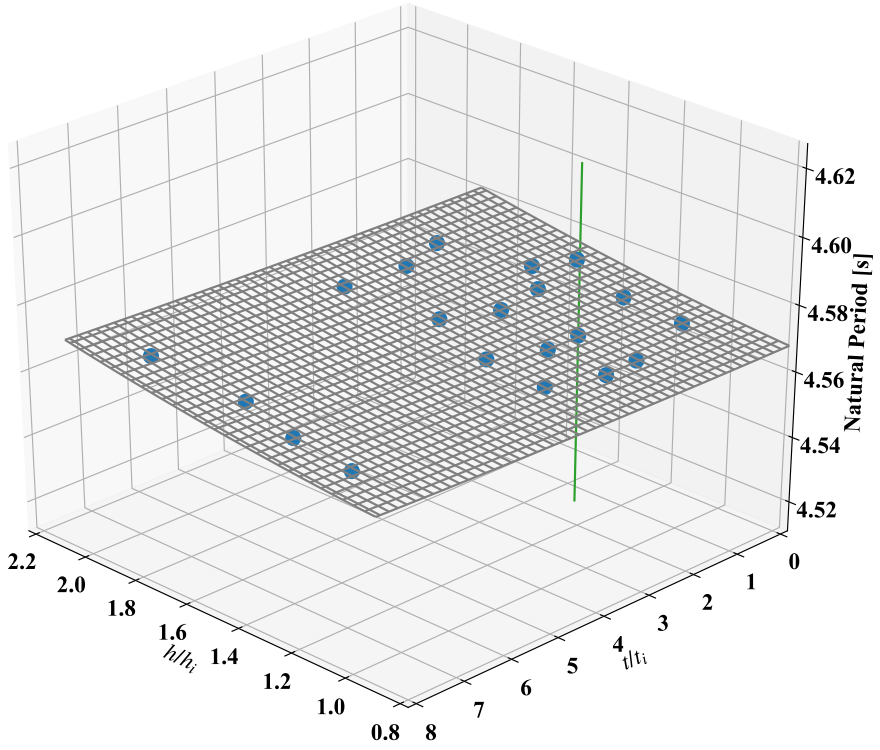

Figure 5.4: 3D fit of pitch natural periods gathered from 20 cases. Green bar indicates the uncertainty range of natural period for G3T4.

for quantification of discretization uncertainties. The discretization uncertainty of the pitch natural period was checked at first to ensure that the same time stamp in different cases are representing almost the same oscillating phase. The results are shown in Table 5.6 and Figure 5.4. The discretization uncertainty is estimated as 1.1% in pitch natural period with baseline simulation G3T4.

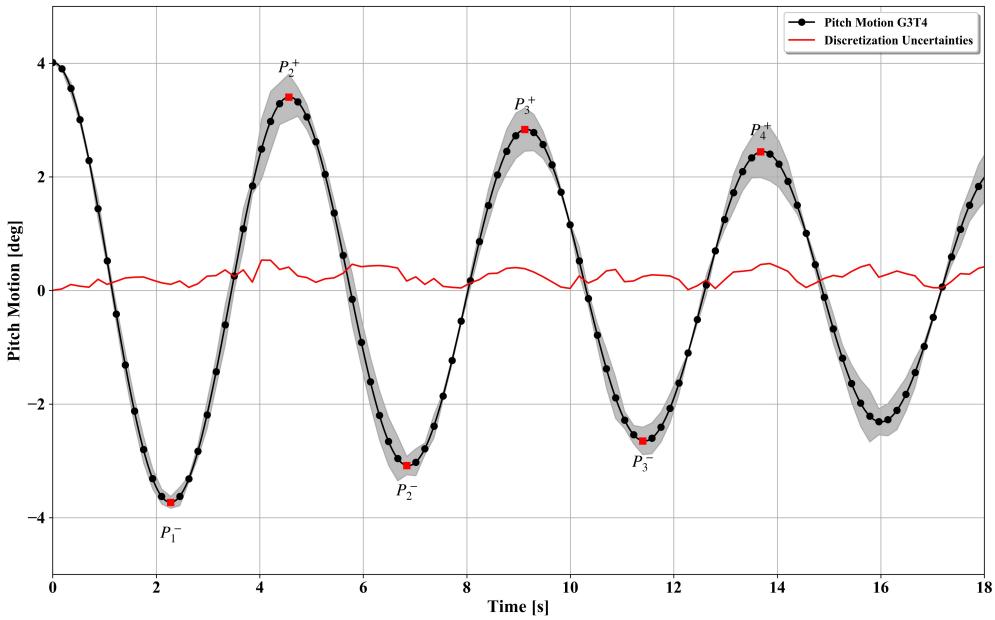

Figure 5.5: Discretization uncertainty analysis of pitch motion over 4 oscillation periods. Gray area is the range of motion based on the quantified uncertainty level.

With the low uncertainties in temporal scale, the pitch motions at the same time instance from all cases can be used in the quantification of the discretization uncertainties.

In Figure 5.5, the discretization uncertainty is illustrated as the gray area around the pitch motion history. The red solid line represents the absolute discretization uncertainty which is half of the uncertainty range. Inspecting the figure, the discretization uncertainty is at a low level in the first oscillating period and then grows in time. The uncertainty is higher around the peaks of pitch motion. The absolute discretization uncertainty in pitch motion is smooth along the whole simulation with a maximum of 0.531 deg and an average value at 0.236 deg. The averaged discretization uncertainty percentage from all selected time instances is 15.78%.

Further investigation is made with the six peaks in the first three cycles which are marked with red square markers in Figure 5.5. The numerical uncertainty results for these peaks are shown in Figure 5.6 and summarized in Table 5.7. Uncertainty percentages obtained in these peaks ranged from 2.8% to 18.6 %. The estimated uncertainties are smaller when evaluating the negative peaks.

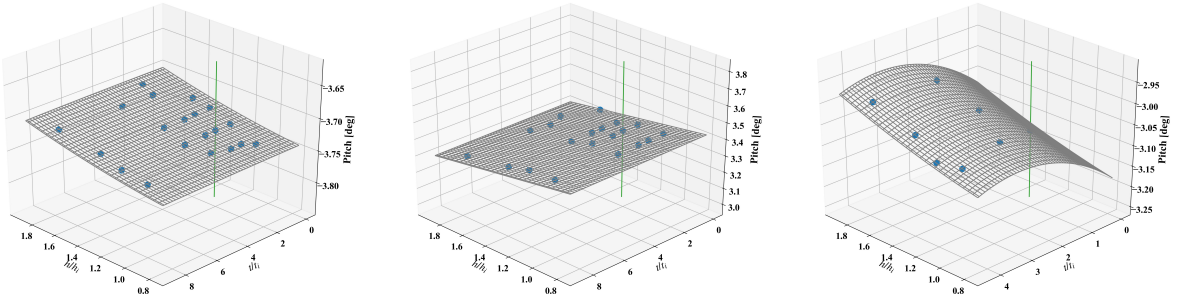

(a) P_1^- at $t = 2.2803$ s. (b) P_2^+ at $t = 4.5607$ s. (c) P_2^- at $t = 6.8401$ s.

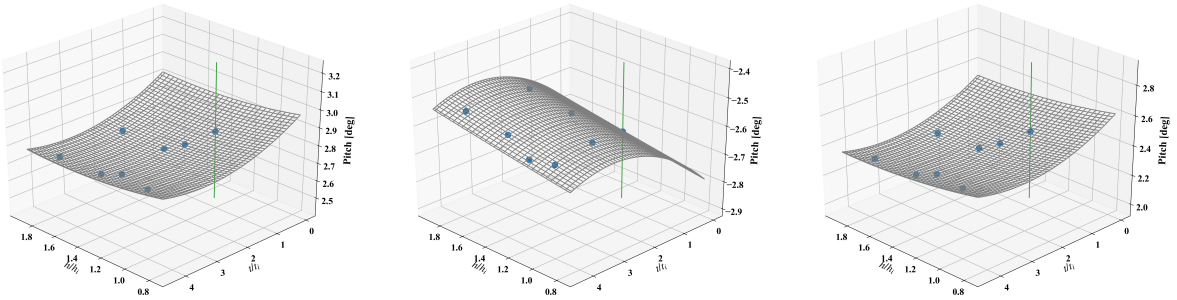

(d) P_3^+ at $t = 9.1204$ s. (e) P_3^- at $t = 11.4008$ s. (f) P_4^+ at $t = 13.6802$ s.

Figure 5.6: 3D fit of pitch peaks with green bar representing uncertainty estimation for G3T4. Uncertainties for first two peaks were evaluated from all 20 cases while others from 8 cases with sufficient simulation time.

Table 5.7: Uncertainty analysis of six pitch peaks with G3T4.

	Extrapolated value	**G3T4 solution**	**Discr. uncertainty**
	ϕ_0	ϕ_1	U_d
P_1^-	-3.75	-3.73	0.104 (2.8%)
P_2^+	3.51	3.40	0.408 (12.0%)
P_2^-	-3.21	-3.08	0.163 (5.3%)
P_3^+	3.14	2.83	0.382 (13.5%)
P_3^-	-2.84	-2.65	0.241 (9.1%)
P_4^+	2.80	2.44	0.454 (18.6%)

5.3 Validation study

The settings of G3T4 are adopted in the simulation for the validation study. The total simulation time is 25 s which includes 5 oscillating cycles of pitch decay motion. The time window is chosen such that the average numerical uncertainty does not exceed the uncertainty of the amplitude in the fifth oscillation. In Figure 5.7, the surge, heave and pitch motions are presented during the pitch decay, comparing the experimental results with the results using the linear mooring (LM) and the dynamic mooring (DM) model.

Inspecting the surge motion, the experimental results shows a drift in opposite of surge direction. Numerical results are fluctuating around zero with a bichromatic pattern where dynamic mooring model has lower amplitude as a result of the drag forces on the mooring lines in surge direction. According to NREL report [1], a large cable bundle was hanging off the tower in the model test and could create additional stiffness and preload for the system. They recommended additional stiffness in surge direction to get closer to the experimental value. However, the exact value is not published and hence in this study no additional surge stiffness is applied.

Heave motion is known to be strongly coupled with pitch motion in the pitch free decay test. The numerical results agree with the experimental heave motion in trend but are larger in amplitudes where the results using the linear mooring have slightly larger heave amplitudes than the results using the dynamic mooring model.

In the pitch motion plot, numerical results using linear mooring model have a shorter natural period and larger pitch amplitudes than the results from dynamic mooring model, whereas the latter show a good agreement with experimental results. Taking the uncertainties into account, the difference between dynamic mooring and experimental results are almost within the range of averaged uncertainty except for the negative pitch peaks, and all fall in the range of maximum uncertainty.

Applying the PQ analysis to the pitch motion histories as shown in Figure 5.8, the derived damping coefficients are listed with natural periods in Table 5.8 & 5.9. From Table 5.8, one can find that utilization of dynamic mooring model significantly improves the prediction of pitch natural

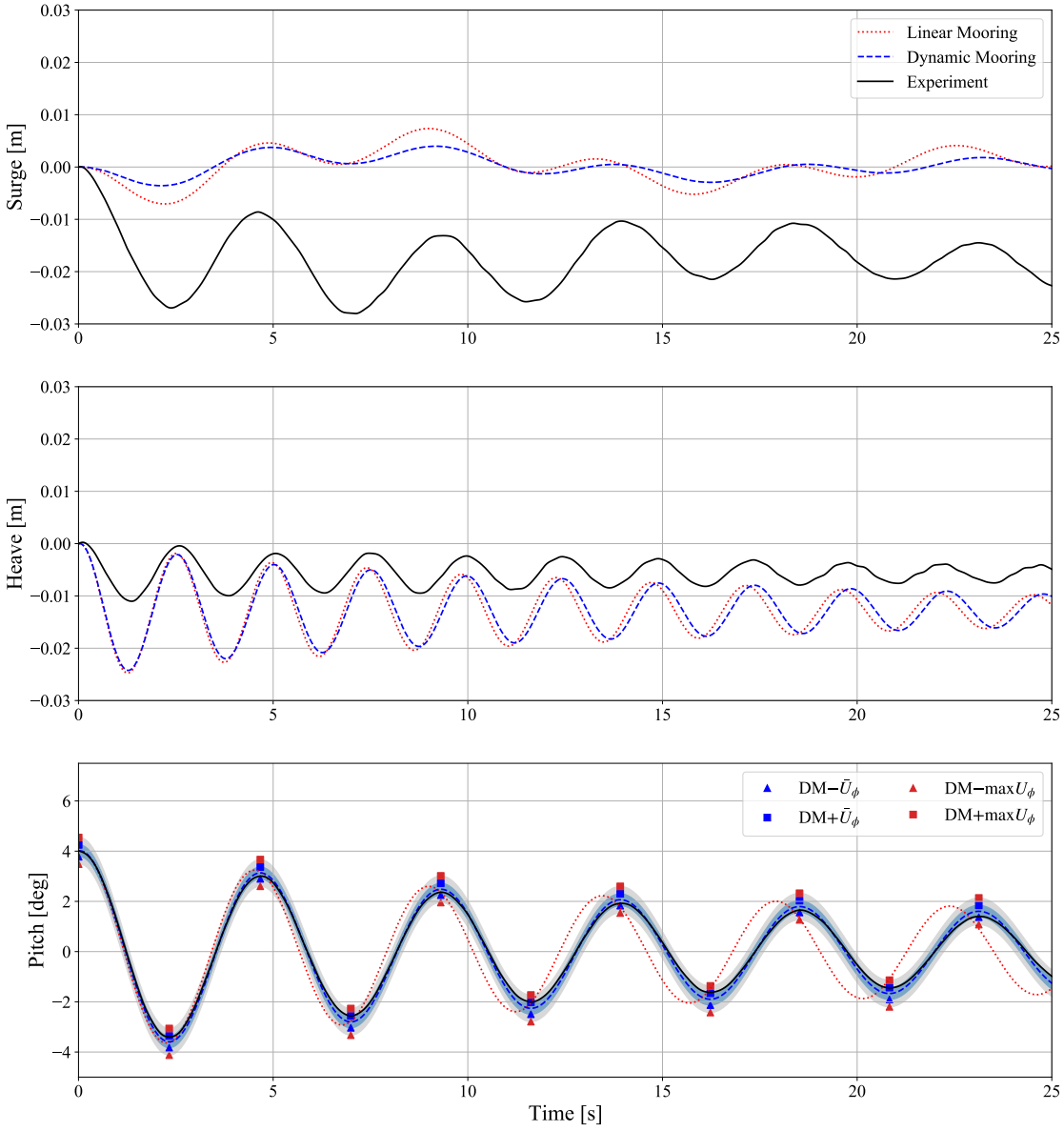

Figure 5.7: Surge, heave and pitch motion histories comparison between CFD simulations with linear mooring model, dynamic mooring model and experiment. Blue and gray bands represent the uncertainty ranges estimated by averaged and maximum value, respectively.

period to obtain a 0.04% comparison error with the experimental measurement where comparison error with linear mooring is 3.3%. Validation has been achieved within the validation uncertainty level 1.1% for DM simulation.

The improvements are also observed in linear and quadratic damping coefficients. For the

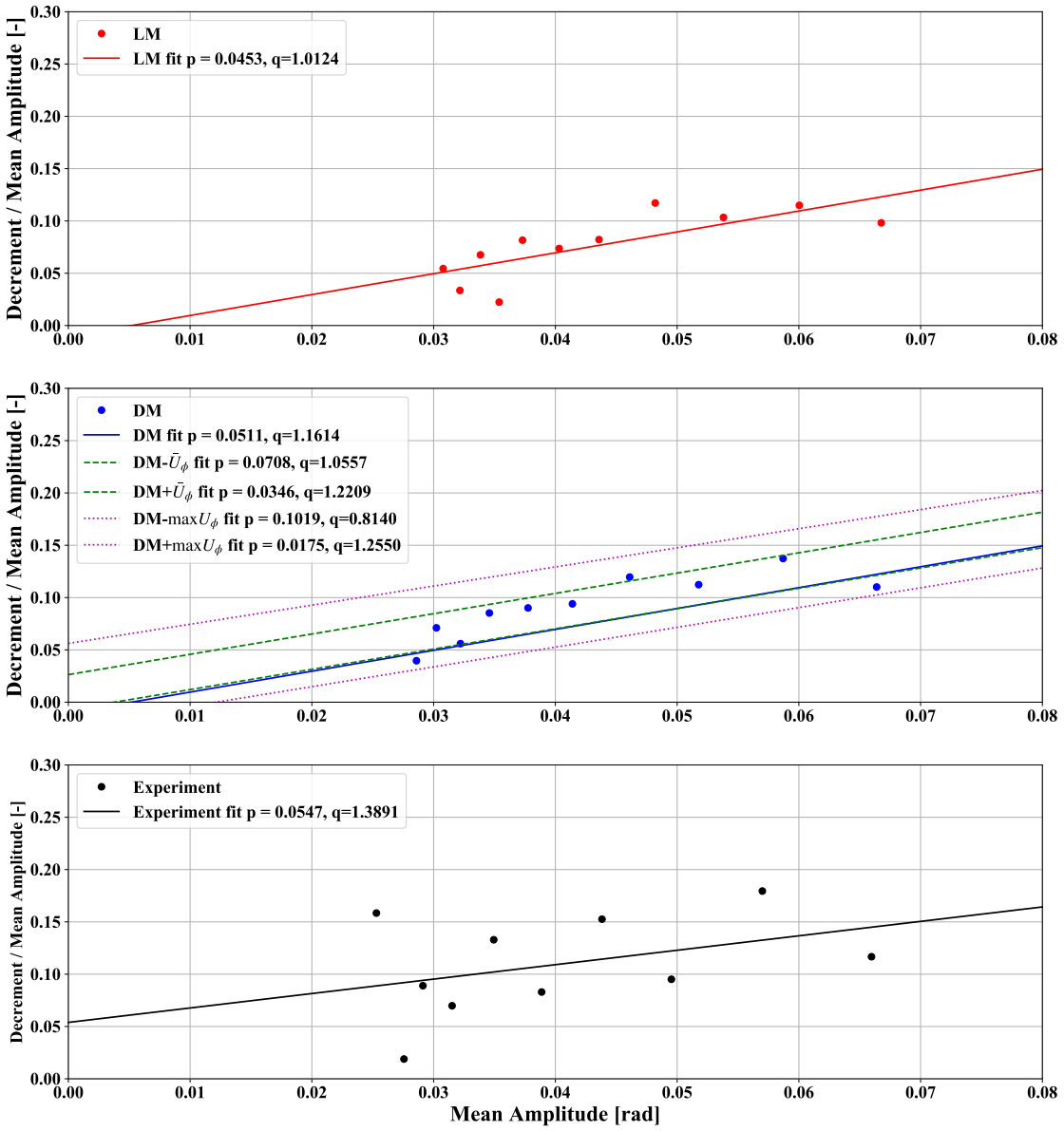

Figure 5.8: PQ analysis to the pitch motion for numerical solutions with LM (linear mooring model), DM (dynamic mooring model) and experimental results.

solutions with DM, the linear damping is 6.59% smaller and quadratic damping is 16.39% smaller than the values from the experimental results, whereas for the solutions with LM, the linear and quadratic damping are 17.24% and 27.12% smaller respectively. Further validation is studied for the solutions with DM. The comparison error and validation uncertainty are listed in Table 5.10. Applying the mean numerical uncertainty to the DM solutions, the validation uncertainty

Table 5.8: Pitch natural periods from numerical solutions and experiment.

	Pitch natural period	**Comparison error**	**Validation uncertainty**
	T_{nP} [s]	E	U_V
LM	4.480	3.3%	1.1%
DM	4.636	0.04%	1.1%
Exp.	4.634	-	-

Table 5.9: Pitch damping coefficients generated from PQ analysis for numerical solutions in comparison with experiment. Critical damping is denoted as b_C. $\bar{U}_\phi$ is the mean value of numerical uncertainty. The damping coefficients for uncertainty bounds are computed using the marked extremes in the pitch decay motion (Figure 5.7).

	Linear damping coeff. & % of b_C	**Quadratic damping coeff. & % of** b_C
	p, B_L	q, B_Q
LM	0.0453, 0.72%	1.0124, 13.53%
DM$-\max(U_\phi)$	0.1019, 1.62%	0.8140, 11.26%
DM$-\bar{U}_\phi$	0.0708, 1.13%	1.0557, 14.60%
DM	0.0511, 0.81%	1.1614, 16.07%
DM$+\bar{U}_\phi$	0.0346, 0.55%	1.2209, 16.89%
DM$+\max(U_\phi)$	0.0175, 0.28%	1.2550, 17.36%
Exp.	0.0547, 0.87%	1.3891, 19.21%

Table 5.10: Validation study for linear and quadratic damping coefficients obtained from the solutions with DM. The subscript ub and lb denote upper bound and lower bound of the uncertainty range. The validation uncertainty obtained by applying the mean uncertainty towards the solutions (DM$\pm\bar{U}_\phi$) is denoted with subscript $mean$ and DM$\pm\max(U_\phi)$ is denoted with subscript max.

	E	$U_{Vlb,mean}$	$U_{Vub,mean}$	$U_{Vlb,max}$	$U_{Vub,max}$
p	+6.58%	−32.29%	+38.55%	−65.75%	+99.41%
q	+16.39%	−9.10%	+5.12%	−29.91%	+8.06%

range for the linear damping coefficient p is from -32.29% to +38.55%, whereas the validation uncertainty range obtained with solutions applying the maximum numerical uncertainty is from

-65.75% to +99.41%. The comparison error 6.58% is well covered in both ranges and thus the validation is achieved for the linear damping coefficient p. For the quadratic damping coefficient q, the validation uncertainty ranges from both solutions are narrower with -9.10% to +5.12% and -29.91% to +8.06%. However, the comparison error does not fall in neither of the uncertainty ranges which indicates that validation is not achieved for the quadratic damping coefficient q.

Through the above validation study, CFD simulation of pitch free decay of OC5 DeepCwind semi-submersible platform with dynamic mooring model is capable to accurately predict the natural period. Prediction of the linear damping coefficient is close to experimental measurement within the uncertainty range. Yet it fails to predict the quadratic damping coefficient.

Burmester et al. [16] listed five inadequacies in simulations of surge decay motion, which are the lack of dynamic mooring model, omitted influence from rotor and attached cables, the shortness in modeled degree of freedoms, the neglect of turbulence effect especially when applying the symmetric cut, and finally, the missing of uncertainty analysis of experiment.

In this study, dynamic mooring effect is well considered and degree of freedoms that strongly coupled with pitch motions, i.e. surge and heave are included. Damping influences from rotor aerodynamics and attached cables are expected to be higher in pitch motion and could be the primary cause of the under-prediction of both linear and quadratic damping.

Turbulence effect around cylindrical structures such as the columns of the floater is believed to increase the quadratic damping. The application of symmetry plane boundary condition in the xOz-plane would suppress the turbulence effects around the front and center columns and hence reduce the prediction in quadratic damping.

Last but not the least, missing uncertainties of the experimental data made it difficult to perform a rigorous validation on the quantities reported. It would also affect the credibility of the model test data. Within the OC6 consortium a follow-up model test campaign was carried out to assess some of these uncertainties [46].

6. V&V STUDY OF FOWT SEMI-SUBMERSIBLE PLATFORM UNDER REGULAR WAVES

6.1 Numerical settings

The numerical wave tank for regular waves simulations is designed with a length of $L = 26$ m, width of $W = 5$ m and a total height of $h = 5.6$ m consisting of the water domain with depth of $d = 4.0$ m and the air domain with height of $h_a = 1.6$ m. The floater is placed at the location where its center of gravity (COG) coincides with the origin of the computational domain. The centerline is 10 m downstream the inflow boundary and 16 m upstream from the outflow boundary. The computational domain and the boundary settings are illustrated in Figure 6.1.

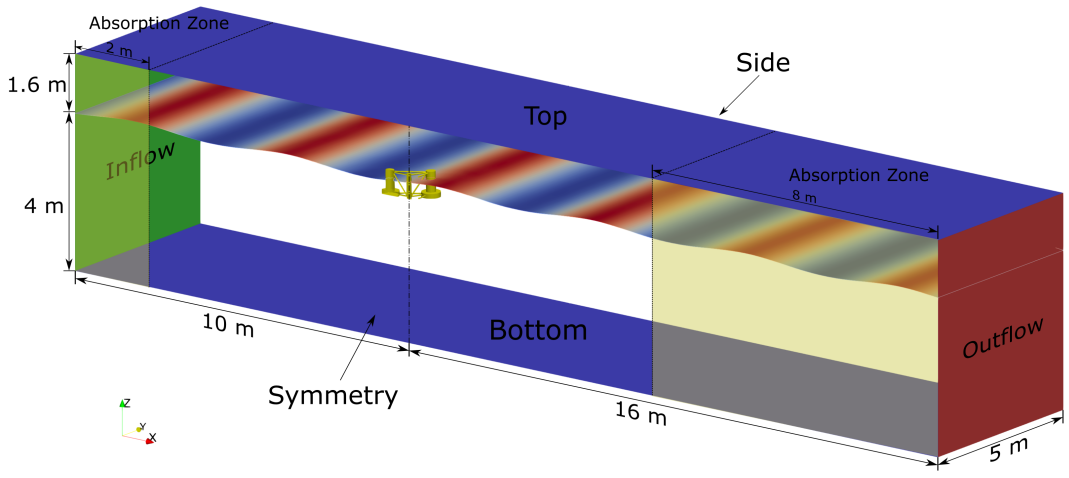

Figure 6.1: Computational domain and the boundary conditions settings in all simulations.

Pure hexahedral unstructured grids are generated in the computational domain. The grids are refined at the near region of the semi-submersible floater and the free surface. The refinement zones are depicted in Fig. 6.2. Detail refinement ratios of the refinement zones are listed in Table

6.1. The reference cell size, h_{ref} is used to concisely describe the grid resolution. For the baseline grid (G2 in the following grid acronyms), the reference grid size is $h_{ref} = 0.008$ m ($H/16$). Such refinement setup is able to capture up to 99.9 % of the wave kinetic energy [31].

Viscous layers are inserted at the near wall regions of the floater with the non-dimensional wall distance value $y^+ < 1.5$. A detail view of the grid is illustrated in Fig. 6.3. Four grids with different grid sizes are generated for the purpose of discretization uncertainty analysis. Number of cells and corresponding refinement factors (with the finest grid denoted as 1) of each grid are summarized in Table 6.2.

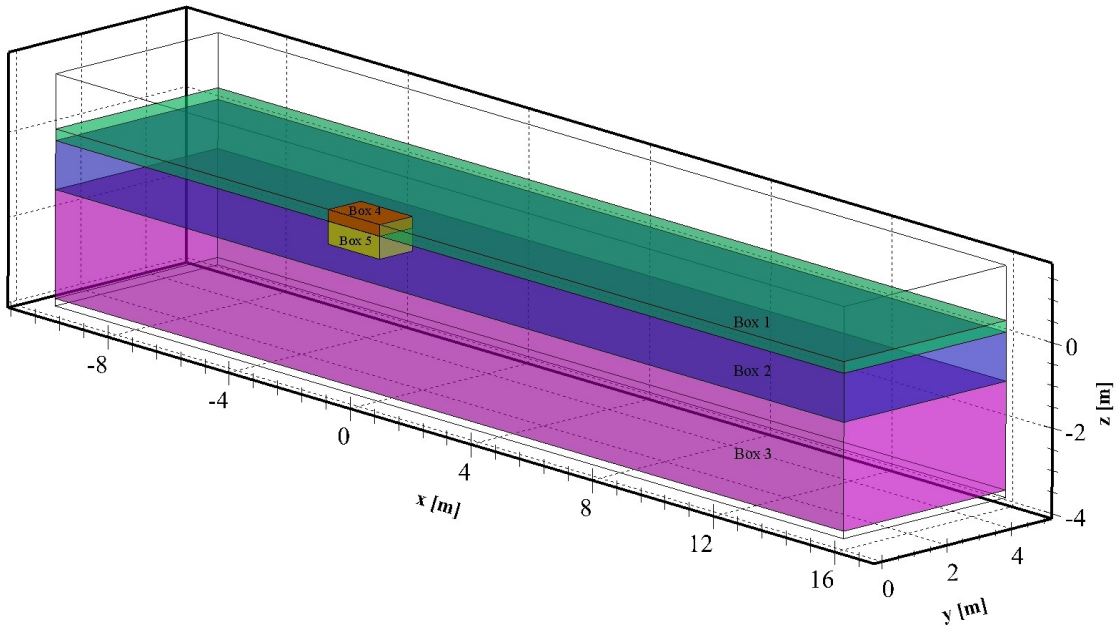

Figure 6.2: Refinement zones division in the computational domain. See detail refinement settings in Table 6.1.

A no-slip condition is assigned to the boundaries of the semi-submersible. A static pressure boundary condition is prescribed at the top of the domain. A slip wall boundary condition is applied at the bottom. On the xOz planar surface and the side plane located at $y = 5$ m, symmetry

Table 6.1: Refinement zones for the computational domain.

Zones	x [m]	y [m]	z [m]	$\Delta x/h_{ref}$	$\Delta y/h_{ref}$	$\Delta z/h_{ref}$
Box 1	$[-10, 16]$	$[0, 5]$	$[-1.2a, 1.4a]$	5	50	1
Box 2	$[-10, 16]$	$[0, 5]$	$[-0.2\lambda, -1.2a]$	10	50	2
Box 3	$[-10, 16]$	$[0, 5]$	$[-0.6\lambda, -0.2\lambda]$	20	50	4
Box 4	$[-1, 0.7]$	$[0, 1]$	$[-1.2a, 1.4a]$	5	5	1
Box 5	$[-1, 0.7]$	$[0, 1]$	$[-0.4, -1.2a]$	10	10	2

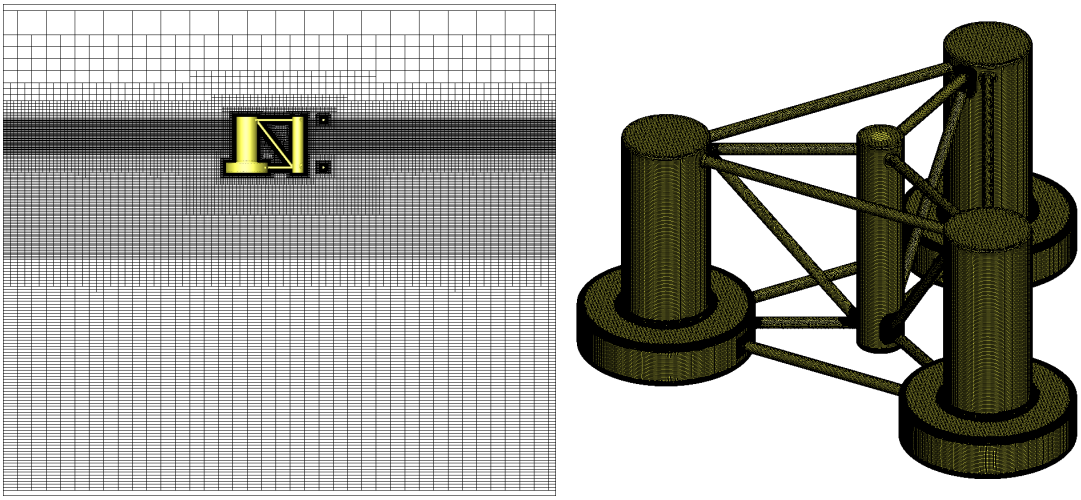

Figure 6.3: Grid refinement at semi-submersible platform and free surface for regular wave load conditions.

Table 6.2: Number of cells and refinement factors of grids for the verification study for regular waves.

Grid acronyms	**Refinement factor**, h_i	**Number of cells**, N_{cell_i}
G1	1.4087	3.793 millions
G2	1.2357	5.619 millions
G3	1.1167	7.615 millions
G4	1.0000	10.603 millions

boundary condition is applied. The outflow boundary is modeled as non-reflecting boundary condition of first-order Sommerfeld type. The phase velocity in the non-reflecting boundary condition is set larger than the theoretical maximum phase velocity that can be form in the wave tank, which is $\sqrt{gd}$. Wave absorption zones of length 2 m at the inlet and 8 m from the outlet are applied, comparing to 0.44 wavelengths for generation and 1.78 wavelengths for absorption.

The motions of the floater is also modelled with deform grid with a support radius of 1.6 m. Solver settings and choices of discretization schemes for each transport equation are listed in Table 6.3. Implicit three time level scheme is utilized for time discretization.

Table 6.3: Numerical settings to solve the governing equations and the convergence tolerance or maximum iterations in regular wave case.

Equation	**Preconditioner**	**Solver**	**Convec. scheme**	**Converg. tol. (Max iter.)**
Momentum	JACOBI	BCGS	HARMONIC	1×10^{-2} (200)
Pressure	BJACOBI	BCGS	-	1×10^{-2} (500)
Free Surface	BJACOBI	GMRES	ReFRICS	1×10^{-2} (200)

Four sets of time step sizes are paired with the grid settings and there are in total 11 simulations for the verification study. The time step sizes range from $\Delta t = 2.5 \times 10^{-3}$ s ($T/684$) to $\Delta t = 1 \times 10^{-2}$ s ($T/171$). Detailed time step settings and refinement factors are listed in Table 6.4.

Table 6.4: Time step size and refinement factor of time step for the verification study for regular waves.

Time step acronyms	**Refinement factor**, t_j	Δt_j (s)
T1	4.00	0.01
T2	2.00	0.005
T3	1.33	0.00333
T4	1.00	0.0025

6.2 Verification study

A guide simulation with baseline setup is performed to help identify the metrics to be studied in this work. The amplitude spectrum of the surge, heave, pitch motion and the wave elevation are present in Figure 6.4. Most significant response occurred at wave frequency f as expected. A critically high response at zero frequency for surge motion is observed, which can be investigated through the mean surge offset and the diff-frequency surge QTF at zero frequency f_0. Additional second order sum-frequency response can be investigated through the RAOs at double wave frequency $2f$. Resonance effect is captured at natural frequency of each DOF.

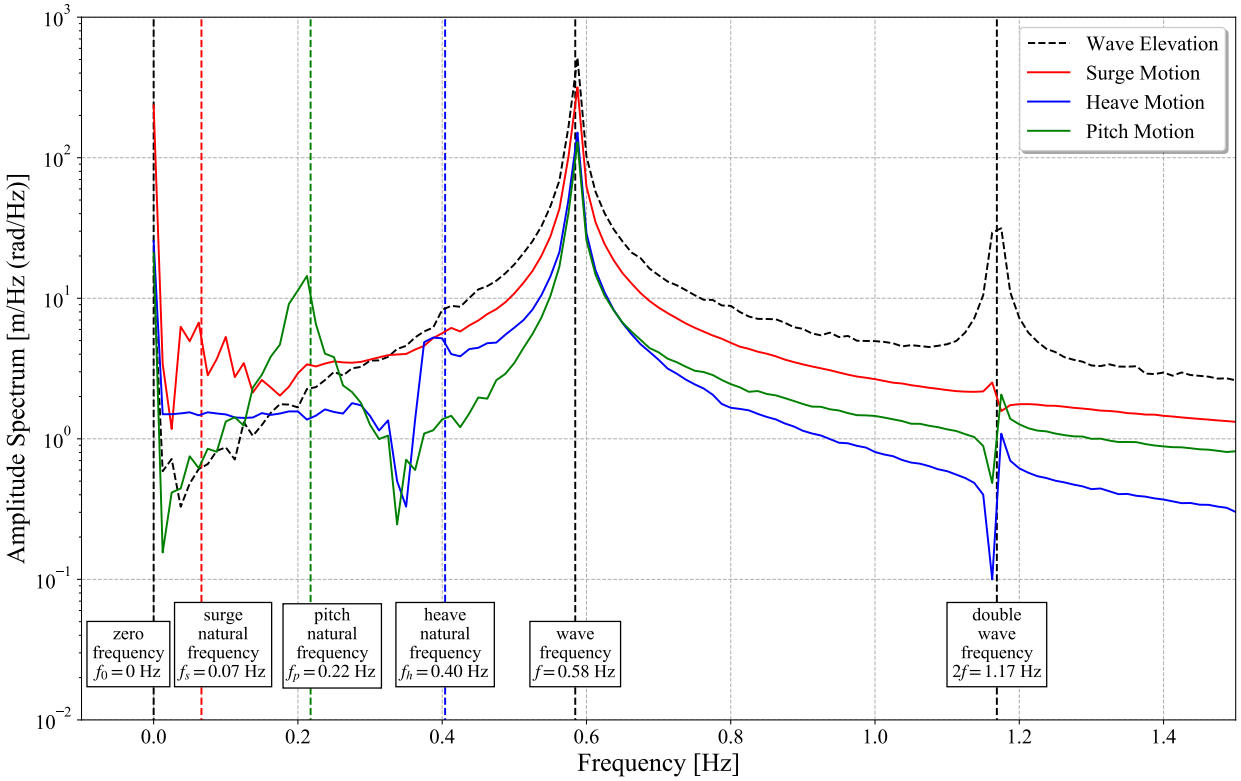

Figure 6.4: The amplitude spectrum of 3-DOF motion and wave elevation.

There are in total eight metrics selected to investigate the hydrodynamic response of semi-submersible platform under regular waves. The metrics and their symbols are listed in Table 6.5

for reference. The first three metrics $\mathrm{SRAO},\ \mathrm{HRAO},\ \mathrm{PRAO}$ represent the linear wave response while the rest 5 metrics $\mathrm{SRAO_2},\ \mathrm{HRAO_2},\ \mathrm{PRAO_2}, \mathrm{MSO}, \mathrm{SQTF_0}$ are selected to study the second order wave response.

Table 6.5: Selected metrics for numerical uncertainty quantification in regular wave case.

Metrics	**Symbol**
Surge RAO at wave frequency	SRAO
Heave RAO at wave frequency	HRAO
Pitch RAO at wave frequency	PRAO
Surge RAO at double wave frequency	$\mathrm{SRAO_2}$
Heave RAO at double wave frequency	$\mathrm{HRAO_2}$
Pitch RAO at double wave frequency	$\mathrm{PRAO_2}$
Mean surge offset	MSO
Zero frequency surge QTF	$\mathrm{SQTF_0}$

Among all simulations, the simulation with grid 2 and time step size 2 (G2T2) is set as the baseline simulation. The quantification of statistical and iterative uncertainty is made with the baseline G2T2 setup.

6.2.1 Statistical uncertainty

To determine a time window for the computation of the metrics, the TST technique is applied to 3-DOF motions of the semi-submersible platform and the wave elevation of the simulated waves to discard the transient phase. The results reveal that except for the surge motion history, all other motions or wave elevation are stationary just after the first oscillation period. The TST result of the surge motion history is present at Fig. 6.5. As shown in the figure, the surge motion history is stationary after 17.6 s of transient phase. Therefore, the time window for the following uncertainty analyses is selected as $[20, 100]$ s. The respective statistical uncertainties of all metrics are listed in Table 6.6.

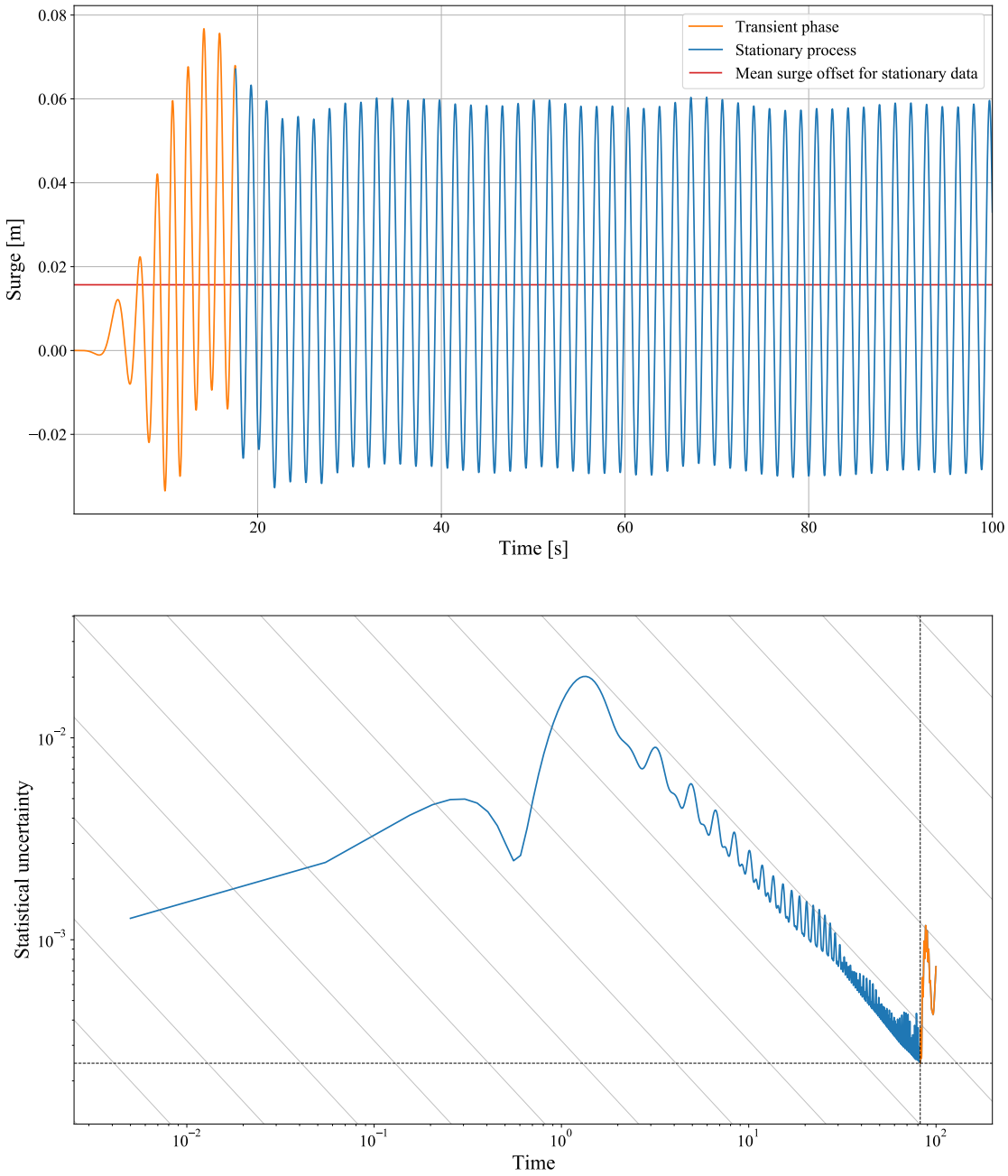

Figure 6.5: Transient scanning results of surge motion of the semi-submersible platform under the regular waves.

6.2.2 Iterative uncertainty

To quantify the iterative uncertainty for the metrics, 4 simulations with G2 and T2 are conducted with different numbers of outer iterations per step. The numbers of iterations are respec-

Table 6.6: The statistical uncertainties of all metrics in selected time window $[20, 100]$ s.

	SRAO	HRAO	PRAO	$SRAO_2$	$HRAO_2$	$PRAO_2$	MSO	$SQTF_0$
U_{st}	0.050%	0.292%	0.167%	0.095%	0.523%	0.688%	2.175%	6.047%

tively 20, 40, 60 and 80. The convergence tolerance is set at 1×10^{-5}. During the selected time window $[20, 100]$ s, none of the simulation could reach below the tolerance in every time step. Hence the L_2 residuals at the last iteration of every time step are collected and the mean of them is used as the convergence tolerance δ_{it} for the computation in Equation 2.48. The L_2 residuals for variables in momentum, pressure and free surface equations are plotted in Figure 6.7. From the observation of the figure, L_2 norm of residuals of velocity in z direction is the highest among all variables. Therefore, the residuals in z momentum equation are used as the convergence tolerance δ_{it}. A plot of the mean residuals within the selected time window versus the number of outer iterations is present as Figure 6.6. A exponential decay pattern can be identified in the figure, indicating that further increasing the number of outer iteration above 80 is not practical. The iterative uncertainties for all metrics are computed and summarized in Table 6.7. Trading off with computing time, 60 outer iterations per time step is chosen as the baseline setup for the following validation study.

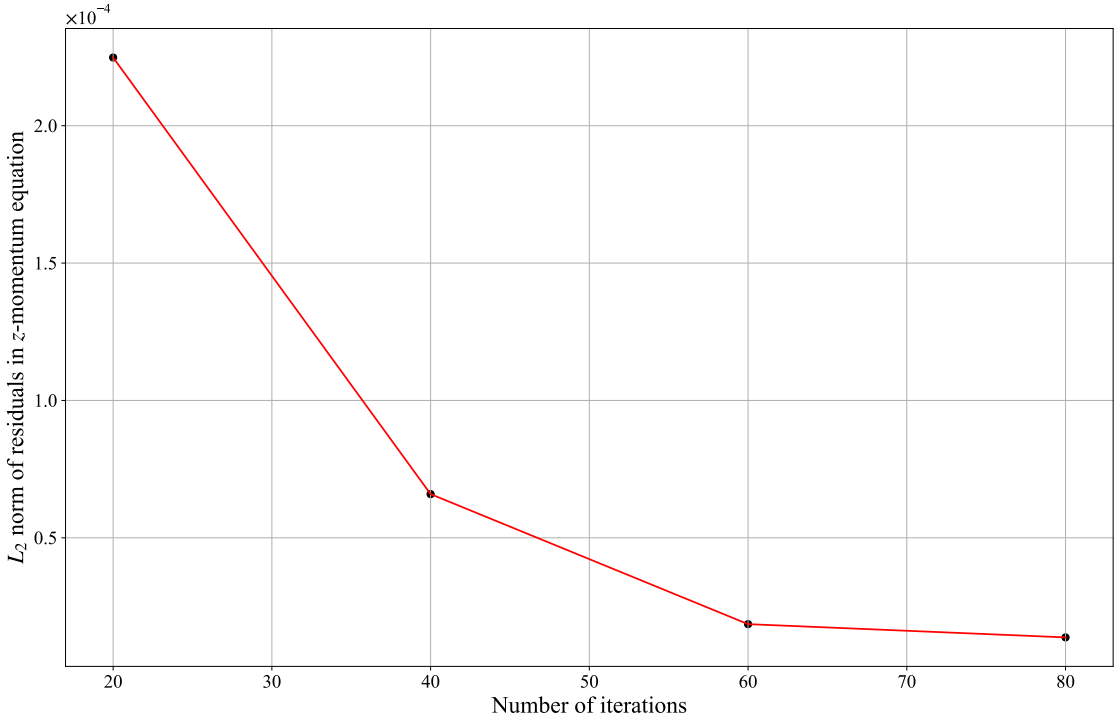

Figure 6.6: Mean L_2 norm residuals of the z momentum equation at the end of every time step within $[20, 100]$ s versus the numbers of outer iterations.

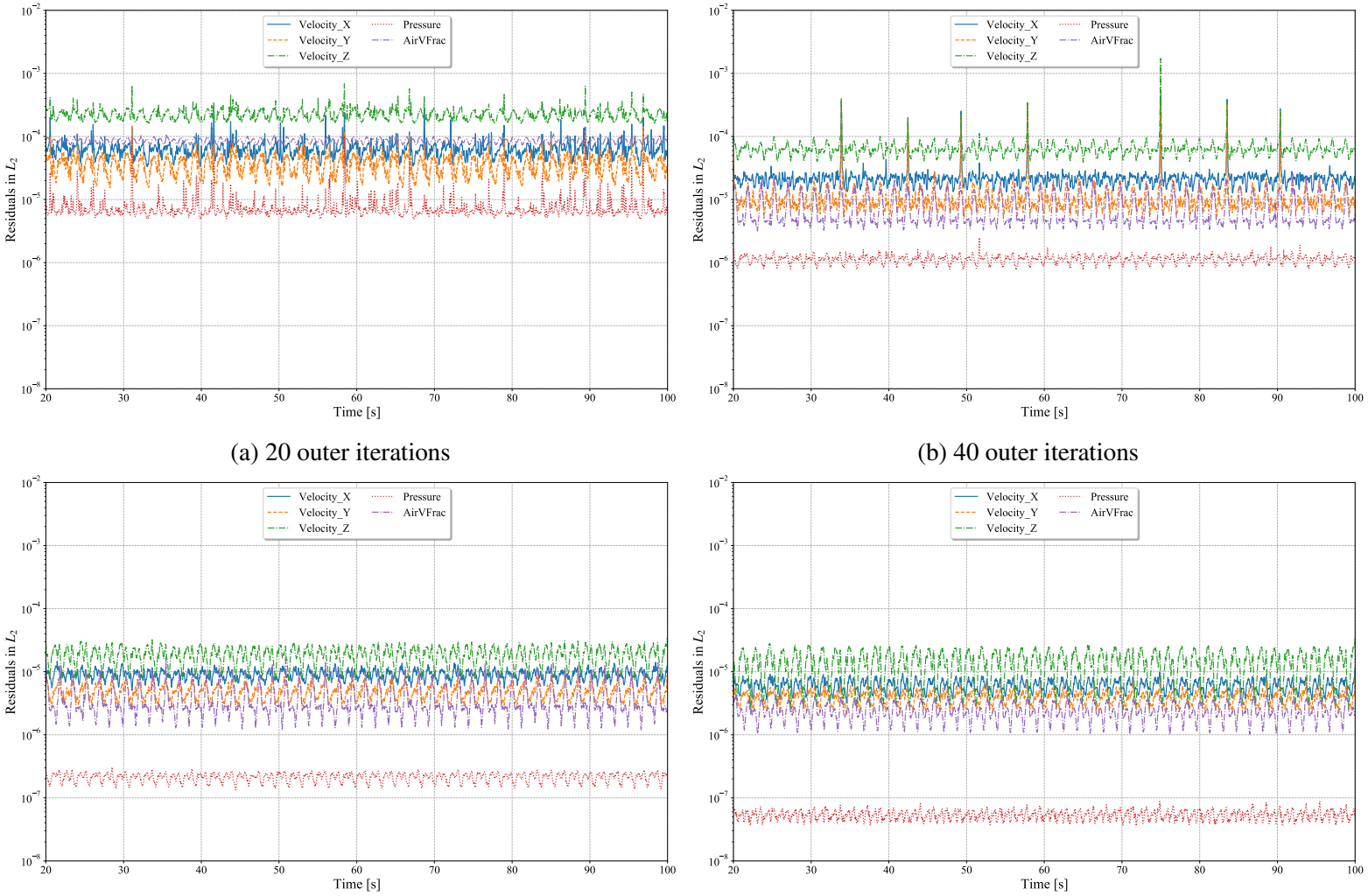

(a) 20 outer iterations

(b) 40 outer iterations

(c) 60 outer iterations

(d) 80 outer iterations

Figure 6.7: Residuals in L_2 norm for 4 simulations with different numbers of outer iterations.

Table 6.7: Iterative uncertainties of all metrics obtained from 4 simulations with different number of outer iterations.

Number of iter.	SRAO	HRAO	PRAO	$SRAO_2$	$HRAO_2$	$PRAO_2$	MSO	$SQTF_0$
20	2.29%	7.61%	4.92%	6.02%	9.53%	2.54%	67.36%	30.32%
40	0.05%	0.53%	0.36%	3.06%	1.43%	1.00%	3.30%	2.86%
60	0.05%	0.30%	0.32%	1.99%	1.22%	0.96%	2.92%	1.62%
80	0.03%	0.49%	0.23%	1.88%	0.77%	0.55%	2.14%	1.97%

6.2.3 Discretization uncertainty

There are in total 11 simulations performed for the discretization uncertainty analysis. The combinations of grids and time step sizes for the 11 simulations are listed in Table 6.8. The maximum theoretical Courant number for each simulation is annotated for reference. The simulations are conducted on clusters provided by Texas A&M University HPRC using 720 Intel Xeon 6248R 3.0 GHz cores. The total wall time for all simulations is about 900 hrs (37.5 days).

Table 6.8: Grid and time step size combinations of 11 simulations for the discretization uncertainty analysis and the corresponding Courant number.

	T1	**T2**	**T3**	**T4**
G1	0.267	0.134	0.089	0.067
G2	-	0.167	0.111	0.083
G3	-	0.223	0.148	0.111
G4	-	-	0.222	-

The wave height time traces and 3-DOF motion histories are plotted at Figure 6.8 for all 11 simulations at a zoomed time frame of $[50, 70]$ s. The horizontal lines in the surge motion plot denote for the mean surge offset. An enlarged view of a oscillation trough is presented on the right to better identify different simulations. All simulations produced similar motion histories in the surge, heave and pitch degrees of freedom. No obvious tendency can be observed in relation with the spatial or temporal sizes used in the simulations.

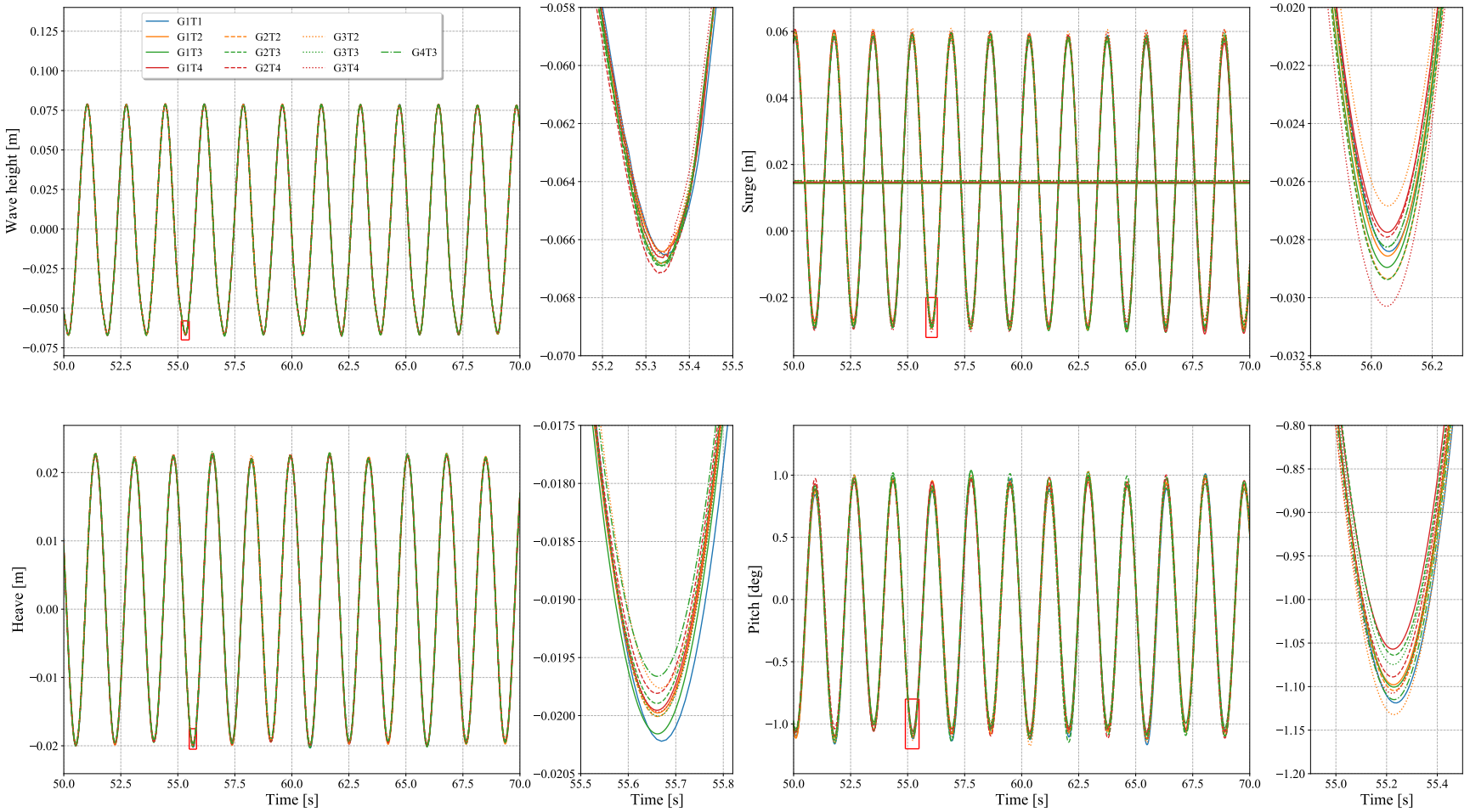

Figure 6.8: Wave heights and motion histories in surge, heave and pitch DOF for 11 simulations conducted for discretization uncertainty analysis.

All 3-DOF motions are oscillating with the same frequency of the wave frequency but with different phases. According to the phase spectrum of 3-DOF motion and wave height (Figure 6.9), the surge motion is nearly out of phase with the waves by a 1.121π difference. The heave motion has a 0.426π phase lag. And the pitch motion is nearly in phase with the waves by a phase difference of 0.092π.

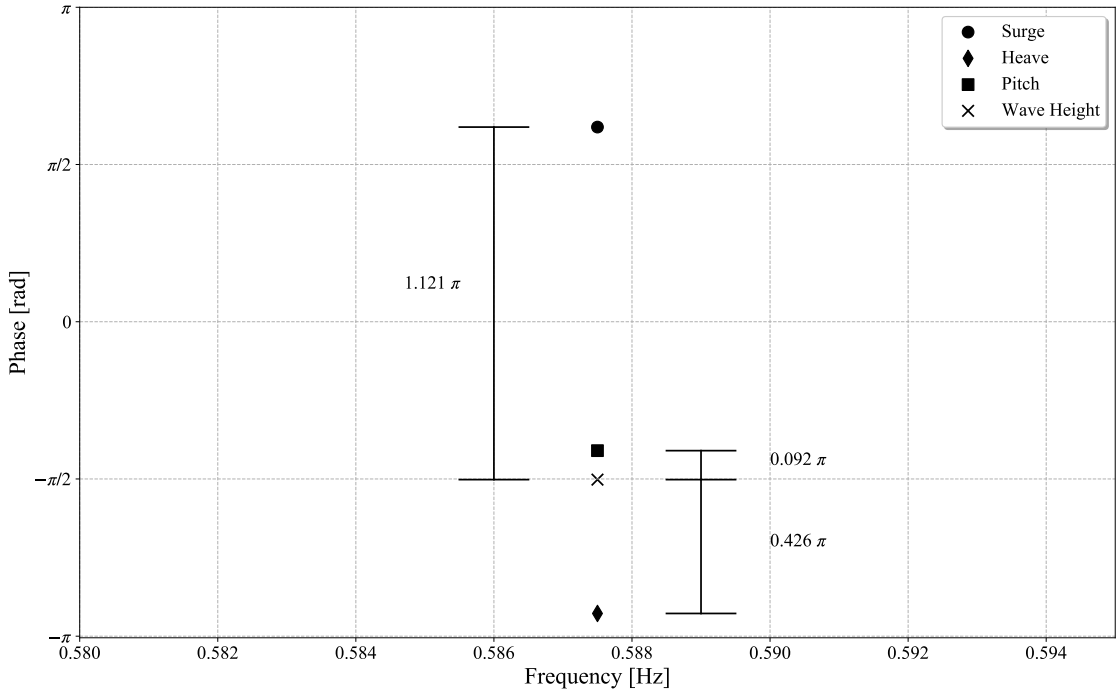

Figure 6.9: Phase spectrum of 3-DOF motion compared with the waves.

The RAOs at wave frequency, double wave frequency in 3-DOF and the mean surge offset, zero frequency surge QTF are derived from the numerical results from all 11 simulations. Direct comparison between different simulations can be inspected in Figure 6.10 - 6.12. The selected metrics obtained from different simulations are very close to each other.

The discretization uncertainty for baseline simulation G2T2 is quantified based on these results. The 3D fit for the metrics are plotted in Figure 6.13 and the final results are listed in Table 6.9. Higher discretization uncertainty is obtained for RAOs at double wave frequency with the highest

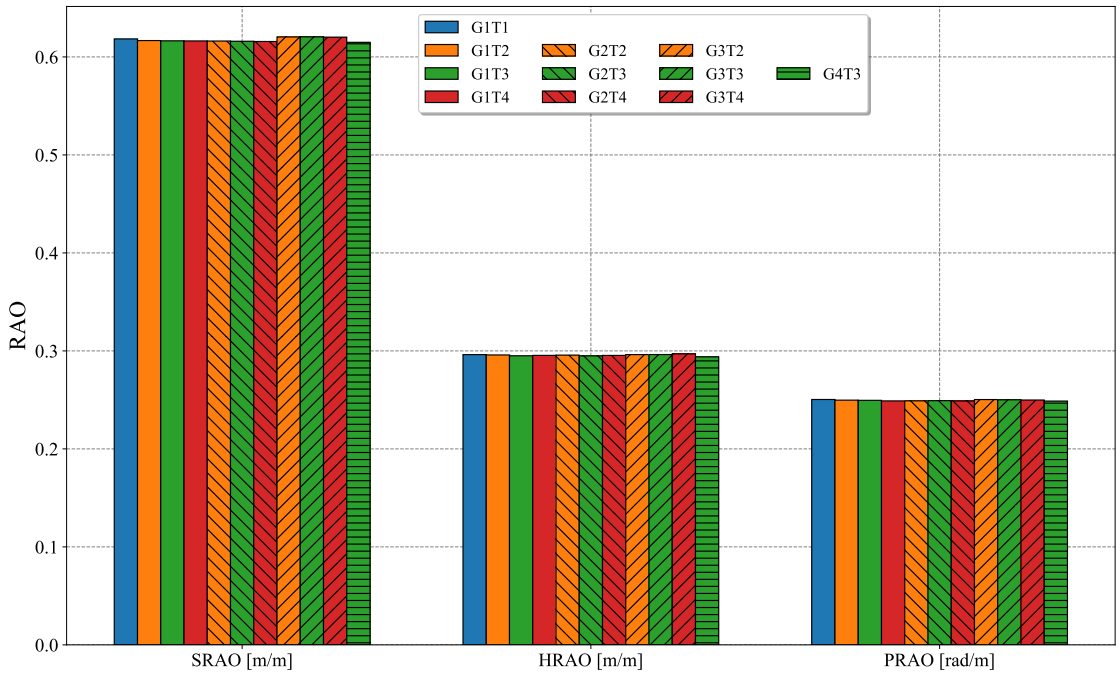

Figure 6.10: Surge, heave and pitch RAOs at wave frequency calculated from the 11 simulations for discretization uncertainty analysis.

for SRAO_2 at over 60 %. The discretization uncertainties for MSO and SQTF_0 are moderate at around 20 % and the discretization uncertainties for RAOs at wave frequency are even smaller. By inspection of the error constants, the magnitudes of the spatial error constants α_x are larger than temporal error constants α_t. The differences are above or close to one order of magnitude. Such comparison indicate that the discretization uncertainty weighs more in space and less in time.

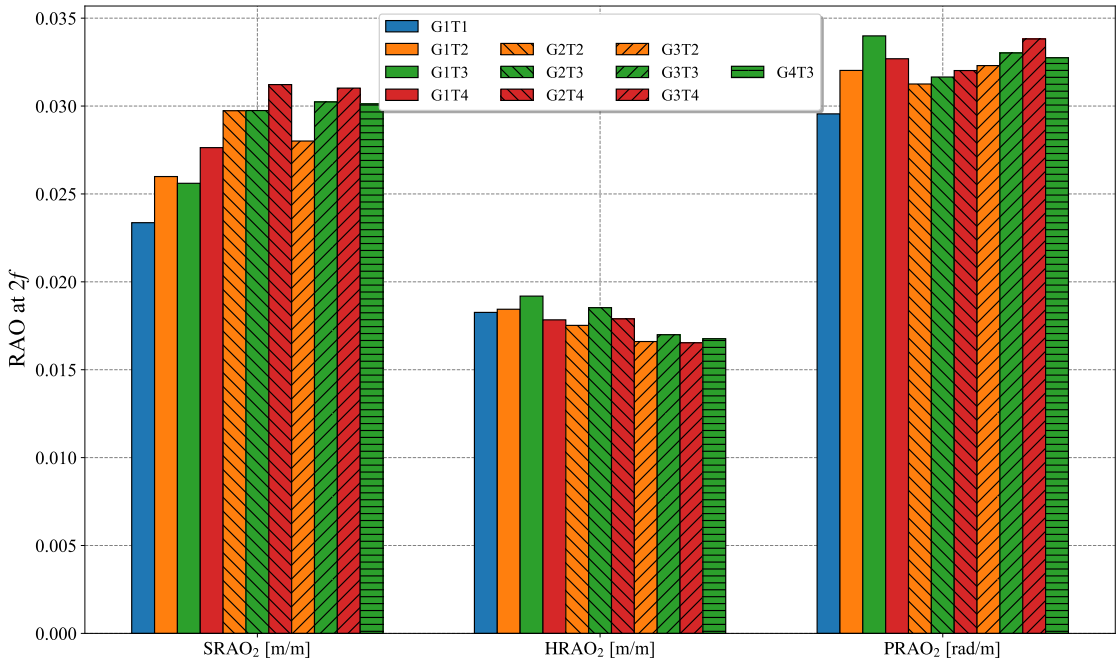

Figure 6.11: Surge, heave and pitch RAOs at double wave frequency calculated from the 11 simulations for discretization uncertainty analysis.

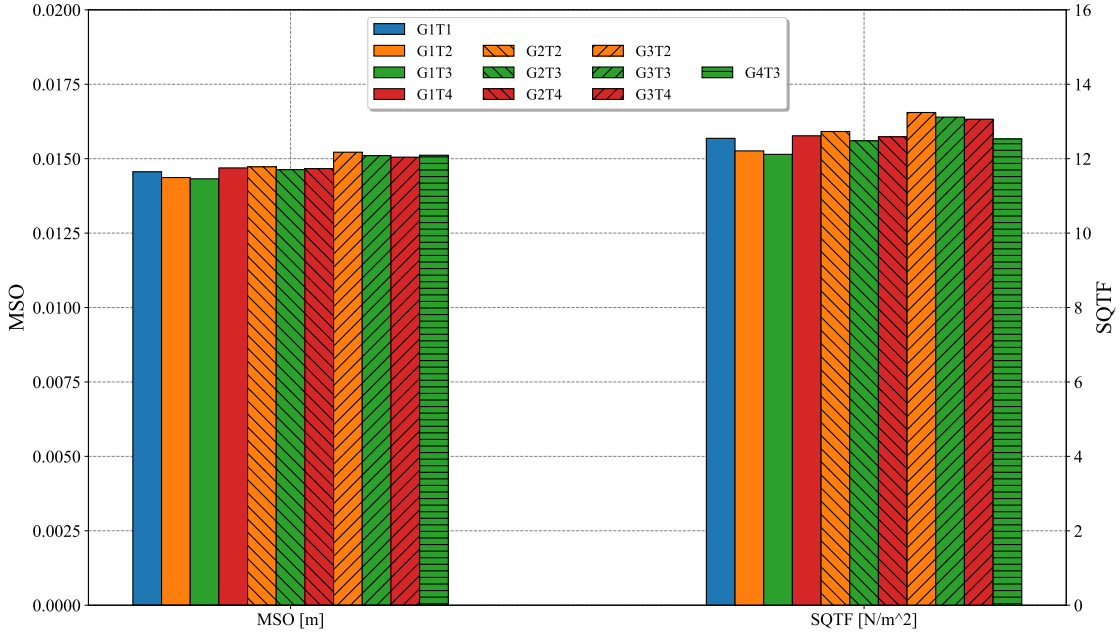

Figure 6.12: Mean surge offset and zero frequency surge QTF calculated from the 11 simulations for discretization uncertainty analysis.

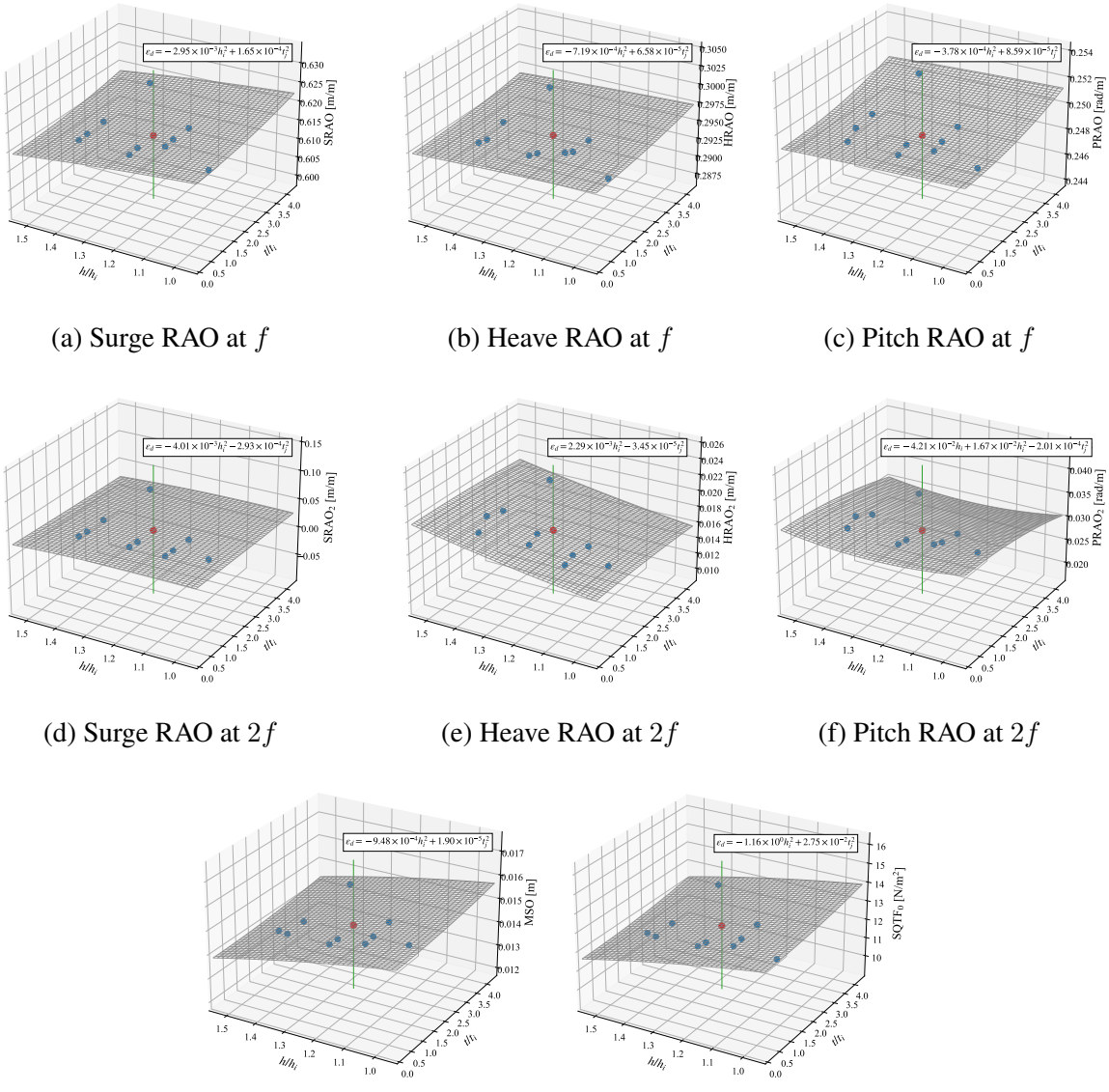

(a) Surge RAO at f (b) Heave RAO at f (c) Pitch RAO at f

(d) Surge RAO at $2f$ (e) Heave RAO at $2f$ (f) Pitch RAO at $2f$

(g) Mean surge offset (h) Zero frequency surge QTF

Figure 6.13: 3D fit of all metrics in regular wave case with green bar representing discretization uncertainty bounds for simulation G2T2 (denoted as red dot).

Table 6.9: Discretization uncertainties of all the metrics obtained from 11 simulations with different grids and/or time step sizes. The error constants and order of convergence in space and time as described in Equation 2.51 are attached.

	Ext. value ϕ_0	**G2T2 solution** ϕ_1	**Discr. unc.** U_ϕ	α_x	p_x	α_t	p_t
SRAO	6.2163×10^{-1}	6.1621×10^{-1}	2.707%	-2.95×10^{-3}	2.0	1.65×10^{-4}	2.0
HRAO	2.9665×10^{-1}	2.9571×10^{-1}	2.938%	-7.19×10^{-4}	2.0	6.58×10^{-5}	2.0
PRAO	2.4986×10^{-1}	2.4904×10^{-1}	1.951%	-3.78×10^{-4}	2.0	8.59×10^{-5}	2.0
SRAO_2	3.5736×10^{-2}	2.9734×10^{-2}	60.557%	-4.01×10^{-3}	2.0	-2.93×10^{-4}	2.0
HRAO_2	1.4214×10^{-2}	1.7523×10^{-2}	45.472%	2.29×10^{-3}	2.0	-3.45×10^{-5}	2.0
PRAO_2	5.8946×10^{-2}	3.1254×10^{-2}	42.580%	$^*-4.21 \times 10^{-2}, 1.67 \times 10^{-2}$	$^*1.0, 2.0$	-2.01×10^{-4}	2.0
MSO	1.6148×10^{-2}	1.4726×10^{-2}	18.213%	-9.48×10^{-4}	2.0	1.90×10^{-5}	2.0
SQTF_0	1.4408×10^{1}	1.2730×10^{1}	26.489%	-1.16×10^{0}	2.0	2.75×10^{-2}	2.0

* Fit is made using first and second order exponents as $\alpha_{x1}h_i + \alpha_{x2}h_i^2$.

6.2.4 Total numerical uncertainty

Gathering the statistical, iterative and discretization uncertainties, the total numerical uncertainty can be computed using equation 2.62. The total numerical uncertainties based on numerical results obtained by G2T2 using 60 outer iterations are listed in Table 6.10. In the total numerical uncertainty of all metrics, the discretization uncertainty is considered as the dominant source of numerical uncertainty, weighing above 80%. For numerical uncertainties of RAOs, the discretization uncertainty is nearly the only contributor. Moreover, within the discretization uncertainty, the spatial discretization uncertainty is more important than temporal discretization uncertainty. Therefore, it is advocated to perform at least discretization uncertainty analysis for CFD simulations of FOWT under regular waves to obtain an approximation of numerical uncertainty level. Specifically the spatial discretization uncertainty should be quantified at the first priority.

Table 6.10: The total numerical uncertainties of all metrics for G2T2 simulation with 60 outer iterations per time step.

	Statistical unc. U_{st}	**Iterative unc.** U_{it}	**Discretization unc.** U_d	**Total numerical unc.** U_N
SRAO	0.050%	0.047%	2.707%	2.755%
HRAO	0.292%	0.304%	2.938%	3.256%
PRAO	0.167%	0.322%	1.951%	2.279%
SRAO_2	0.095%	1.985%	60.557%	62.542%
HRAO_2	0.523%	1.218%	45.472%	46.692%
PRAO_2	0.688%	0.962%	42.580%	43.548%
MSO	2.175%	2.920%	18.213%	21.245%
SQTF_0	6.047%	1.620%	26.489%	28.752%

Table 6.11: The component uncertainties, validation uncertainty and comparison error of investigated metrics for the semi-submersible platform under regular wave condition. Judgement of validation is determined by direct comparion of E and U_V.

	Total exp. unc. $\sqrt{U_{exp}^2 + U_I^2}$	**Numerical unc.** U_N	**Validation unc.** U_V	**Numerical value** ϕ_N	**Exp. value** ϕ_{exp}	**Comp. error** E	**Validated?**
SRAO	3.179%	2.755%	4.206%	6.1621×10^{-1}	5.9206×10^{-1}	4.080%	Yes
HRAO	5.111%	3.256%	6.060%	2.9571×10^{-1}	3.0138×10^{-1}	1.882%	Yes
PRAO	5.117%	2.279%	5.602%	2.4904×10^{-1}	2.4342×10^{-1}	2.308%	Yes
$SRAO_2$	N/A	62.542%	62.542%	2.9734×10^{-2}	6.0705×10^{-2}	51.020%	Yes
$HRAO_2$	N/A	46.692%	46.692%	1.7523×10^{-2}	1.4862×10^{-2}	17.907%	Yes
$PRAO_2$	N/A	43.548%	43.548%	3.1254×10^{-2}	3.6599×10^{-2}	14.603%	Yes
MSO	24.431%	21.245%	32.376%	1.4726×10^{-2}	9.1202×10^{-3}	61.470%	No
$SQTF_0$	N/A	28.752%	28.752%	1.2730×10^{1}	6.9959×10^{0}	81.967%	No

6.3 Validation study

The validation uncertainty U_V is computed by root sum of squares of total numerical uncertainty (U_N) and total experimental uncertainty (U_{exp}, U_I) obtained from [46]. The total experimental uncertainty for mean surge offset under current wave condition was overstated in that study, which is probably caused by calibration issue in the computations. By investigation of the total experimental uncertainty for mean surge offset in other wave conditions, stabler uncertainty levels around 20 - 30 % are observed. Therefore, an average value of them is taken as the total experimental uncertainty of mean surge offset under current wave condition. Moreover, the total experimental uncertainty for the second-order metrics, i.e. the RAOs at double wave frequency and zero frequency surge QTF is not given. Therefore, the validation uncertainty for these metrics is merely contributed by the numerical uncertainty.

Validation is examined based on the validation uncertainty and the comparison error between experimental measurements and numerical simulations of the metrics. The uncertainty levels, comparison errors and judgements of whether validation is achieved are listed in Table 6.11. The comparison between numerical results and experimental measurements with uncertainty bounds are depicted in Figure 6.14. Numerical results using linear mooring model are also added for reference.

Inspecting the RAOs at wave frequency in surge, heave and pitch motions (SRAO, HRAO, PRAO), all of them have a relatively small comparison error between numerical and experimental results. Validation is achieved in all three metrics. In the RAOs at wave frequency obtained by linear mooring model, none of them has achieved validation with the experimental results. For the RAOs at double wave frequency ($SRAO_2$, $HRAO_2$, $PRAO_2$) larger numerical uncertainties are observed, which leads to successful validation against experimental results in all three metrics despite that comparison error of $SRAO_2$ is as large as 51 %. As for the linear mooring model, $HRAO_2$ fails the validation. In comparison between linear and dynamic mooring model, utilization of dynamic mooring model has shown improvement in predicting the RAOs. Such improvement indicates that a dynamic mooring model should always be applied to obtain an accurate prediction

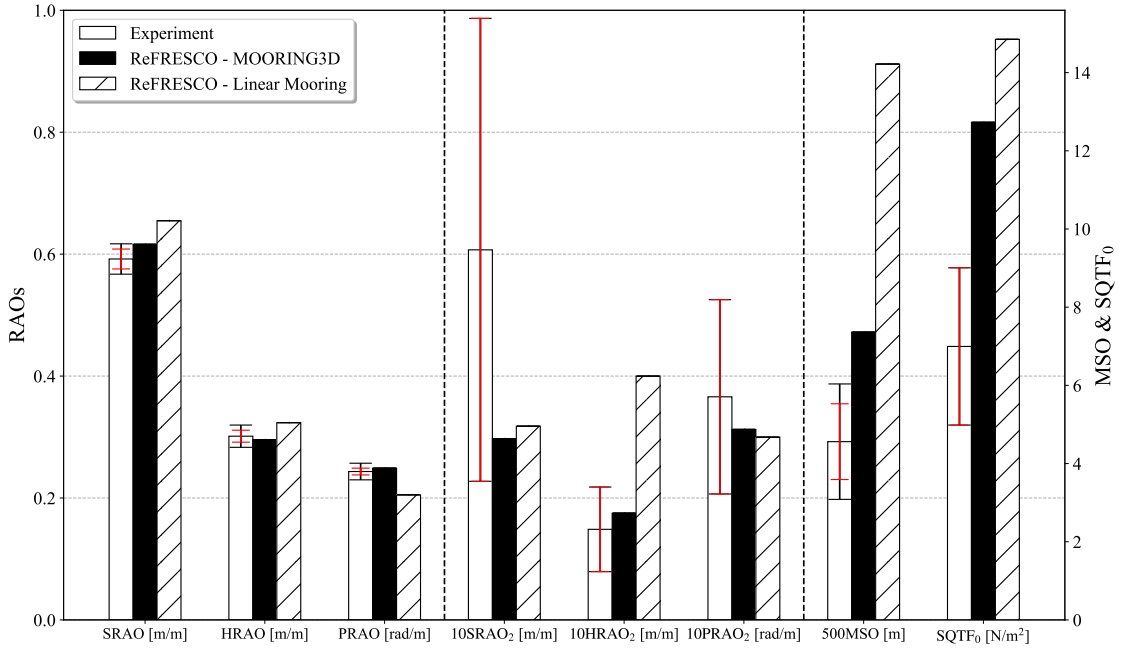

Figure 6.14: Validation of RAOs, MSO and $SQTF_0$ between numerical results and experimental measurements. The red uncertainty bands represent the total numerical uncertainty and the black ones represent the validation uncertainty. The RAOs at double wave frequency are scaled up by a factor of 10 and the MSO is scaled up by a factor of 500.

of RAOs in regular waves.

From the previous verification study, we observed that the discretization uncertainty contributes the most to the numerical uncertainty of double wave frequency RAOs, especially the spatial discretization uncertainty. Therefore, the high numerical uncertainty of double wave frequency RAOs is most possibly caused by limited mesh resolution for the small wave amplitude at double wave frequency. More finer meshes are suggested to estimate the numerical uncertainty of double wave frequency responses of FOWT in regular waves.

From Table 6.11, the experimental uncertainty of MSO is higher than that of RAOs at wave frequency, showing a similar pattern with the numerical uncertainty, which further increase the validation uncertainty. However, the comparison error of MSO is still larger than the validation uncertainty - the numerical simulation over-predicts the MSO with a 61 % difference. Similarly, over-prediction is found at the $SQTF_0$ with a 82 % comparison error. Therefore, validation is not

achieved for MSO and $SQTF_0$. This is also revealed in the Figure 6.14. The numerical simulation with linear mooring model has a even larger MSO and $SQTF_0$. The reason is obvious since linear mooring model cannot provide sufficient surge restoring forces. However, the over-prediction of both metrics by dynamic mooring model needs further investigation.

From the overview of the validation study, the missed validation is obtained at MSO and $SQTF_0$. Moreover, the comparison error of SRAO and $SRAO_2$ is very close to the corresponding validation uncertainty where validation is reluctantly achieved. The results are foreseeable based on a difference between numerical simulation and experimental setups mentioned in the experiment report [1] and in the previous study [13]. According to the experiment report, a large cable bundle was hanging off the tower in the model test and could create additional stiffness and pre-load for the system. Since the exact value of the additional stiffness in the surge direction is unknown, it was not applied in the previous study for pitch decay motion and is not applied in present work either. The additional surge stiffness is the most possible reason causing the over-prediction in MSO and $SQTF_0$.

With the thorough verification and validation study in CFD simulations of the OC5 DeepCwind semi-submersible platform under regular waves, the coupled ReFRESCO - MOORING3D numerical tool is capable to accurately predict the 3-DOF RAOs. Yet the prediction of the mean surge offset doesn't match with experiments even with a large uncertainty level, which indicates that the innate physics of mean surge offset is more sensitive to different setups in experiments or simulations.

7. V&V STUDY OF FOWT SEMI-SUBMERSIBLE PLATFORM UNDER IRREGULAR WAVES

7.1 Benchmark case: focused waves

To calibrate the performance of ReFRESCO in generation of irregular waves, a benchmark case of a focused wave generation is simulated. The case configuration of the benchmark case is taken from a comparative study presented in ISOPE 2020 led by Sriram et al. [55]. In this study, experiments of a fixed monopile undertaking uni-directional focusing waves were conducted and the measurements are available to any interested research group. The comparative study considers the wave generation and propagation, wave loads on the fixed and moving cylinder. However, the scope of this benchmark case is to calibrate the ability to generate irregular wave of ReFRESCO. Therefore, solely irregular wave generation and propagation is investigated. ReFRESCO is used to simulate the exact conditions as in experiment and comparison between the numerical and experimental results is made.

7.1.1 Case description and numerical settings

The experiments are performed using a wave tank with 110 m length, 2.2 m width and 2 m depth. Waves are generated by a computer controlled hydraulically driven wave maker at one end of the tank. The tank is filled with fresh water to a depth of 0.7 m. The wave tank is depicted in Figure 7.1. Wave probes are placed at seven locations along the centerline of the wave tank and around the cylinder. In the benchmark case, the first four wave probes are of interest. The positions of the first four wave probes are listed in Table 7.1. The unidirectional focusing waves are generated by the second order wavemaker theory [56] using a constant steepness spectrum of 32 components ranging from 0.34 to 1.02 Hz. The detail wave characteristics are listed in Table 7.2, where f_1 is the starting frequency in the spectrum, f_N is the last frequency component in the spectrum, N is the total number of wave frequency components used in the wave packets, t_f is the theoretical focusing time used to generate the time series, G_a is the amplitude gain parameter used

to obtain the amplitude of every component in the spectrum with respect to k_i, i.e. $a_i = G_a/k_i$, where k_i is the wave number corresponding to f_i. By applying the discrete FFT to the wave elevation time series at the WP1, the amplitude spectrum of the focused wave is depicted as Figure 7.2.

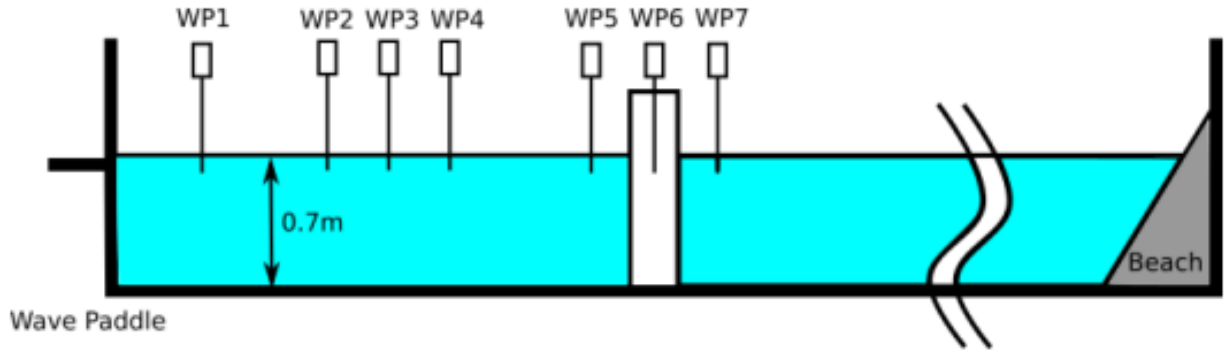

Figure 7.1: Illustration of the wave tank and the locations of the wave probes.

Table 7.1: Positions of the wave probes to be investigated with the x measured from wave paddle and y measured from side wall.

Wave probe	x (m)	y (m)
WP1	4.975	1.085
WP2	13.928	1.085
WP3	14.178	1.085
WP4	14.428	1.085

Table 7.2: Wave characteristics of the benchmark focused wave case.

	f_1	f_N	N	t_f	G_a
values	0.34	1.02	32	38	0.001

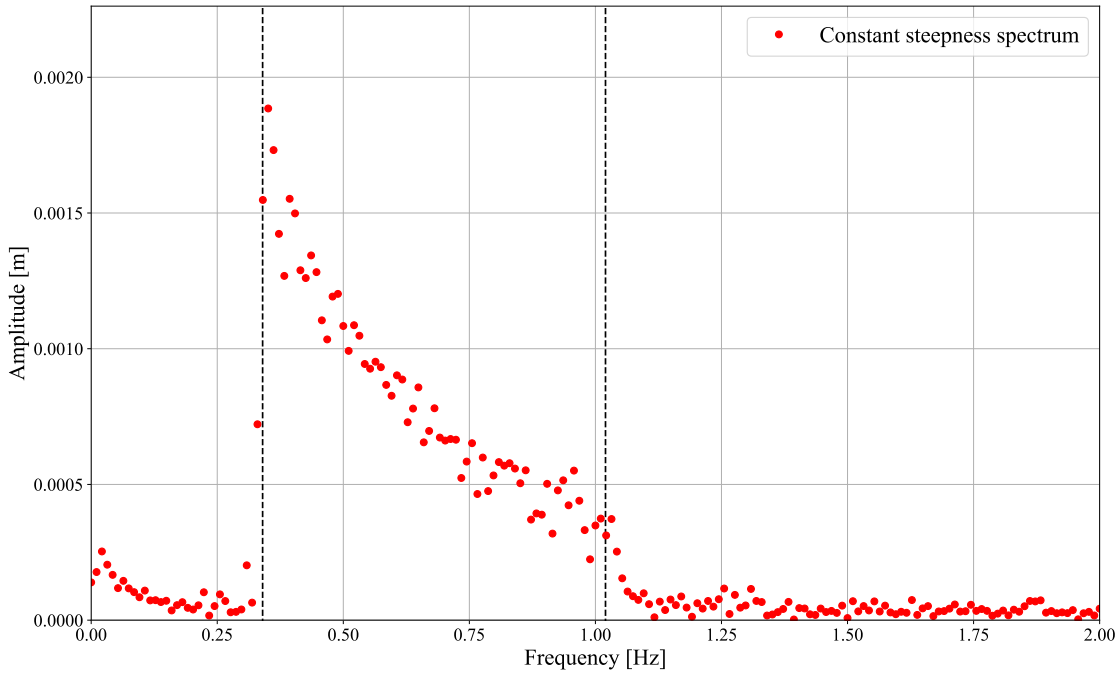

Figure 7.2: The wave amplitude spectrum of the focused waves.

A computational domain is constructed with the same width (2.2 m) and depth (2 m) of the wave tank but truncated in length (50 m) for a cost-friendly purpose. The domain is meshed with unstructured grid with refinement around and below the free surface. Such that the refined region could resolve the free surface waves up to two times of the highest wave amplitude obtained in the amplitude spectrum ($2a_{max}$). The grid is illustrated in Figure 7.3. The total cell count for the grid is 4.72 millions.

The boundary condition settings are similar to regular wave case. The waves are generated at the inflow boundary using 32 wave components sampled from the wave spectrum. Wave absorption zone is set at the last 10 m of the computational domain. The length of the absorption zone is approximately 25 times of the largest wavelength in the spectrum.

The flow is assumed as laminar in this study, hence no turbulence transport equation need to be solved. The time step size for the simulation is $\Delta t = 0.01$ s which is the same as the measuring rate of the experiments.

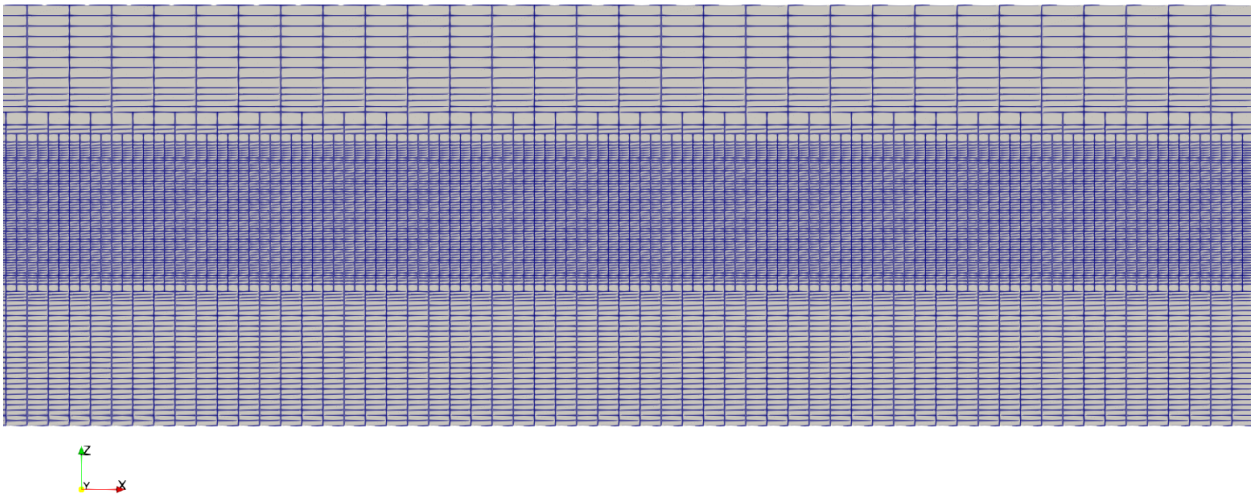

Figure 7.3: The computational domain used in the benchmark focused wave simulation.

7.1.2 Results and discussions

The simulation is complete on Texas A&M University HPRC clusters using 560 Intel Xeon E5-2680 2.40 GHz cores. The total run time for this case is around 8 hrs. Convergence is achieved in every time step within the outer iteration limit (50 iterations).

The wave elevation time series from the numerical simulation and experimental measurement are plotted at Figure 7.4. A time window of [15, 40] s is selected where the focused waves are captured in all four wave probes. By direct line to line comparison, the numerical results are in satisfactory agreement with the experimental data with minor deviations in some of the peaks and troughs. However, the small amplitude high frequency oscillations at around 35 s of WP1 in experimental data are not captured in the simulation. This is due to a measurement noise in the experiments or a nonlinear development of the waves. A wave paddle motion history is provided with the experimental report where no high frequency movement exhibits, indicating that the high frequency oscillations are not generated directly by the wave makers. Moreover, several CFD simulations of this test case [57, 58] using the wave paddle movements to generate the waves

showed the same results, indicating that the high frequency oscillations are not a result of nonlinear development of focused waves. Therefore, the measurement noise is the most possible cause of the high frequency oscillations. This again emphasize the importance for a experimental uncertainty analysis.

Based on the previous observation and discussion, ReFRESCO is capable to reconstruct irregular focused wave time series based on the provided 32 wave components. The numerical waves also propagated as like in a real wave tank. The following verification and validation study of bichromatic waves and random waves are feasible to perform.

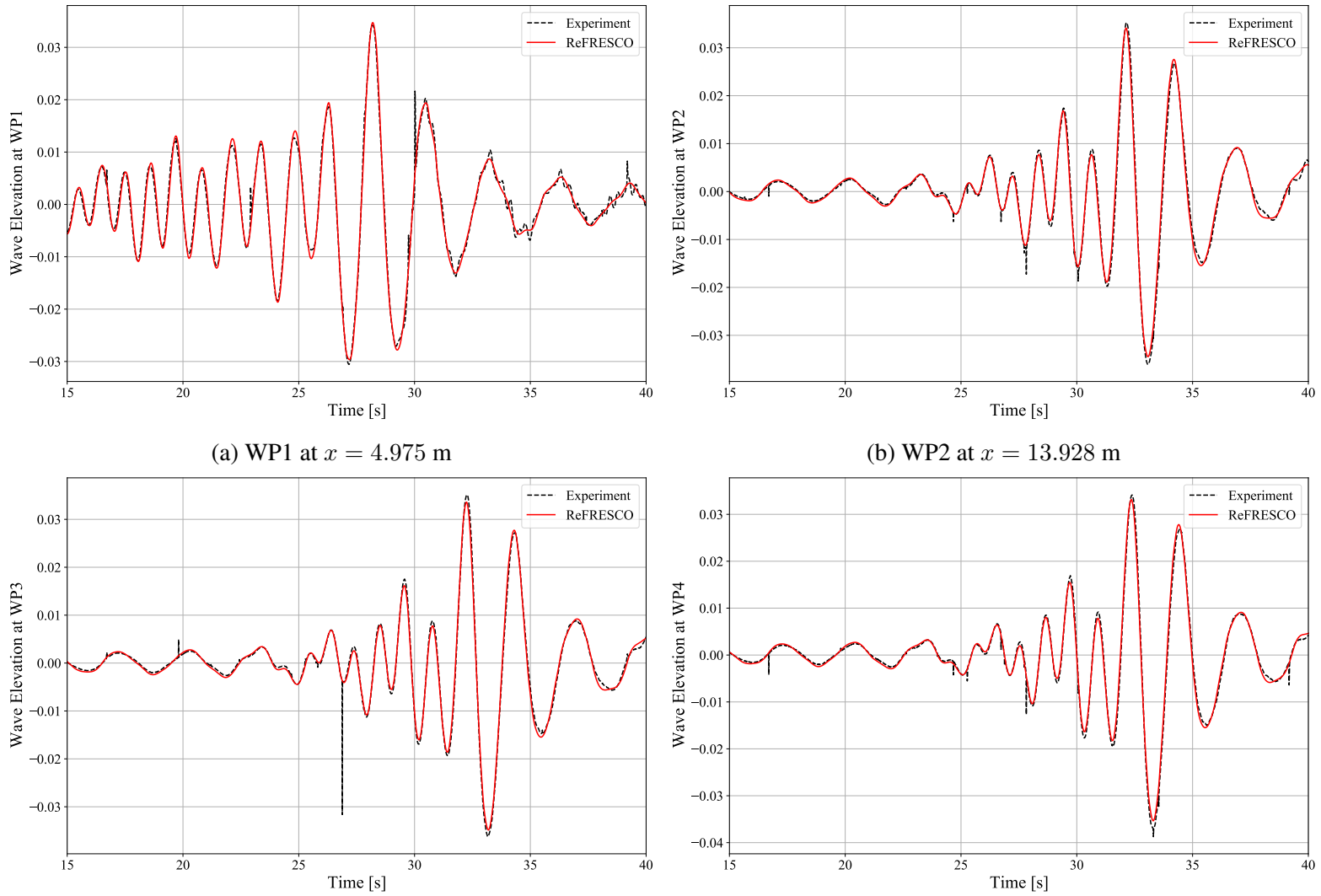

(a) WP1 at $x = 4.975$ m

(b) WP2 at $x = 13.928$ m

(c) WP3 at $x = 14.178$ m

(d) WP4 at $x = 14.428$ m

Figure 7.4: Wave elevation time series at WP1-4 from the focused wave simulation in comparison with experimental data.

7.2 Bichromatic waves

7.2.1 Numerical settings

The computational domain used in bichromatic waves condition is the same as the domain used in regular wave condition with enlarged refine regions around and beneath the free surface to resolve the sum amplitude of the two wave components. The dimensions of refinement boxes are the same as listed in Table 6.1 but with reference wave amplitude $a = a_1 + a_2$ and reference wavelength $\lambda = \lambda_1 + \lambda_2$. The wave absorption zones are also enlarged accordingly.

Three set of grids are prepared for the discretization uncertainty quantification. The number of cells and corresponding refinement factors are listed in Table 7.3. The time step size settings are listed in Table 7.4. Among the combinations of grids and time step sizes, simulation G2T2 is selected as the baseline setup.

Table 7.3: Number of cells and refinement factors of grids for the verification study for bichromatic waves.

Grid acronyms	**Refinement factor**, h_i	**Number of cells**, N_{cell_i}
G1	1.2615	3.967 millions
G2	1.1066	5.877 millions
G3	1.0000	7.964 millions

Table 7.4: Time step size and refinement factor of time step for the verification study for bichromatic waves.

Time step acronyms	**Refinement factor**, t_j	Δt_j (s)
T1	4.00	0.01
T2	2.00	0.005
T3	1.00	0.0025

7.2.2 Verification study

Based on the numerical results of baseline setup, the amplitude spectrum of the surge, heave, pitch motion and the wave elevation are present in Figure 7.5. Significant responses occurred at wave frequency f_1 and f_2 as expected. A critically high response at zero frequency for surge response is observed, which can be investigated through the mean surge offset and the diff-frequency surge QTF at zero frequency f_0. Second order responses can be investigated through the RAOs at wave sum-frequency $f_1 + f_2$ and wave diff-frequency $f_2 - f_1$. Resonance effect is captured at natural frequency of each DOF. Particularly, the wave diff-frequency is adjacent to pitch natural frequency and causing a critical pitch response at wave diff-frequency.

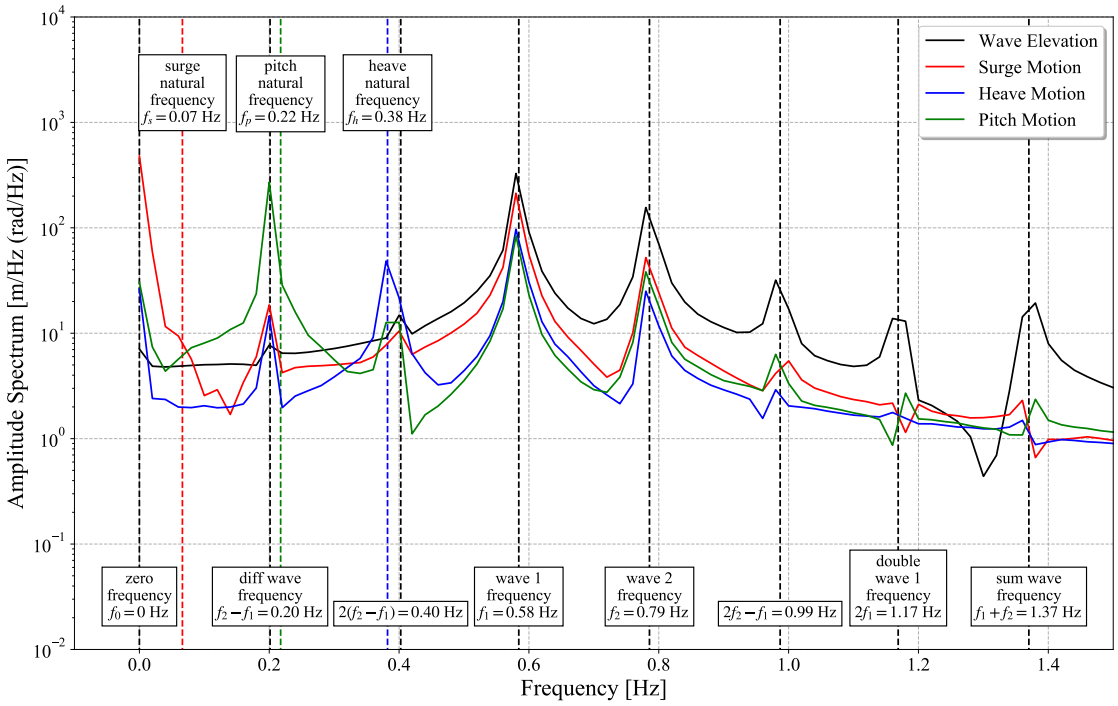

Figure 7.5: The amplitude spectrum of 3-DOF motion and wave elevation in bichromatic wave condition.

In total 14 metrics are selected for the verification study of bichromatic wave case as listed in Table 7.5. The RAOs at both wave frequencies are investigated for the first order wave response

and the others for the second order wave response.

Table 7.5: Selected metrics for numerical uncertainty quantification in bichromatic wave case.

Metrics	**Symbol**
Surge RAO at wave frequency 1	SRAO_1
Heave RAO at wave frequency 1	HRAO_1
Pitch RAO at wave frequency 1	PRAO_1
Surge RAO at wave frequency 2	SRAO_2
Heave RAO at wave frequency 2	HRAO_2
Pitch RAO at wave frequency 2	PRAO_2
Surge RAO at wave sum-frequency	SRAO_+
Heave RAO at wave sum-frequency	HRAO_+
Pitch RAO at wave sum-frequency	PRAO_+
Surge RAO at wave diff-frequency	SRAO_-
Heave RAO at wave diff-frequency	HRAO_-
Pitch RAO at wave diff-frequency	PRAO_-
Mean surge offset	MSO
Zero frequency surge QTF	SQTF_0

According to the observations in regular wave case, the statistical and iterative uncertainties are neglected in this verification study. Only the discretization uncertainty is the quantified in the following analyses. However, TST technique is applied to select a proper time window to compute for the metrics. Moreover, iterative residuals for all simulations with different combination of grid and time step size are investigated to ensure the solutions have converged to certain level.

The TST technique is applied to the surge, heave and pitch motion histories of the semi-submersible platform. The results show that except for the surge motion history, all other motions are stationary at around 10 s. The TST result of the surge motion history is present at Fig. 7.6. As shown in the figure, the surge motion history is stationary after 64.8 s of transient phase with a statistical uncertainty of 0.12 %. However, to ensure adequate time length for the calculation of RAOs in wave diff-frequency, the time window of $[40, 100]$ s with second least statistical uncertainty 0.14% is selected.

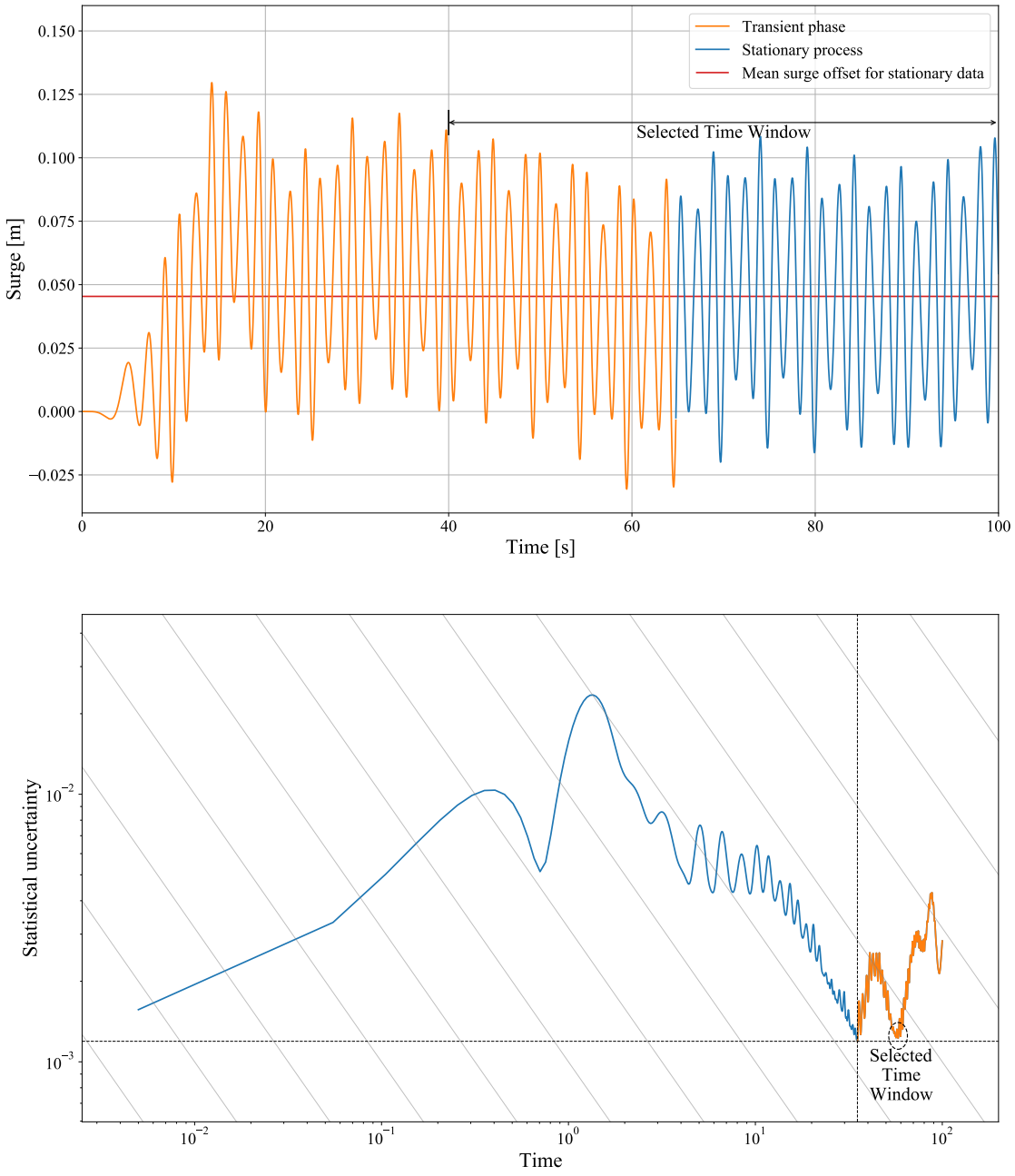

Figure 7.6: The time history of surge motion of semi-submersible under bichromatic waves with the transient phase marked as orange. Below is the time length T vs. the statistical uncertainty to judge if the signal is stationary.

The spatial discretization uncertainty is found to be the primary source of numerical uncertainty. Hence in the quantification of discretization uncertainty in the bichromatic wave case, each grid is paired with only two or fewer time step sizes, resulting in 5 simulations to be studied with.

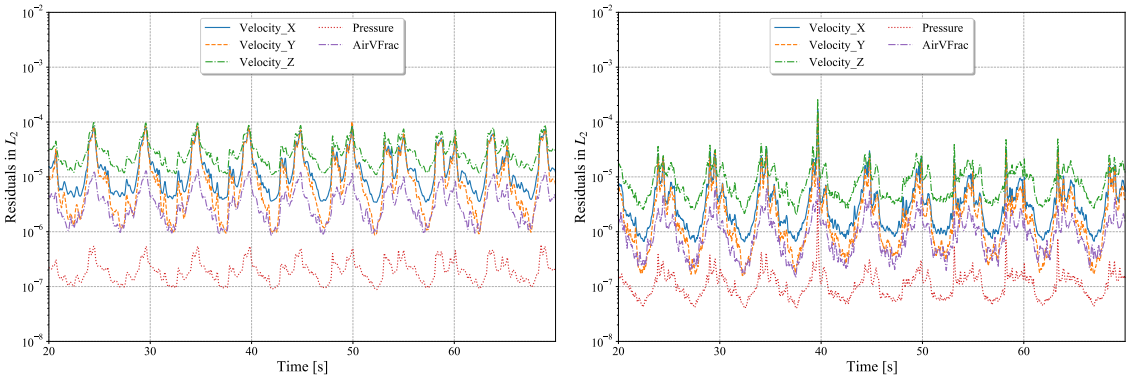

(a) Simulation G1T1

(b) Simulation G1T2

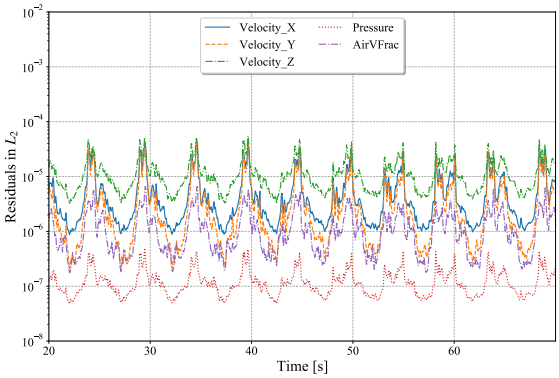

(c) Simulation G2T2

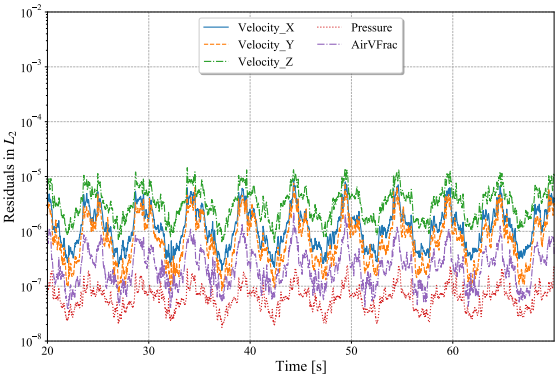

(d) Simulation G2T3

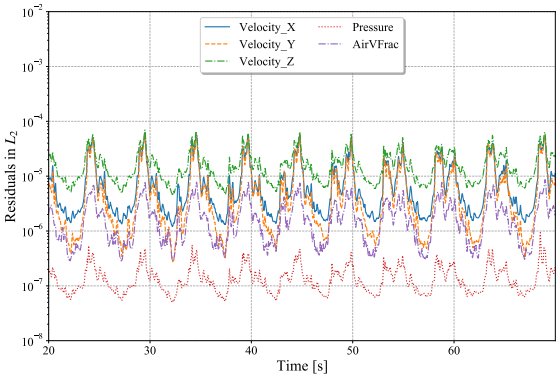

(e) Simulation G3T2

Figure 7.7: Residuals in L_2 norm for 5 simulations with different combination of grid and time step sizes.

The combinations of grid and time step size with the corresponding theoretical Courant number is listed in Table 7.6. The L_2 norm of convergent residuals of all variables of all 5 simulations are then investigated as shown in Figure 7.7. Most of the L_2 residuals for all simulations have fallen

below the level of 10^{-4} which indicates the iterative uncertainty is safe to be neglected.

Table 7.6: Grid and time step size combinations of 5 simulations for the discretization uncertainty analysis and the corresponding Courant number in bichromatic wave case.

	T1	**T2**	**T3**
G1	0.267	0.134	-
G2	-	0.167	0.083
G3	-	0.223	-

The simulations are conducted on Grace clusters provided by Texas A&M University HPRC using 720 Intel Xeon 6248R 3.0 GHz cores. The total wall time for all simulations is about 380 hrs (15.8 days). The wave elevation and 3-DOF motion time histories are plotted at Figure 7.8 for all 5 simulations at a time window of $[50, 70]$ s. The horizontal lines in the surge motion plot denote for the mean surge offset. An enlarged view of a oscillation trough is presented on the right side to identify the small discrepancies between simulations. All simulations produced very close wave elevation time history and similar motion histories in the heave and pitch degrees of freedom. However, the deviations are larger in surge motion histories of different simulations. Moreover, the motion discrepancies between different simulations are larger than that in the regular wave case. This is expected since bichromatic waves exhibit more non-linearity than regular waves which is sensitive to the grid resolution in CFD simulations. Difference in grid resolution would largely affect the generation and propagation of bichromatic waves, especially when the grid is unable to resolve the wave amplitude of the diff-frequency of the two wave components.

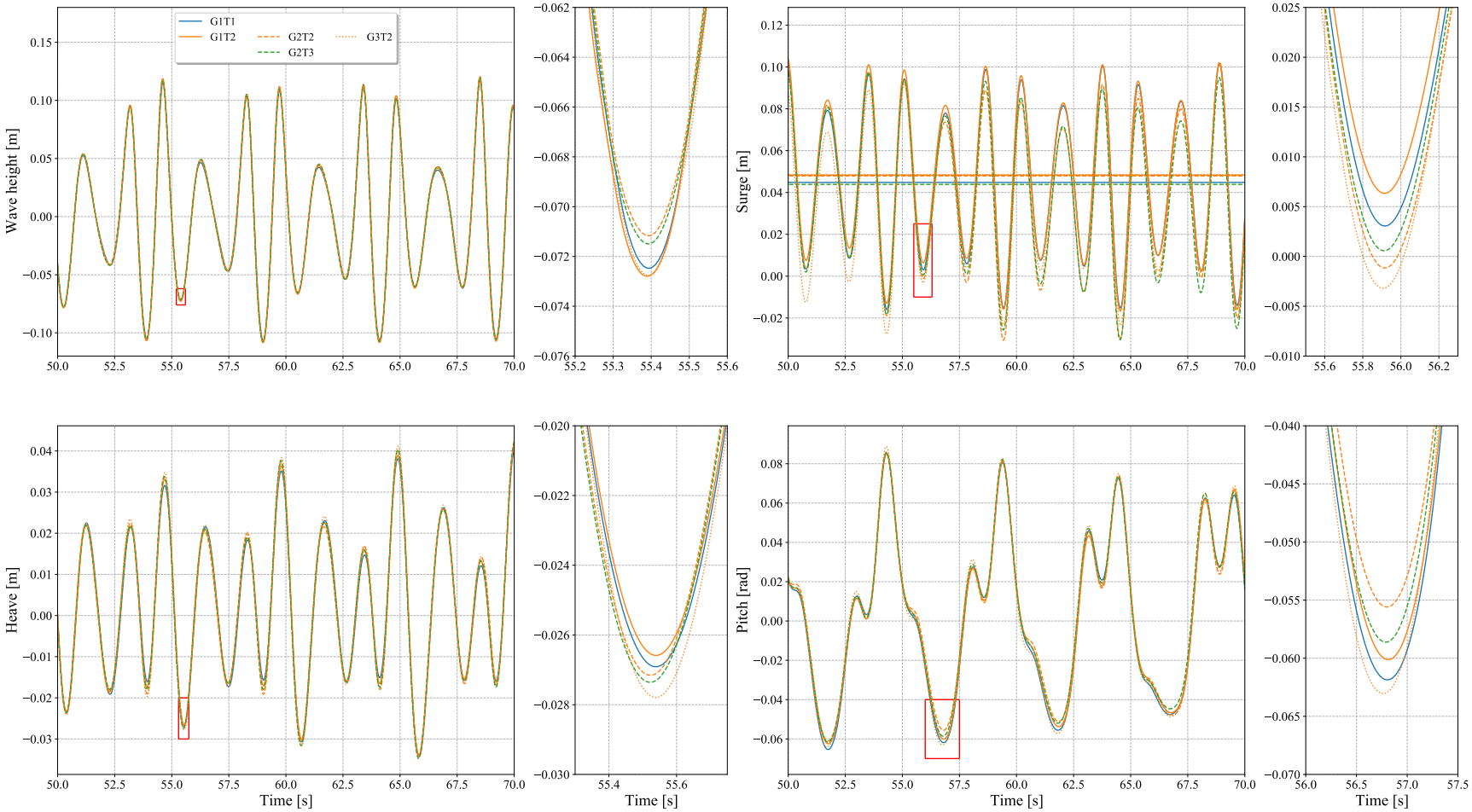

Figure 7.8: Wave elevation and motion time histories in surge, heave and pitch DOF for 5 simulations conducted for discretization uncertainty analysis in bichromatic wave cases.

The RAOs at two wave frequencies, wave sum-frequency, wave diff-frequency in 3-DOF and the mean surge offset, zero frequency surge QTF are derived from the numerical results from all 5 simulations. Direct comparison between different simulations is presented in Figure 7.9 - 7.11.

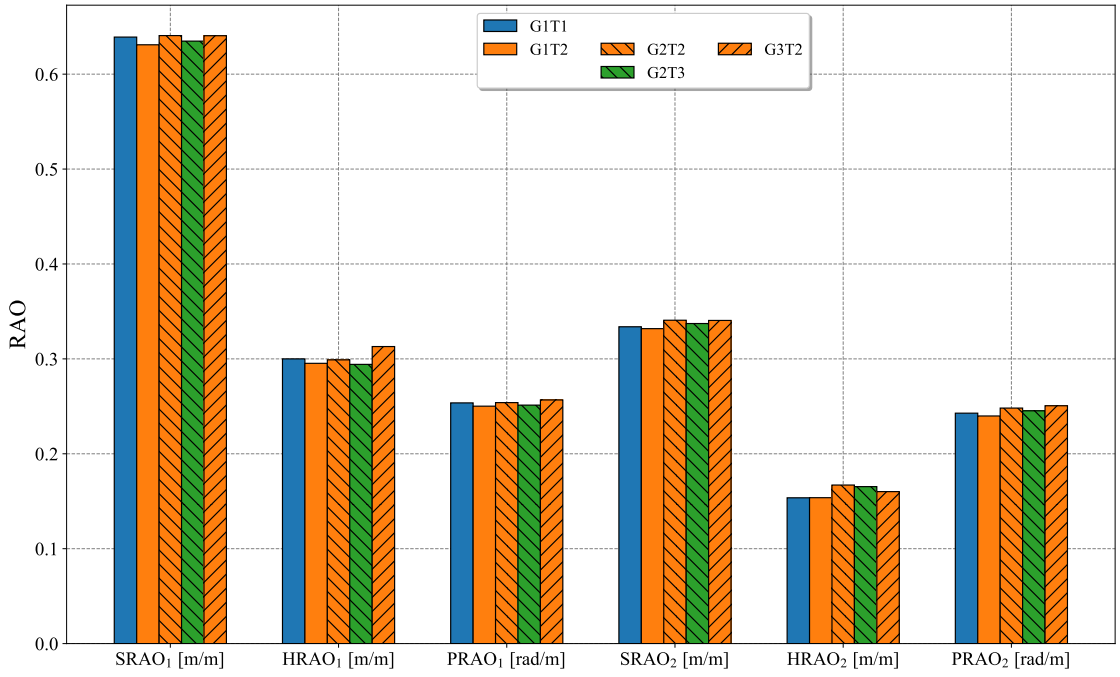

Figure 7.9: 3-DOF RAOs at wave frequency 1 and wave frequency 2 calculated from the 5 simulations for discretization uncertainty analysis in bichromatic wave case.

The discretization uncertainty for baseline simulation G2T2 is quantified based on these results. The 3D fit for the metrics are plotted in Figure 7.12 and the final results are listed in Table 7.7. The discretization uncertainty for all metrics has fallen below 20 % except for surge, heave RAO at diff-frequency, mean surge offset and zero frequency surge QTF. The discretization uncertainty for metrics related with second order surge response ($SRAO_+$, $SRAO_-$, MSO and $SQTF_0$) is generally higher than the other two DOFs. Satisfactory level of discretization uncertainty has achieved for the RAOs of first order response and for second order response RAO at heave and pitch DOFs. Similar to the previous discretization uncertainty quantification, the magnitudes of the spatial error constants α_x are larger than temporal error constants α_t. Such comparison reaffirms that the

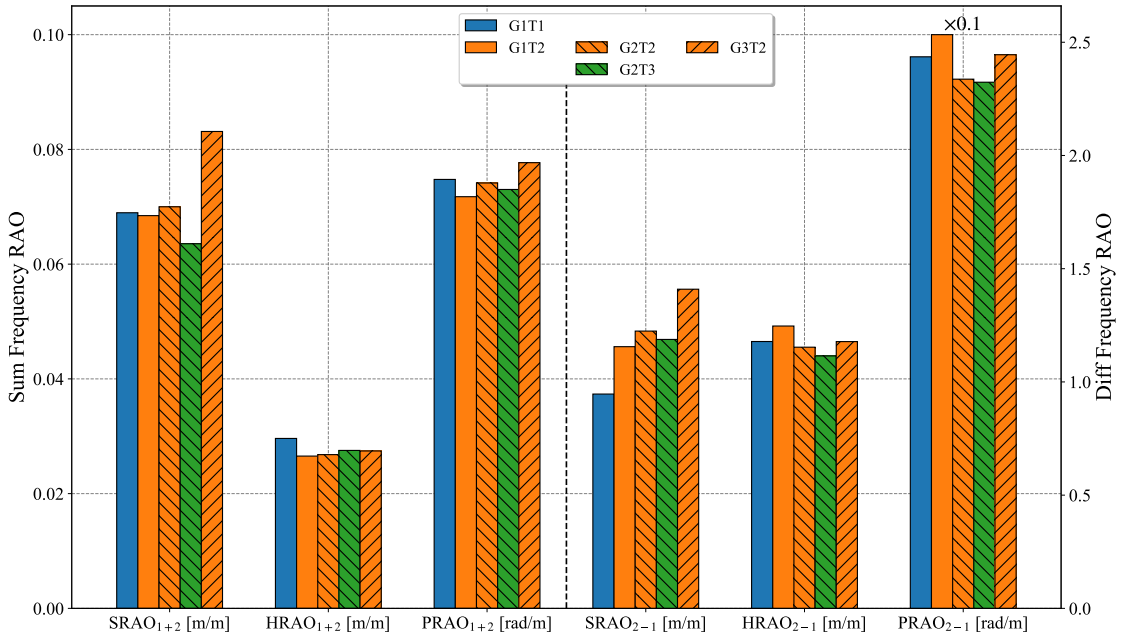

Figure 7.10: 3-DOF RAOs at wave sum-frequency and diff-frequency calculated from the 5 simulations for discretization uncertainty analysis in bichromatic wave case.

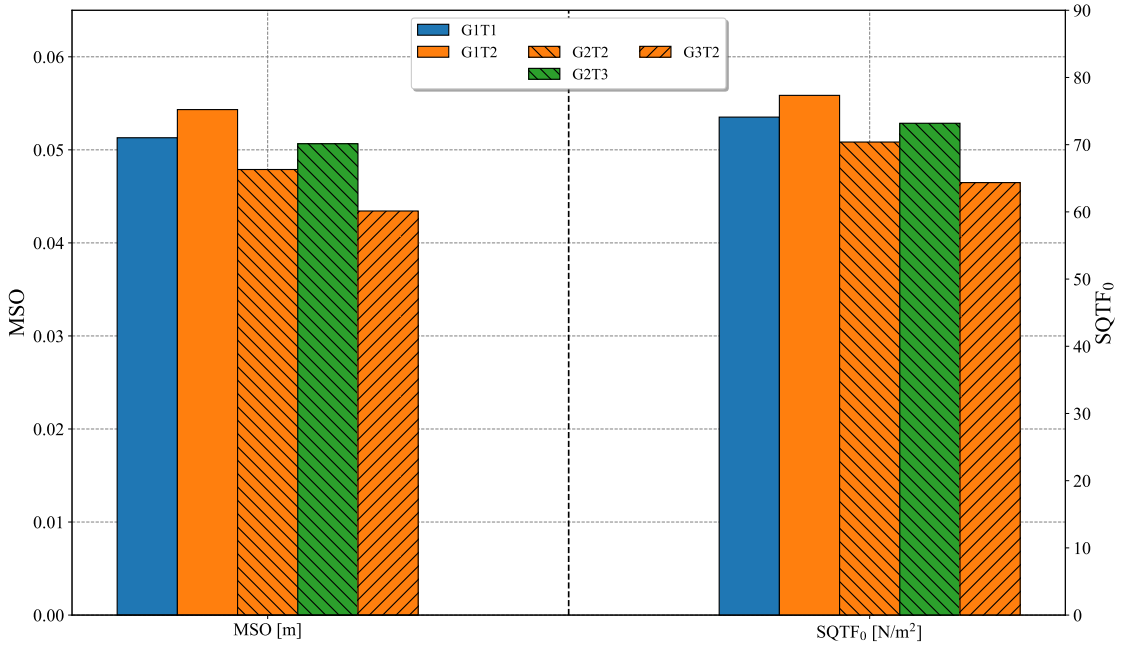

Figure 7.11: Mean surge offset and zero frequency surge QTF calculated from the 5 simulations for discretization uncertainty analysis in bichromatic wave case.

discretization uncertainty weighs more in space and less in time.

The numerical uncertainty in bichromatic wave case is purely contributed by discretization uncertainty. Hence, the spatial discretization uncertainty is the most significant source of numerical uncertainty. The high numerical uncertainty obtained for metrics related with surge direction indicates that for a bichromatic wave case, the grid spacing in surge direction should be taken good care with. In general, 50 cell points per wavelength should be acquired with the wavelength taken as the shorter wavelength at sum-frequency. Since no experimental data is available for the free floating semi-submersible platform under bichromatic waves, validation study is not performed. The numerical uncertainty quantified in bichromatic wave case is utilized to demarcate the uncertainty bound for random waves.

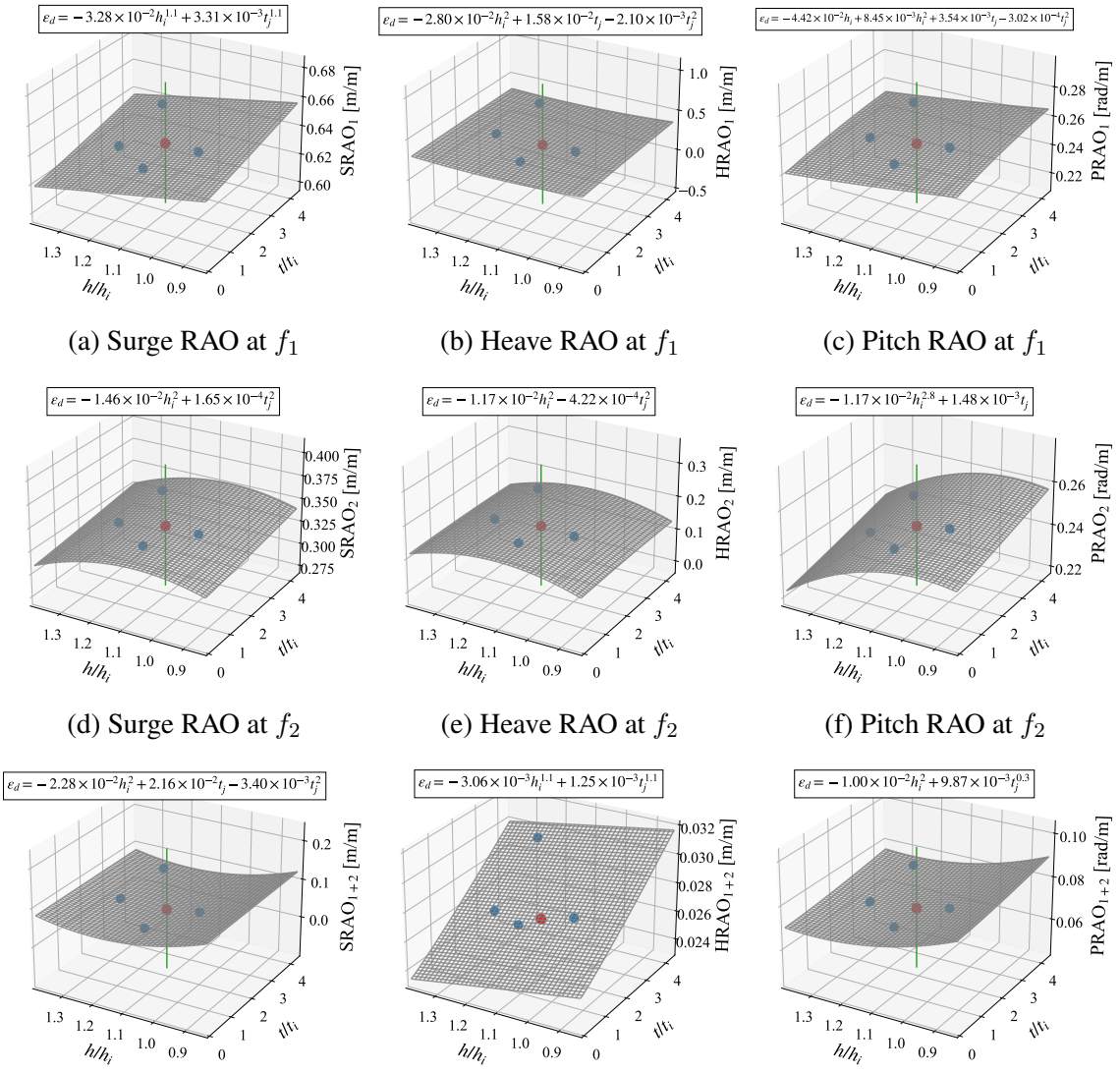

(a) Surge RAO at f_1 (b) Heave RAO at f_1 (c) Pitch RAO at f_1

(d) Surge RAO at f_2 (e) Heave RAO at f_2 (f) Pitch RAO at f_2

(g) Surge RAO at $f_1 + f_2$ (h) Heave RAO at $f_1 + f_2$ (i) Pitch RAO at $f_1 + f_2$

Figure 7.12: 3D fit of all metrics in bichromatic wave case with green bar representing discretization uncertainty bounds for simulation G2T2 (denoted as red dot).

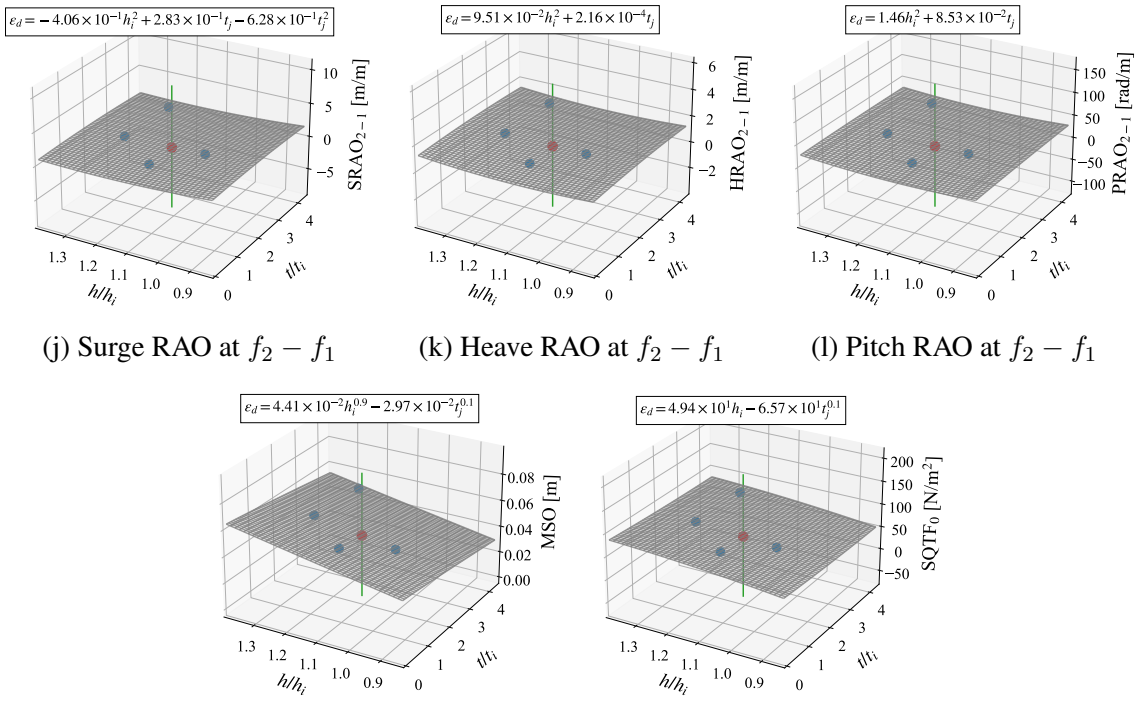

(j) Surge RAO at $f_2 - f_1$ (k) Heave RAO at $f_2 - f_1$ (l) Pitch RAO at $f_2 - f_1$

(m) Mean surge offset (n) Zero frequency surge QTF

Figure 7.12: (Continued) 3D fit of all metrics in bichromatic wave case with green bar representing discretization uncertainty bounds for simulation G2T2 (denoted as red dot).

Table 7.7: Discretization uncertainties of all metrics in bichromatic wave case. The error constants and order of convergence in space and time as described in Equation 2.51 are attached.

	Ext. value ϕ_0	**G2T2** ϕ_1	**Dis. unc.** U_ϕ	α_x	p_x	α_t	p_t
SRAO_1	6.6626×10^{-1}	6.4064×10^{-1}	6.40%	-3.28×10^{-2}	1.1	3.31×10^{-3}	1.1
HRAO_1	3.1472×10^{-1}	2.9896×10^{-1}	15.81%	-2.80×10^{-2}	2	$^{*}1.58 \times 10^{-2}$, -2.10×10^{-3}	$^{*}1$, 2
PRAO_1	2.8657×10^{-1}	2.5391×10^{-1}	16.08%	$^{*} - 4.42 \times 10^{-2}, 8.45 \times 10^{-3}$	$^{*}1$, 2	$^{*}3.54 \times 10^{-3}$, -3.02×10^{-4}	$^{*}1$, 2
SRAO_2	3.5445×10^{-1}	3.4072×10^{-1}	12.09%	-1.46×10^{-2}	2	1.65×10^{-4}	2
HRAO_2	1.7811×10^{-1}	1.6707×10^{-1}	19.82%	-1.17×10^{-2}	2	-4.22×10^{-4}	2
PRAO_2	2.5931×10^{-1}	2.4816×10^{-1}	13.48%	-1.17×10^{-2}	2.8	1.48×10^{-3}	1
SRAO_+	7.3290×10^{-2}	6.9998×10^{-2}	14.11%	-2.28×10^{-2}	2	$^{*}2.16 \times 10^{-2}$, -3.40×10^{-3}	$^{*}1$, 2
HRAO_+	2.7807×10^{-2}	2.6797×10^{-2}	4.71%	-3.06×10^{-3}	1.1	1.25×10^{-3}	1.1
PRAO_+	7.5422×10^{-2}	7.4146×10^{-2}	2.15%	-1.00×10^{-2}	2	9.87×10^{-3}	0.3
SRAO_-	1.4640×10^{0}	1.2245×10^{0}	58.68%	-4.06×10^{-1}	2	$^{*}2.83 \times 10^{-1}$, -6.28×10^{-2}	$^{*}1$, 2
HRAO_-	1.0474×10^{0}	1.1534×10^{0}	27.57%	9.51×10^{-2}	2	2.16×10^{-4}	1
PRAO_-	2.2029×10^{1}	2.3370×10^{1}	17.21%	1.46×10^{0}	2	8.53×10^{-2}	1
MSO	3.1747×10^{-2}	4.7887×10^{-2}	42.13%	4.41×10^{-2}	0.9	-2.97×10^{-2}	0.1
SQTF_0	8.4218×10^{1}	7.0392×10^{1}	58.92%	4.94×10^{1}	1.1	-6.57×10^{1}	0.1

* Fit is made using first and second order exponents as $\alpha_{x1} h_i + \alpha_{x2} h_i^2$.

7.3 JONSWAPS spectrum random waves

7.3.1 Numerical settings

The computational domain used in the random wave case has the same dimensions as the domain for regular wave case, with length $L = 26$ m, width $W = 5$ m, height $h = 5.6$ m and a water depth of $d = 4$ m. The semi-submersible platform is placed with its center of gravity coincides with the origin of the coordinate and surge, sway, heave directions align with x, y and z axes. Unstructured hexahedral mesh is generated in the computational domain. Grid refinement around the platform is the same as the refinement settings described in regular wave case. The refinement strategy as shown in Table 6.1 is adopted near and underneath the free surface. The reference grid size in random wave case is taken as $h_{ref} = 0.008$ m which is 1/16 of significant wave height $H_S = 0.142$ m. The reference wave amplitude is $a = 0.16$ m which is the maximum wave amplitude measured in the experiment. The reference wavelength is $\lambda = 4.57$ m which is computed from the peak period $T_p = 1.711$ s. The total cell count of the mesh is 6.15 millions.

The boundary condition at each boundary is set the same as the computational domain in regular wave case. The length of preset wave absorption zone is adequate to absorb such random waves. All numerical solver settings are as listed in Table 6.3 except that a $k - \omega$ SST-IDDES turbulence model is applied in this simulation. The time step size is $\Delta t = 0.005$ s where a theoretical Courant number of 0.167 is maintained.

7.3.2 Wave-only simulation

A comparative study between numerically reconstructed wave time series and experimental wave time series is performed. In the wave only simulation, all numerical settings are the same as described in previous subsection except that the semi-submersible platform is removed. A wave probe is placed at the centerline of the platform to monitor the wave elevation of incident waves. To investigate the effect brought by the grid resolution, a grid with $h_{ref} = 0.004$ m is generated and the simulation results of this grid are added for comparison.

Figure 7.13 presents the comparison of the numerical and experimental results of the wave el-

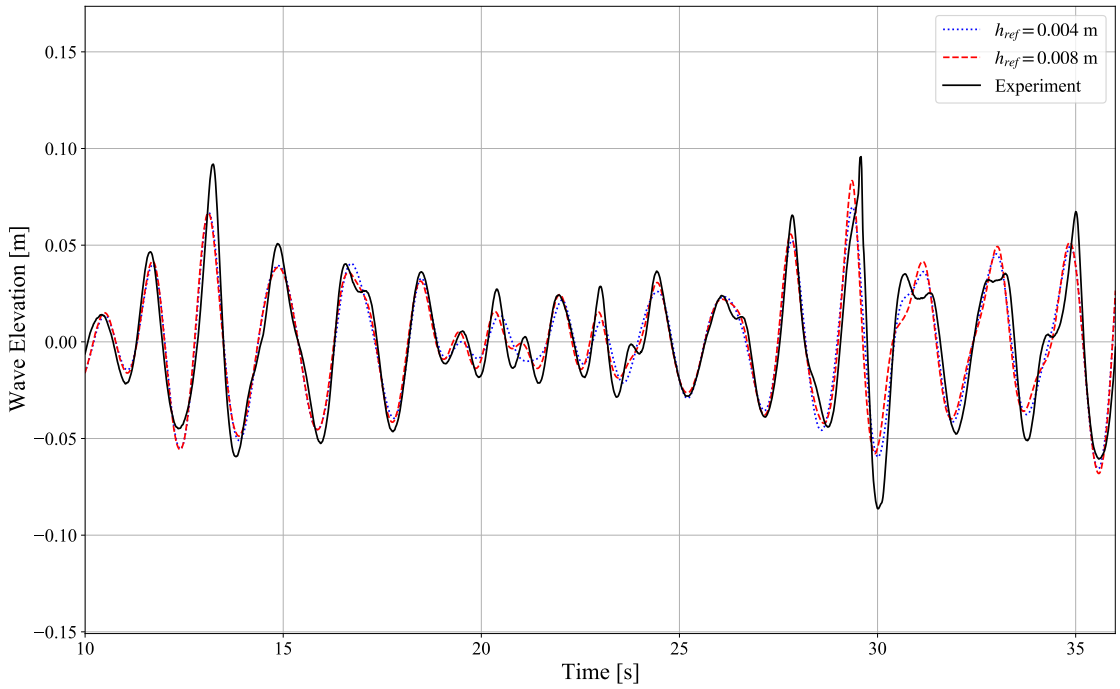

Figure 7.13: Comparison of JONSWAP spectrum random wave elevation histories from numerical simulations and experiment.

evation histories. The numerical wave elevations are in fair agreement with the experimental wave elevations. Whereas the loss of agreement in small amplitude fluctuations and under-prediction in large amplitudes are still presented as like in the benchmark focused wave case. The finer grid does not resolve this issue, while it is getting close to the experimental results in the small fluctuations at some places, the under-prediction in larger amplitudes is even worse. Again, the small amplitude fluctuations are possibly due to the noise in the experimental measurements. The grid with reference grid size $h_{ref} = 0.008$ m is capable for the simulation of JONSWAP spectrum random waves in the following validation study.

7.3.3 Validation study with the semi-submersible platform

A simulation with a total time of 300 s is performed for the random wave condition. The simulation is conducted on clusters provided by Texas A&M University HPRC using 720 Intel Xeon 6248R 3.0 GHz cores. The total wall time for the simulation is about 12.5 days. Based on a TST analysis, the initial 50 s is dropped as the transient phase.

The power spectral density of the 3 DOFs response in surge, heave and pitch are depicted in Figure 7.14 - 7.16. The heave response possesses a lower magnitude in PSD than other two responses. Hence, more focus is put on the surge and pitch responses. The simulation results are in good agreement with experimental results in the wave frequency range in surge and pitch PSD. Resonance responses can be observed in PSD of all 3 DOFs at the natural frequencies. The simulation is able to capture the resonance but under-predicts in magnitudes for surge and pitch and over-predicts for heave response.

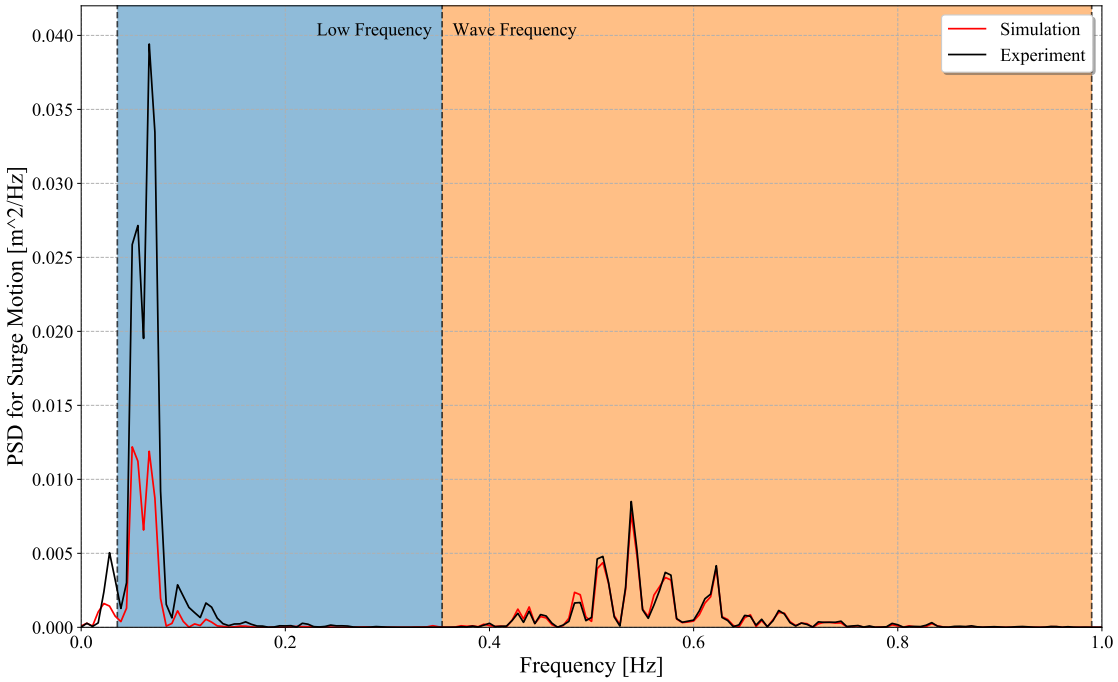

Figure 7.14: Power spectral density of surge responses of the semi-submersible platform under random waves. The blue shade denotes low frequency range (0.0354, 0.3536) Hz and orange shade denotes wave frequency range (0.3536, 0.9900) Hz.

The PSD sums of low frequency range and wave frequency range for both numerical and experimental results are shown in Figure 7.17. The uncertainty levels for all metrics and validation with experimental data are listed in Table 7.8. A conservative numerical uncertainty level of 20 % for all metrics are estimated based on the verification study of semi-submersible platform under

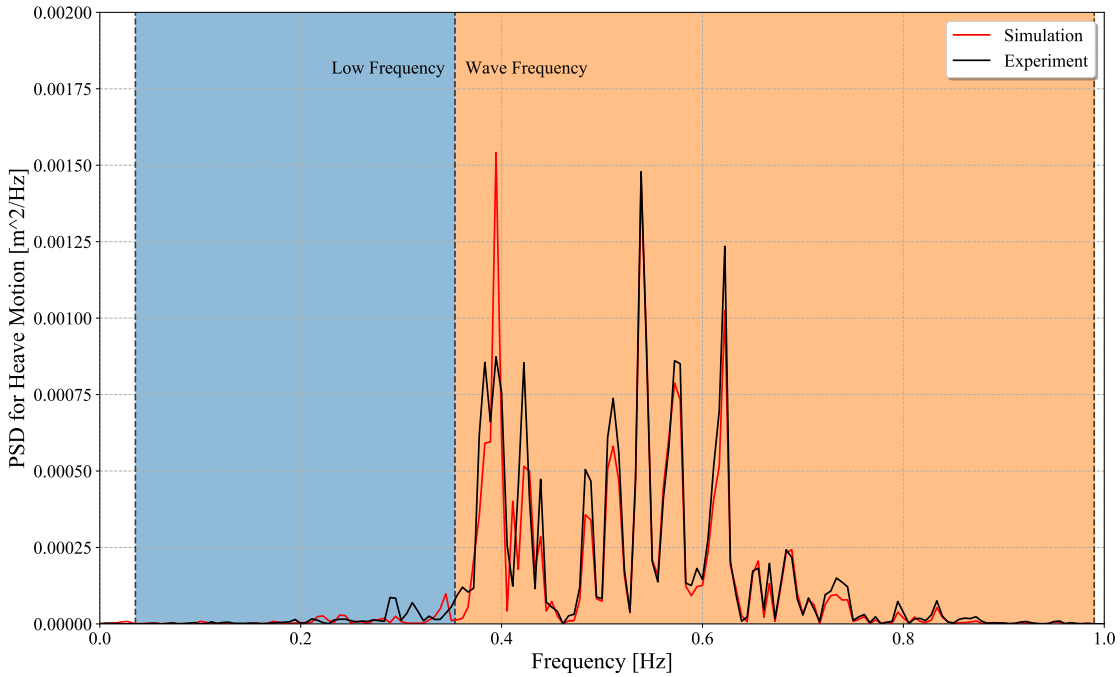

Figure 7.15: Power spectral density of heave responses of the semi-submersible platform under random waves. The blue shade denotes low frequency range (0.0354, 0.3536) Hz and orange shade denotes wave frequency range (0.3536, 0.9900) Hz.

bichromatic waves. The total experimental uncertainty is provided in Robertson et al. [46] for the PSD sums of surge and pitch responses.

The validation is achieved in PSD sums of all 3 DOFs responses of wave frequency range but failed in all PSD sums of low frequency range. The numerical results show smaller PSD sums of low frequency range in 3 DOFs where low frequency surge PSD sum is largely under-predicted. This is consistent with numerical results presented in OC5 project where most of the modelling tools under-predicted the low frequency surge and pitch PSD sums [2].

The natural frequencies of surge and pitch motion of the semi-submersible platform fall in the low frequency range where resonance is observed as much higher magnitudes in the PSD diagrams. While the responses to wave frequency components are well simulated, the resonant responses are highly sensitive to the input parameters in simulation configurations. As mentioned in the previous study, the detail property of the test model is not fully provided. Hence, the simulation

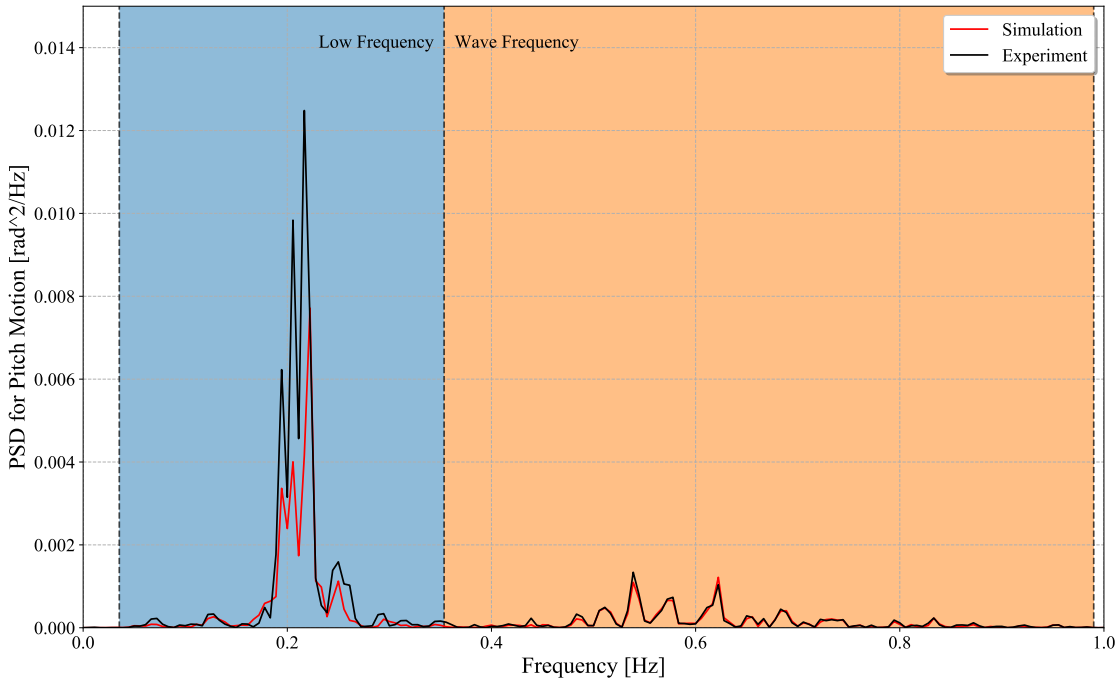

Figure 7.16: Power spectral density of pitch responses of the semi-submersible platform under random waves. The blue shade denotes low frequency range (0.0354, 0.3536) Hz and orange shade denotes wave frequency range (0.3536, 0.9900) Hz.

configuration cannot reproduce the same property of the platform in the experiment, resulting that discrepancies are presented out of the uncertainty bounds.

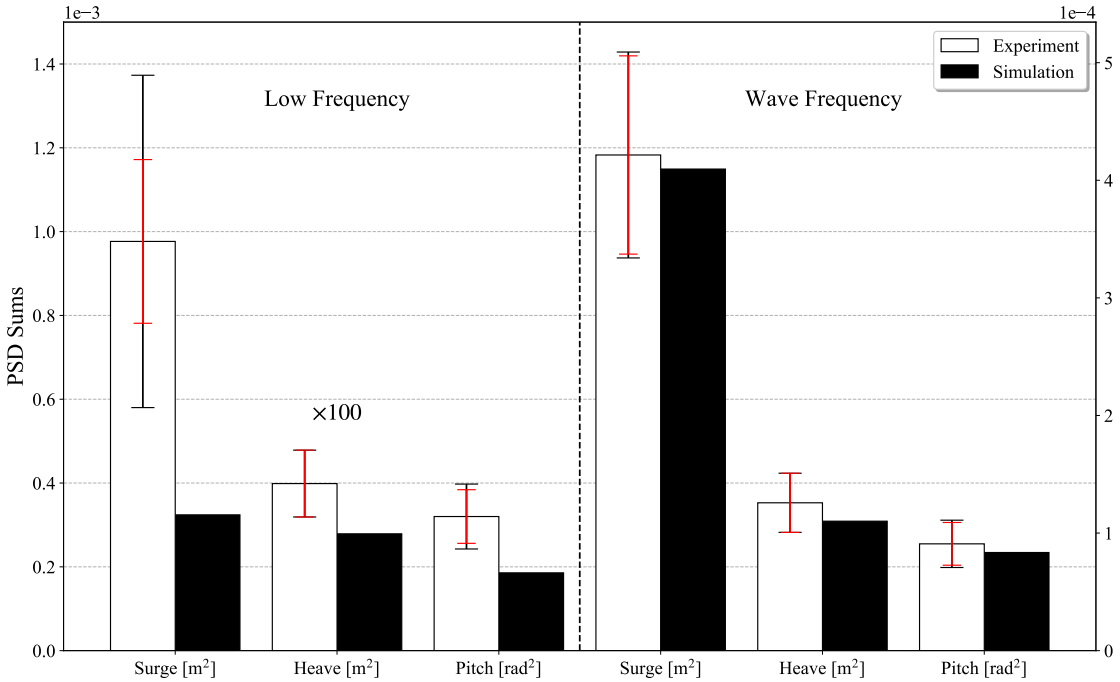

Figure 7.17: Validation of the PSD sums in low frequency range and wave frequency range of the semi-submersible platform under random waves. The red uncertainty bands represent the numerical uncertainty and the black ones represent the validation uncertainty. The heave PSD sum of low frequency is scaled up by a factor of 100.

Table 7.8: The numerical uncertainties, total experiment uncertainty, and validation uncertainty of PDS sums in 3 DOFs for the semi-submersible platform under random wave condition. Judgement of validation is determined by direct comparion of E and U_V.

	Total exp. unc. $\sqrt{U_{exp}^2 + U_I^2}$	**Num. unc.** U_N	**Validation unc.** U_V	**Numerical value** ϕ_N	**Exp. value** ϕ_{exp}	**Comp. error** E	**Validated?**
Low surge PSD sum	35.339%	20%	40.606%	3.2405×10^{-4}	9.7657×10^{-4}	66.818%	No
Low heave PSD sum	N/A	20%	20.000%	2.7879×10^{-6}	3.9873×10^{-6}	30.080%	No
Low pitch PSD sum	13.613%	20%	24.193%	1.8567×10^{-4}	3.2008×10^{-4}	41.992%	No
Wave surge PSD sum	5.607%	20%	20.771%	4.0954×10^{-4}	4.2152×10^{-4}	2.840%	Yes
Wave heave PSD sum	N/A	20%	20.000%	1.1010×10^{-4}	1.2573×10^{-4}	12.432%	Yes
Wave pitch PSD sum	9.509%	20%	22.145%	8.3461×10^{-5}	9.0829×10^{-5}	8.112%	Yes

8. CONCLUSIONS

8.1 Generalized procedure of V&V study

For the widespread of CFD for renewable energy applications one needs to quantify all possible errors in order to increase their credibility. The following procedures are generalized to conduct a verification and validation study:

- Select several metrics that is of interest. For decay test, natural periods, linear and quadratic damping coefficients are often investigated. For regular wave cases, mean offset in wave direction and RAOs in wave direction, transverse wave direction and rotation whose axis lies in transverse wave direction are often used;
- Generate the computational domain for the specific model with adequate resolution at free surface to resolve the waves. Refine the entire computational domain in several steps to generate grids with different spatial sizes;
- Design a simulation matrix which consists of at least 5 different combinations of spatial and temporal sizes. Select a intermediate setup as baseline setup;
- For periodic load conditions, conduct one simulation with baseline setup for the quantification of statistical uncertainty. Based on the statistical uncertainty analysis, select a time window with stationary signal for the computation of investigated metrics;
- Conduct at least 3 simulations with the baseline setup but with different convergence tolerances. Select a baseline convergence tolerance for the remaining analysis and quantify the iterative uncertainty;
- Conduct the simulations with grid and time step setups according to the simulation matrix. Quantify the discretization uncertainty for the baseline simulation;

- Derive the total numerical uncertainty as the combination of the statistical, iterative and discretization uncertainties;

- For each input parameter that required input uncertainty analysis, conduct at least 3 simulations with the input parameter changing individually. Quantify the input uncertainty of each parameter using local sensitivity method;

- Combine the numerical uncertainty with the input uncertainty and the experimental uncertainty provided in experiment report to obtain the validation uncertainty. Compare the validation uncertainty with the comparison error between numerical and experimental results to determine validation

8.2 Conclusions

In this work, a mooring module MOORING3D is coupled with an in-house CFD code ReFRESCO to simulate the DeepCwind semi-submersible platform of FOWT with mooring system in several load conditions. Coefficients of the mooring lines are investigated and calibrated for accurate presentation of the mooring system. A systematic verification and validation study is then performed to quantify a series of uncertainties in several metrics that present important physics and validate against experiments.

For pitch free decay load condition, 20 simulations with different spatial and temporal sizes are designed for the study of discretization uncertainty where simulation G3T4 in balance of accuracy and computing costs is selected as the baseline simulation. Iterative uncertainty is found to have little contribution to the total numerical uncertainty and is neglected. The numerical uncertainty for the pitch natural period is quantified based on solutions from all simulations and 1.1% uncertainty is obtained for baseline simulation G3T4. The numerical uncertainty for the pitch motion is quantified based on pitch motions at time instances distributed along first 4 oscillation cycles from all or some of the simulations depending on the length of simulation time. From the observation of a smooth pattern of numerical uncertainty over time, an average or maximum of numerical uncertainty is selected for uncertainty quantification in the validation study. The values of mean and

maximum numerical uncertainty are respectively 5.9 % and 13.28 % of initial pitch angle.

A validation study is performed using simulation setup same as G3T4 with linear and dynamic mooring model applied. Significant improvements are found using a dynamic mooring model. Validation is achieved for the pitch natural period predicted by simulation within uncertainty level. Validation is also achieved for the linear damping coefficient p derived from numerical solution within mean uncertainty level. However, the simulation under-predicts the quadratic damping coefficient which is out of the maximum uncertainty level.

For the regular wave conditions, the statistical, iterative and discretization uncertainties are carefully identified and quantified from numerical results towards 8 selected metrics - surge, heave and pitch RAOs at wave frequency and double wave frequency, mean surge offset and zero frequency surge QTF. The statistical uncertainty is analyzed in the first place where a time window of [20, 100] s is selected to avoid the initial transient phase of the motion histories. The simulation with 60 outer iterations per time step is selected as the baseline setup based on the following iterative uncertainty analysis. The discretization uncertainty forms the last piece of the numerical uncertainty. The G2T2 simulation in balance of accuracy and computing cost is selected as the baseline setup. The total numerical uncertainty is obtained for the metrics combining the above uncertainties. The numerical uncertainties are generally higher for metrics associated with second order responses. The spatial discretization uncertainty due to mesh resolution is identified as the dominant source of numerical uncertainty.

The total numerical uncertainty is combined with the total experimental uncertainty to form the validation uncertainty. Validation is achieved for SRAO, HRAO and PRAO. Validation is also achieved for $SRAO_2$, $HRAO_2$ and $PRAO_2$ but with a larger validation uncertainty. Validation is failed for MSO and $SQTF_0$. A comparison between linear and dynamic mooring model again indicates that utilization of dynamic mooring model significantly improves the numerical results in validation with the experiments.

A focused wave generation case is performed to investigate the performance of irregular wave generation of the CFD code ReFRESCO. Satisfactory agreement is found between numerical re-

sults and the experimental results.

For the bichromatic wave conditions, the statistical and iterative uncertainties are neglected and primarily the discretization uncertainty is investigated. With the G2T2 simulation selected as the baseline setup, 5 simulations with combinations of different grids and time step sizes are performed. A transient phase of 40 s is dropped in the data processing. The discretization uncertainties for surge, heave and pitch RAO at both wave frequencies, wave sum-frequency and diff-frequency, the mean surge offset and the zero frequency surge QTF are quantified. Most of the uncertainty are within a level of 20 % while metrics related with second order surge response obtain a higher uncertainty at 40-60 %.

The numerical uncertainty obtained from bichromatic wave is applied to the numerical results of simulations of semi-submersible platform under random waves for validation study. Validation is achieved for the PSD sums of surge, heave and pitch responses in the wave frequency range but is failed for PSD sums in the low frequency range.

A verification and validation procedure is generalized from this work and is applicable to CFD simulations of hydrodynamics of FOWT. The procedure provides a general guideline to CFD simulations of FOWT by giving the uncertainty level of a specific grid and time step setup. To obtain confidence in the CFD results for FOWT simulations, it is recommended to carry out the generalized V&V procedure.

REFERENCES

[1] A. Robertson, J. Jonkman, F. Wendt, A. Goupee, and H. Dagher, "Definition of the OC5 DeepCwind semisubmersible floating system," tech. rep., NREL, 2016.

[2] A. N. Robertson, F. Wendt, J. M. Jonkman, W. Popko, H. Dagher, S. Gueydon, J. Qvist, F. Vittori, J. Azcona, E. Uzunoglu, C. G. Soares, R. Harries, A. Yde, C. Galinos, K. Hermans, J. B. de Vaal, P. Bozonnet, L. Bouy, I. Bayati, R. Bergua, J. Galvan, I. Mendikoa, C. B. Sanchez, H. Shin, S. Oh, C. Molins, and Y. Debruyne, "OC5 project phase II: Validation of global loads of the DeepCwind floating semisubmersible wind turbine," *Energy Procedia*, vol. 137, pp. 38–57, oct 2017.

[3] L. Wang, A. Robertson, J. Jonkman, Y.-H. Yu, A. Koop, A. B. Nadal, H. Li, E. Bachynski-Polić, R. Pinguet, W. Shi, *et al.*, "OC6 phase Ib: Validation of the CFD predictions of difference-frequency wave excitation on a FOWT semisubmersible," *Ocean Engineering*, vol. 241, p. 110026, 2021.

[4] A. N. Robertson, S. Gueydon, E. Bachynski, L. Wang, J. Jonkman, D. Alarcón, E. Amet, A. Beardsell, P. Bonnet, B. Boudet, *et al.*, "OC6 Phase I: Investigating the underprediction of low-frequency hydrodynamic loads and responses of a floating wind turbine," in *Journal of Physics: Conference Series*, vol. 1618, p. 032033, IOP Publishing, 2020.

[5] F. Beyer, M. Arnold, and P. W. Cheng, "Analysis of floating offshore wind turbine hydrodynamics using coupled CFD and multibody methods," in *The twenty-third international offshore and polar engineering conference*, 06 2013. ISOPE-I-13-071.

[6] S. Quallen and T. Xing, "CFD simulation of a floating offshore wind turbine system using a variable-speed generator-torque controller," *Renewable Energy*, vol. 97, pp. 230–242, nov 2016.

[7] T. T. Tran and D.-H. Kim, "Fully coupled aero-hydrodynamic analysis of a semi-submersible FOWT using a dynamic fluid body interaction approach," *Renewable Energy*, vol. 92,

pp. 244–261, jul 2016.

[8] C. Liu and C. Hu, "CFD simulation of a floating wind turbine platform in rough sea conditions," in *The Twenty-fourth International Ocean and Polar Engineering Conference*, 2014. ISOPE-I-14-006.

[9] Y. Liu, Q. Xiao, A. Incecik, C. Peyrard, and D. Wan, "Establishing a fully coupled CFD analysis tool for floating offshore wind turbines," *Renewable Energy*, vol. 112, pp. 280–301, nov 2017.

[10] S. Burmester, G. Vaz, S. Gueydon, and O. el Moctar, "Investigation of a semi-submersible floating wind turbine in surge decay using CFD," *Ship Technology Research*, vol. 67, no. 1, pp. 2–14, 2020.

[11] Y. Wang, H.-C. Chen, G. Vaz, and S. Burmester, "CFD simulation of semi-submersible floating offshore wind turbine under pitch decay motion," in *ASME 2019 2nd International Offshore Wind Technical Conference*, American Society of Mechanical Engineers, nov 2019.

[12] Y. Wang, H.-C. Chen, G. Vaz, S. Burmester, *et al.*, "CFD simulation of semi-submersible floating offshore wind turbine under regular waves," in *The 30th International Ocean and Polar Engineering Conference*, 2020. ISOPE-I-20-1166.

[13] Y. Wang, H.-C. Chen, A. Koop, and G. Vaz, "Verification and validation of CFD simulations for semi-submersible floating offshore wind turbine under pitch free-decay motion," *Ocean Engineering*, vol. 242, p. 109993, 2021.

[14] P. J. Roache, *Fundamentals of verification and validation*. Hermosa Publishers, 2009.

[15] L. Eça and M. Hoekstra, "A procedure for the estimation of the numerical uncertainty of CFD calculations based on grid refinement studies," *Journal of Computational Physics*, vol. 262, pp. 104–130, apr 2014.

[16] S. Burmester, G. Vaz, and O. el Moctar, "Towards credible CFD simulations for floating offshore wind turbines," *Ocean Engineering*, vol. 209, p. 107237, 2020.

[17] J. Oberhagemann, *On prediction of wave-induced loads and vibration of ship structures with finite volume fluid dynamic methods*. PhD thesis, Universität Duisburg-Essen, 2016.

[18] T. Xing and F. Stern, "Factors of safety for Richardson extrapolation," *Journal of Fluids Engineering*, vol. 132, jun 2010.

[19] L. Wang, A. Robertson, J. Jonkman, and Y.-H. Yu, "Uncertainty assessment of CFD investigation of the nonlinear difference-frequency wave loads on a semisubmersible FOWT platform," *Sustainability*, vol. 13, p. 64, dec 2020.

[20] G. Vaz, F. Jaouen, and M. Hoekstra, "Free-Surface Viscous Flow Computations: Validation of URANS Code FreSCo," in *Volume 5: Polar and Arctic Sciences and Technology; CFD and VIV*, vol. 5, pp. 425–437, ASMEDC, jan 2009.

[21] S. V. Patankar, *Numerical heat transfer and fluid flow*. CRC press, 2018.

[22] C. Klaij, M. Hoekstra, and G. Vaz, "Design, analysis and verification of a volume-of-fluid model with interface-capturing scheme," *Computers & Fluids*, vol. 170, pp. 324–340, jul 2018.

[23] F. R. Menter and Y. Egorov, "The scale-adaptive simulation method for unsteady turbulent flow predictions. part 1: Theory and model description," *Flow, Turbulence and Combustion*, vol. 85, pp. 113–138, jun 2010.

[24] F. R. Menter, M. Kuntz, and R. Langtry, "Ten years of industrial experience with the SST turbulence model," *Turbulence, heat and mass transfer*, vol. 4, no. 1, pp. 625–632, 2003.

[25] B. E. Larsen and D. R. Fuhrman, "On the over-production of turbulence beneath surface waves in Reynolds-averaged Navier–Stokes models," *Journal of Fluid Mechanics*, vol. 853, pp. 419–460, 2018.

[26] M. S. Gritskevich, A. V. Garbaruk, J. Schütze, and F. R. Menter, "Development of DDES and IDDES formulations for the k-ω shear stress transport model," *Flow, turbulence and combustion*, vol. 88, no. 3, pp. 431–449, 2012.

[27] F. R. Menter, Y. Egorov, and D. Rusch, "Steady and unsteady flow modelling using the $k - \sqrt{kL}$ model," in *Proceedings of the International Symposium on Turbulence, Heat and Mass Transfer*, Begellhouse, 2006.

[28] S. Burmester and M. Guérinel, "Calculations of wave loads on a vertical cylinder using potential-flow and viscous-flow solvers," in *International Conference on Offshore Mechanics and Arctic Engineering*, vol. 49989, p. V007T06A054, American Society of Mechanical Engineers, 2016.

[29] L. Skjelbreia and J. Hendrickson, "Fifth order gravity wave theory," *Coastal Engineering Proceedings*, no. 7, pp. 10–10, 1960.

[30] K. F. Hasselmann, T. P. Barnett, E. Bouws, H. Carlson, D. E. Cartwright, K. Eake, J. Euring, A. Gicnapp, D. Hasselmann, P. Kruseman, *et al.*, "Measurements of wind-wave growth and swell decay during the joint north sea wave project (JONSWAP).," *Ergaenzungsheft zur Deutschen Hydrographischen Zeitschrift, Reihe A*, 1973.

[31] S. Rapuc, P. Crepier, F. Jaouen, T. Bunnik, and P. Regnier, "Towards guidelines for consistent wave propagation in CFD simulations," in *19th International Conference on Ship and Maritime Research, Trieste*, 2018.

[32] Y. Saad and M. H. Schultz, "GMRES: A generalized minimal residual algorithm for solving nonsymmetric linear systems," *SIAM Journal on scientific and statistical computing*, vol. 7, no. 3, pp. 856–869, 1986.

[33] W. E. Arnoldi, "The principle of minimized iterations in the solution of the matrix eigenvalue problem," *Quarterly of applied mathematics*, vol. 9, no. 1, pp. 17–29, 1951.

[34] M. R. Hestenes, E. Stiefel, *et al.*, *Methods of conjugate gradients for solving linear systems*, vol. 49. NBS Washington, DC, 1952.

[35] H. A. Van der Vorst, "Bi-CGSTAB: A fast and smoothly converging variant of Bi-CG for the solution of nonsymmetric linear systems," *SIAM Journal on scientific and Statistical Computing*, vol. 13, no. 2, pp. 631–644, 1992.

[36] B. P. Leonard, "A stable and accurate convective modelling procedure based on quadratic upstream interpolation," *Computer methods in applied mechanics and engineering*, vol. 19, no. 1, pp. 59–98, 1979.

[37] B. Van Leer, "Towards the ultimate conservative difference scheme. IV. A new approach to numerical convection," *Journal of computational physics*, vol. 23, no. 3, pp. 276–299, 1977.

[38] F. Jaouën, A. Koop, and L. Vatinel, "URANS predictions of low-frequency damping of a LNGC," in *Volume 2: CFD and FSI*, American Society of Mechanical Engineers, jun 2019.

[39] O. Faltinsen, *Sea loads on ships and offshore structures*, vol. 1. Cambridge university press, 1993.

[40] L. Eça and M. Hoekstra, "Evaluation of numerical error estimation based on grid refinement studies with the method of the manufactured solutions," *Computers & Fluids*, vol. 38, pp. 1580–1591, sep 2009.

[41] L. Eça, G. Vaz, S. L. Toxopeus, and M. Hoekstra, "Numerical errors in unsteady flow simulations," *Journal of Verification, Validation and Uncertainty Quantification*, vol. 4, jun 2019.

[42] J. Brouwer, J. Tukker, Y. Klinkenberg, and M. van Rijsbergen, "Random uncertainty of statistical moments in testing: Mean," *Ocean Engineering*, vol. 182, pp. 563–576, 2019.

[43] H. W. Coleman and F. Stern, "Uncertainties and CFD code validation," *Journal of Fluids Engineering*, vol. 119, pp. 795–803, dec 1997.

[44] E. T. Katsuno, A. K. Lidtke, B. Düz, D. Rijpkema, J. L. Dantas, and G. Vaz, "Estimating parameter and discretization uncertainties using a laminar–turbulent transition model," *Computers & Fluids*, vol. 230, p. 105129, 2021.

[45] E.-J. de Ridder, W. Otto, G.-J. Zondervan, F. Huijs, and G. Vaz, "Development of a scaled-down floating wind turbine for offshore basin testing," in *Volume 9A: Ocean Renewable Energy*, American Society of Mechanical Engineers, jun 2014.

[46] A. Robertson, E. E. Bachynski, S. Gueydon, F. Wendt, and P. Schünemann, "Total experimental uncertainty in hydrodynamic testing of a semisubmersible wind turbine, considering numerical propagation of systematic uncertainty," *Ocean Engineering*, vol. 195, p. 106605, jan 2020.

[47] A. Ern and J.-L. Guermond, *Theory and practice of finite elements*, vol. 159. Springer Science & Business Media, 2013.

[48] N. M. Newmark, "A method of computation for structural dynamics," *Journal of the engineering mechanics division*, vol. 85, no. 3, pp. 67–94, 1959.

[49] S. Gueydon, "Aerodynamic damping on a semisubmersible floating foundation for wind turbines," *Energy Procedia*, vol. 94, pp. 367–378, sep 2016.

[50] S. Burmester, G. Vaz, O. el Moctar, S. Gueydon, A. Koop, Y. Wang, and H. C. Chen, "High-fidelity modelling of floating offshore wind turbine platforms," in *Volume 9: Ocean Renewable Energy*, American Society of Mechanical Engineers, aug 2020.

[51] J. Palm, C. Eskilsson, G. M. Paredes, and L. Bergdahl, "Coupled mooring analysis for floating wave energy converters using CFD: Formulation and validation," *International Journal of Marine Energy*, vol. 16, pp. 83–99, dec 2016.

[52] A. Sommerfeld, *Partial differential equations in physics*. Academic Press, 1949.

[53] A. de Boer, M. van der Schoot, and H. Bijl, "Mesh deformation based on radial basis function interpolation," *Computers & Structures*, vol. 85, pp. 784–795, jun 2007.

[54] S. Balay, S. Abhyankar, M. F. Adams, J. Brown, P. Brune, K. Buschelman, L. Dalcin, A. Dener, V. Eijkhout, W. D. Gropp, D. Karpeyev, D. Kaushik, M. G. Knepley, D. A. May, L. C. McInnes, R. T. Mills, T. Munson, K. Rupp, P. Sanan, B. F. Smith, S. Zampini, H. Zhang, and H. Zhang, "PETSc users manual," Tech. Rep. ANL-95/11 - Revision 3.15, Argonne National Laboratory, 2021.

[55] V. Sriram, S. Agarwal, and T. Schlurmann, "Laboratory study on steep wave interactions with fixed and moving cylinder," *International Journal of Offshore and Polar Engineering*, vol. 31, no. 01, pp. 19–26, 2021.

[56] V. Sriram, T. Schlurmann, and S. Schimmels, "Focused wave evolution using linear and second order wavemaker theory," *Applied Ocean Research*, vol. 53, pp. 279–296, 2015.

[57] S. Yan, Q. Ma, W. Asnim, Z. Sulaiman, and H. Sun, "Comparative study on focusing wave interaction with cylinder using QALE-FEM and qaleFOAM," in *The 30th International Ocean and Polar Engineering Conference*, OnePetro, 2020.

[58] Y.-J. Ha, S.-K. Cho, and S. Y. Hong, "CFD study for steep focused wave interactions with fixed and moving cylinders," *International Journal of Offshore and Polar Engineering*, vol. 31, no. 01, pp. 53–60, 2021.